UNIVERSITÀ DI PARMA

UNIVERSITÀ DEGLI STUDI DI PARMA

DOTTORATO DI RICERCA IN

"SCIENZE DEL FARMACO"

CICLO XXXVI

Respirable nano/micro systems for prevention and treatment of pulmonary infectious diseases

Coordinatore:
Chiar.mo Prof. Marco Mor

Tutore:
Chiar.mo Prof. Ruggero Bettini

Dottoranda: Daisy Sorgi

Anni Accademici 2020/2021 – 2022/2023

Table of Contents

List of Figures

List of Tables

List of Equations

Abbreviations

ACI	Andersen Cascade Impactor
ACN	Acetonitrile
ASL	Airway surface liquid
CV	Coefficient variation
DCR	Derived count rate
DD	Delivered dose
DLS	Dynamic light scattering
DMEM	Dulbecco's Modified Eagle's Medium
DMSO	Dimethyl sulfoxide
DSC	Differential scanning calorimetry
Dv10	Volume diameter of the 10^{th} percentile of the particle population
Dv50	Volume diameter of the 50^{th} percentile of the particle population
Dv90	Volume diameter of the 90^{th} percentile of the particle population
ED	Emitted dose
ELISA	Enzyme-linked immunosorbent assay
EtOH	Ethanol
FBS	Fetal bovine serum
FDA	Food and Drug Administration
FPD	Fine particle dose
FPF	Fine particle fraction
HBSS	Hank's balanced salt solution
HPLC	High-performance liquid chromatography
IL-6	Interleukin 6
IL-8	Interleukin 8
IMQ	Imiquimod
Imq_M	Imiquimod micronized particles
Imq_RM	Imiquimod raw material
Imq_SD	Imiquimod spray-dried particles
IP	Induction port

LAM	Lipoarabinomannan
LOD	Lower limit of detection
LOQ	Lower limit of quantification
LPS	Lipopolysaccharide
MeOH	Methanol
MMAD	Mass median aerodynamic diameter
MPL	30-O-deacylated monophosphoryl lipid A
Mtb	*Mycobacterium tuberculosis*
MTT	3-(4,5-dimethylthiazol-2-yl)-2,5-diphenyl tetrazolium bromide
NCs	Nanoconjugates
nDCR	Normalized derived count rate
NMR	Nuclear magnetic resonance
PBS	Phosphate-buffered saline
PdI	Polydispersity index
PG	Propylene glycol
PMA	Poly (malic acid)
POA	Pyrazinoic acid
POA-NC	Pyrazinoic acid nanoconjugate
PXRD	Powder X-ray diffraction
PZA	Pyrazinamide
RSD	Relative standard deviation
SEM	Scanning electron microscopy
SLF	Simulated lung fluid
TB	Tuberculosis
TEM	Transmission electron microscopy
TGA	Thermogravimetric analysis
THF	Tetrahydrofuran
TLRs	Toll-like receptors

1 General overview

This doctoral thesis focuses on pulmonary drug delivery, which is gaining increasing interest as a potential substitute for traditional drug delivery systems. Orally inhaled therapy has proven efficient in treating local lung diseases like asthma, chronic obstructive pulmonary diseases, and cystic fibrosis, thanks to the precise and quick targeting of drugs to specific areas of the respiratory tract in a non-invasive manner. Additionally, it proved suitable to treat systemic diseases like diabetes mellitus, Parkinson's disease, and schizophrenia, thanks to exploiting the alveoli's high surface area for systemic delivery. Pulmonary delivery proved to be suitable both for small molecules and biologics.

As well as being a potential target in treating local and systemic diseases, the lungs may represent the target site in administering active ingredients intended to prevent or treat infectious diseases that see the airways as the primary site of entry of the pathogen or the site where the most severe symptoms of the disease are most expressed. In this respect, stimulating the immune response could represent an innovative mode for reducing the incidence of infectious diseases.

Among immunostimulants, imiquimod represents a compound of interest because it is already approved for topical administration and is employed extensively in off-label therapeutic trials. However, this molecule has been successfully formulated to date only as semi-solid lipophilic formulations for topical application, has been described as poorly soluble in most solvents, including water, and solubility data available in the literature are discordant. This thesis is structured into three consecutive chapters. The first one aims to investigate IMQ solubility in solvents suitable to develop innovative IMQ formulations like inhalation spray-dried powders, which will be the focus of the second chapter, and to clarify literature discrepancies to collect robust and reliable data.

The second chapter aims to design an imiquimod powder suitable for inhalation administration and helpful in preventing infectious diseases due to its ability to stimulate innate immunity in

the lungs, but also potentially valuable for fighting them, as an adjuvant in allergen immunotherapy or intended to be combined with an antigen for the formulation of vaccines for inhalation or nasal administration.

The third chapter aims to exploit the benefits of inhalation administration, extensively discussed in the second chapter, to improve the treatment of tuberculosis, an infectious disease predominantly affecting the lungs, contributing to millions of deaths worldwide. Current tuberculosis treatments are effective but linked to severe adverse effects due to the high daily doses of each anti-tuberculosis drug through oral therapy. In detail, the final part of this thesis aims to overcome this issue by designing a spray-dried powder of microparticles embedding innovative pyrazinoic acid nanoconjugates developed for pulmonary administration, a promising strategy to achieve an efficient lung deposition, and reducing the administered doses, achieving a high drug payload and controlled release at the target site.

2 CHAPTER I: IN-DEPTH ANALYSIS OF IMIQUIMOD SOLUBILITY THROUGH AN INTERPRETATIVE APPROACH

This chapter allowed the writing of the article 'Imiquimod Solubility in Different Solvents: An Interpretative Approach' published in *Pharmaceutics* (Volume 16, Issue 2) on 15 February 2024, to which Daisy Sorgi contributed with conceptualization, methodology, investigation, writing of the original draft.

2.1 Introduction

2.1.1 Imiquimod

Imiquimod (IMQ), whose structure is reported in Figure 1, is a synthetic drug belonging to the class of imidazoquinolones, approved by the Food and Drug Administration (FDA) for treating external anogenital warts, actinic keratoses, and superficial basal cell carcinomas, and employed extensively in off-label therapeutic trials due to its pharmacological properties [1]. IMQ has an immunostimulant activity due to the agonism of toll-like receptors (TLRs) 7 and 8, which modulate the innate immune system, inducing secretion of pro-inflammatory cytokines such as interferon α, interferon γ, tumor necrosis factor α, and interleukin 12 [2]. In addition, topical administration of IMQ induces functional maturation of epidermal Langerhans cells, stimulates migration to regional lymph nodes, and promotes a Th1-biased and antigen-specific $CD8^+$ T cell response [3]. IMQ, which is commercially available as a 5 and 3.75% cream [4], is highly challenging to formulate because of its low solubility in hydrophilic or lipophilic vehicles [5], and has been successfully formulated to date mainly as semi-solid lipophilic formulations for topical application.

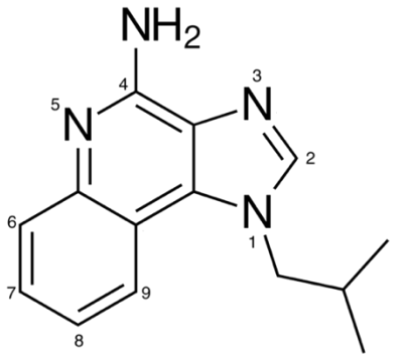

***Figure 1**. IMQ chemical structure.*

2.1.2 Review of IMQ literature solubilities

A review of the available literature regarding IMQ solubility [5–11] in pure solvents, sorted from lowest to highest, is summarized in Table 1.

***Table 1**. Literature IMQ solubilities in pure solvents, both as reported and transformed in µg/mL, considering, when possible, also the conditions under which the measurement was carried out.*

Solvent.	Solubility (as reported)	Solubility (µg/mL)	Temperature (°C)	IMQ/solvent contact time (h)	Shaking	Reference
Water	0.00060 mg/mL	0.6	24 ± 2	90	m.	[6]
	0.002 mg/mL	2	n.r.	n.r.	n.r.	[10]
	18 µg/mL	18	n.r.	n.r.	n.r.	[7]
Phosphate buffer saline	1 µg/mL	1	n.r.	n.r.	n.r.	[10]
Isopropyl palmitate	0.01 mg/mL	10	n.r.	n.r.	n.r.	[6]
Sesame oil	~ 0.02 mg/mL	~ 20	25	48	o.	[11]
Miglyol® 812	~ 0.02 mg/mL	~ 20	25	48	o.	[11]
Almond oil	~ 0.05 mg/mL	~ 50	25	48	o.	[11]
Isopropyl myristate	~ 0.05 mg/mL	~ 50	25	48	o.	[11]
Acetonitrile	0.055 mg/mL	55	n.r.	n.r.	n.r.	[6]
Sorbitan monooleate	0.06 mg/mL	60	n.r.	n.r.	n.r.	[6]
Acetone	0.096 mg/mL	96	n.r.	n.r.	n.r.	[7]
	0.12 mg/mL	120	n.r.	n.r.	n.r.	[6]
Propylene glycol	0.12 mg/mL	120	n.r.	n.r.	n.r.	[6]
	120 µg/mL	120	n.r.	n.r.	n.r.	[7]
	0.60 ± 0.03 mg/mL	600 ± 30	r.t.	~ 24	s.	[5]
	0.73 ± 0.02 mg/g	705 ± 19	25 ± 0.5	48	w.	[8]

Ethanol	0.23 ± 0.0 mg/g	180 ± 0.0	25 ± 0.5	48	w.	[8]
	0.24 mg/mL	240	n.r.	n.r.	n.r.	[6]
	472 µg/mL	472	n.r.	n.r.	n.r.	[7]
Captex® 300	~ 0.3 mg/mL	~ 300	25	48	o.	[11]
Captex® 500	~ 0.3 mg/mL	~ 300	25	48	o.	[11]
PEG 400 monoisostearate	0.33 mg/mL	330	n.r.	n.r.	n.r.	[6]
Methanol	0.46 mg/mL	460	n.r.	n.r.	n.r.	[6]
Chloroform	0.56 mg/mL	560	n.r.	n.r.	n.r.	[6]
Tween 80	0.66 ± 0.02 mg/mL	660 ± 20	r.t.	~ 24	s.	[5]
	0.65 ± 0.025 mg/g	689 ± 27	25 ± 0.5	48	w.	[8]
Dimethylformamide	0.76 mg/mL	760	n.r.	n.r.	n.r.	[6]
Captex® 355	0.8 ± 0.01 mg/g	-	25 ± 0.5	48	w.	[8]
N-methyl-2-pyrrolidone	1.0 mg/mL	1000	n.r.	n.r.	n.r.	[6]
Capmul® MCM	1.02 ± 0.01 mg/g	1015 ± 10	25 ± 0.5	48	w.	[8]
Transcutol	1.11 ± 0.07 mg/mL	1110 ± 70	r.t.	~ 24	s.	[5]
Dimethyl sulfoxide	1.29 ± 0.13 mg/mL	1290 ± 130	r.t.	~ 24	s.	[5]
2-pyrrolidone	1.64 ± 0.12 mg/mL	1640 ± 120	r.t.	~ 24	s.	[5]
PEG 200	1.98 ± 0.38 mg/mL	1980 ± 380	r.t.	~ 24	s.	[5]
Tween 20	1.87 ± 0.01 mg/g	2048 ± 11	25 ± 0.5	48	w.	[8]
Ethyl oleate	2.9 ± 0.2 mg/g	2524 ± 174	25 ± 0.5	48	w.	[8]
Cremophor EL	4.52 ± 0.03 mg/g	4748 ± 32	25 ± 0.5	48	w.	[8]
PEG 400	7.23 ± 0.05 mg/g	8142 ± 56	25 ± 0.5	48	w.	[8]
	7.3 ± 1.84 mg/mL	7300 ± 1840	r.t.	~ 24	s.	[5]
Capmul® PG8	~ 10 mg/mL	~ 10000	25	48	o.	[11]
PEG 600	12.83 ± 1.58 mg/mL	12830 ± 1580	r.t.	~ 24	s.	[5]
Isopropyl alcohol	16.8 ± 0.23 mg/g	13187 ± 181	25 ± 0.5	48	w.	[8]
Isostearic acid	15.73 ± 0.62 mg/mL	15730 ± 620	70	48	w.	[6]
	16.69 ± 0.04 mg/mL	16690 ± 40	60	48	w.	[6]
	17.0 ± 0.08 mg/mL	17000 ± 80	25	48	w.	[6]
	17.21 ± 0.07 mg/mL	17210 ± 70	50	48	w.	[6]
	18.05 ± 0.27 mg/mL	18050 ± 270	30	48	w.	[6]

	18.17 ± 0.07 mg/mL	18170 ± 70	40	48	w.	[6]
	154 ± 0.85 mg/mL	154000 ± 850	n.r.	24	m.	[9]
Linoleic acid	17 mg/mL	17000	r.t.	0.5	m.	[6]
Oleic acid	20 mg/mL	20000	r.t.	0.5	m.	[6]
	73.86 ± 14.2 mg/mL	73860 ± 14200	r.t.	~ 24	s.	[5]
	80 mg/mL	80000	n.r.	n.r.	n.r.	[10]
	111.3 ± 0.60 mg/g	99642 ± 537	25 ± 0.5	48	w.	[8]
	108 ± 0.31 mg/mL	108000 ± 310	25	48	o.	[11]
Capmul® PG12	~ 20 mg/mL	~ 20000	25	48	o.	[11]
Peceol™	~ 20 mg/mL	~ 20000	25	48	o.	[11]
Apifil®	~ 0.8 mg/g	-	80	n.r.	n.r.	[11]
Compritol® 888	~ 1.4 mg/g	-	80	n.r.	n.r.	[11]
Bees wax	~ 1 mg/g	-	80	n.r.	n.r.	[11]
Precirol® ATO 5	~ 1.4 mg/g	-	80	n.r.	n.r.	[11]
Stearyl alcohol	~ 1.4 mg/g	-	80	n.r.	n.r.	[11]

r.t. = room temperature; n.r. = not reported; m. = shaking or mixing; s. = magnetic stirring; w. = shaking water bath, o. = orbital mixer incubator.

Solubilities reported are on the order of µg/mL, except for acids whose solubility reaches the order of mg/mL. The higher solubility values in acids are explained by IMQ being a weak base which, in acidic environments, is converted into the corresponding salt form [6]. This review revealed a wide range of values, highlighting significant discrepancies among literature data. In this regard, there is significant intra-solvent variability regarding solubility values in water (18, 0.6, and 2 µg/mL), propylene glycol (600, 705, and 120 µg/mL), ethanol (180, 240, and 472 µg/mL), isostearic acid (17000, 18050, 18170, 17210, 16690, 15730 and 154000 µg/mL) and oleic acid (73860, 99642, 20000, 80000 and 108000 µg/mL). The intra-solvent variability regarding solubility values, even if less pronounced, is also highlighted in the case of acetone (120 and 96 µg/mL), Tween 80 (689 and 660 µg/mL) and PEG 400 (8142 and 7300 µg/mL). A possible explanation for these significant differences could lie in the fact that the temperature could influence the solubility of IMQ, and that the experimental measurements can be carried out at different temperatures, thus giving rise to discordant results. However, identifying in

which specific cases this explanation is valid is difficult because the temperature was not always reported or was generically reported as “room temperature”, which can be different from laboratory to laboratory and seasonally variable [12]. Moreover, the solubility of IMQ is not necessarily temperature-dependent in all solvents considered. Another possible explanation is the possibility that IMQ takes more than 24-48 h to reach the solid-liquid equilibrium, which could also explain a solubility of 600 µg/mL in propylene glycol after 24 h of mixing and of 705 µg/mL after 48 h, because although 24-48 h stirring time is enough for many compounds, for practically insoluble compounds with very slow dissolution rates as IMQ, an extremely long equilibration time ranging from 10 to 30 days is required, with a series of repeated measurements with increasing agitation time until the solubility is no longer changing [12]. Still, this hypothesis needs to be verified, and, in any case, it is difficult to understand if it is valid because the IMQ/solvent contact time was only sometimes reported. A final hypothesis that can be advanced by observing Table 1 is that IMQ could need proper stirring and kinetic energy to dissolve more rapidly and efficiently. Therefore, the presence or absence of shaking, the shaking force, and the type of shaking could influence the experimental result. In this regard, it should be underlined that each paper used very different conditions to measure the experimental solubility of IMQ, including magnetic stirring, shaking water bath, orbital mixer incubator, generic “shaking” or “mixing”. Often, it is not even specified whether the system was maintained under any stirring. Such a generic description of the operating conditions could imply different kinetic energy from using a magnetic stirrer instead of a shaking water bath, the total absence of stirring, different magnetic stirrers, or different shaking water baths.

2.2 Aim

IMQ has been successfully formulated to date mainly as semi-solid lipophilic formulations for topical application, and literature data regarding IMQ solubility are highly discordant. We aimed to investigate the solubility of IMQ in solvents that can be used to develop formulations intended for innovative administration routes, different from the already well-known and

explored topical ones, for example, powders obtained by spray drying, that will be the topic of the next chapter of this thesis. For this reason, the focus was on water (H_2O), ethanol (EtOH), methanol (MeOH), acetone, acetonitrile (ACN), and dimethyl sulfoxide (DMSO). IMQ solubility was studied at different temperatures, namely 30, 25, 20, 16, and 4 °C. Another aim was to provide a possible explanation of the discrepancies reported in the literature to collect robust and reliable data.

2.3 Materials and methods

2.3.1 Materials

- Acetone (C_3H_6O, Acetone ≥99%, TECHNICAL, VWR International, Radnor, United States)
- Acetone-d_6 (99.9 atom % D, Sigma-Aldrich, Saint Louis, United States)
- Acetonitrile-d_3 (≥99.8 atom % D, Sigma-Aldrich, Saint Louis, United States)
- ACN (CH_3CN, Acetonitrile ≥99.9%, HiPerSolv CHROMANORM®, analytical grade for HPLC, VWR International, Radnor, United States)
- Chloroform-d ($CDCl_3$, 99.8 atom % D, Sigma-Aldrich, Saint Louis, United States)
- DMSO (C_2H_6OS, Dimetilsolfossido ≥99.9% USP, Multi-Compendial, J.T.Baker®, Avantor, Radnor, United States)
- DMSO-d_6 (99.9 atom % D, Sigma-Aldrich, Saint Louis, United States)
- EtOH (C_2H_6O, Etanolo ≥96% (v/v) Reag. Ph. Eur., Supelco®, VWR International, Radnor, United States)
- Hydrochloric acid 37% (HCl, Ph. Eur., Lot #18F064006, VWR International, Radnor, United States)
- Hydrogen peroxide 35% 130VOL.STAB. (H_2O_2, Lot #Q0012832, ACEF; Fiorenzuola d'Arda, Italia)
- IMQ ($C_{14}H_{16}N_4$, Lot #210307, Dayang chem Co., Ltd., Hangzhouzhejiang, China)
- MeOH (CH_3OH, Metanolo ≥99.8%, HiPerSolv CHROMANORM® Reag. Ph. Eur., HPLC grade, VWR International, Radnor, United States)

- Methanol-d_4 (CD_3OD, 99 atom % D, Sigma-Aldrich, Saint Louis, United States)
- Milli-Q water was purified (0.055 µS/cm, TOC 1 ppb) with Purelab pulse + Flex ultra-pure water (Elga Veolia, Milan, Italy)
- Triethylamine ($C_6H_{15}N$, Thermo Fisher Scientific, Waltham, United States)

2.3.2 Methods

2.3.2.1 High-performance liquid chromatography

IMQ in solution was quantified by high-performance liquid chromatography (HPLC) with an Agilent 1200 Series (Agilent Technologies, Santa Clara, United States) driven by ChemStation software version B.04.03-SP1 and using a UV detector set at a wavelength of 242 nm. The HPLC method was developed by adapting one previously described by Telò et al. [5] and by Ghezzi et al. [2]. The mobile phase, composed of MeOH:ACN:H_2O:triethylamine (180:270:530:5), was pumped at a flow rate of 0.9 mL/min through a reverse-phase C_{18} column (Kinetex C18 2.6 µm, 100 Å, 100 × 4.6 mm, Phenomenex, Torrance, United States) kept at 29 °C. In these conditions, the retention time of IMQ was about 2 min. The injection volume for each sample was 10 µL. The analytical method was assessed for response linearity (AUC vs. concentration) in the 10–100 µg/mL concentration range. The calibration curve for the analysis of the solubility of IMQ in EtOH was constructed with standards whose solvent was EtOH:HCl 0.1 M (1:9 v/v) to guarantee complete IMQ dissolution and to replicate the exact ratio between solvents that characterize supernatant solutions of unknown concentration. Similarly, the calibration curve for the analysis of the solubility of IMQ in MeOH was constructed with standards whose solvent was MeOH:HCl 0.1 M (1:9 v/v), in ACN was ACN:HCl 0.1 M (1:9 v/v), in H_2O was H_2O:HCl 0.1 M (1:5 v/v), in acetone was acetone:HCl 0.1 M (1:9 v/v), and in DMSO was DMSO:HCl 0.1 M (1:20 v/v). The lower limit of detection (LOD) and quantification (LOQ) in each solvent were calculated as the analyte concentration at 10 and 33% relative standard deviation (RSD) of the RSD *vs* IMQ concentration curve, respectively, and are reported in

Table 2.

***Table 2**. LOD and LOQ for the calibration curve in each solvent.*

Solvent	LOD (µg/mL)	LOQ (µg/mL)
EtOH	0.03	0.09
MeOH	0.27	0.83
ACN	0.09	0.27
H_2O	0.31	0.93
Acetone	0.44	1.34
DMSO	0.01	0.03

2.3.2.2 Forced degradation studies

To assess whether the analytical method was stability indicating, IMQ was exposed to stress degradation under two conditions: acid hydrolysis performed by putting IMQ in HCl 5 N (0.2 mg/mL) for 3 h at 100 °C and oxidative degradation performed by placing IMQ in 30% H_2O_2 (0.2 mg/mL) for 3 h at 100 °C.

2.3.2.3 Determination of IMQ solubility in different solvents

The solubility of IMQ was investigated by adding an excess amount of IMQ to 5 mL of H_2O, EtOH, MeOH, DMSO, acetone, or ACN. Samples were kept at 30 °C under magnetic stirring until the solid–liquid equilibrium was reached. The equilibrium was checked by measuring drug concentration until it became constant (13 days). Once solid–liquid equilibrium was achieved, supernatant solutions were filtered to ensure they were free of particulate matter before sampling for composition analysis, keeping the temperature at 30 °C during filtration. Filtered supernatant solutions were appropriately diluted and analyzed by HPLC to determine IMQ concentrations. After that, supernatant solutions were kept at 25, 20, 16, or 4 °C to induce IMQ precipitation until solid–liquid equilibrium was reached again. Thus, supernatant solutions were filtered, appropriately diluted, and analyzed by HPLC. The ending time for attainment of equilibrium (2 days) was ascertained by checking the invariability of the concentration.

2.3.2.4 Calorimetric study

Melting point and enthalpy of fusion of IMQ were determined by differential scanning calorimetry (DSC) on an Indium calibrated (onset of melting T_m = 157.1 °C, enthalpy of melting ΔHm = 27.84 J/g) DSC821e (Mettler Toledo Inc., Columbus, United States) equipped with STARe software (Version 11, Mettler Toledo Inc., Columbus, United States). Approximately 5 mg of IMQ was placed in a 40 µL aluminum crucible sealed and pierced twice. DSC scans were carried out between 25 and 320 °C with a heating rate of 10 °C/min and under dry nitrogen purging of 80 mL/min.

2.3.2.5 Preparation of IMQ solutions in different solvents

An excess amount of IMQ was added to 30 mL of carefully degassed H_2O and kept at 25 °C under magnetic stirring for 24 h, then the undissolved IMQ was separated from the solution with 15 min of centrifugation at 25 °C, 10050 × g (NEYA 16R, Remi Elektrotechnik Limited, Mumbai, India). To ensure complete separation of undissolved IMQ, the solution was centrifugated again for 15 min at 25 °C, 10050 × g. The obtained solution of IMQ was then diluted 1:5 with H_2O, obtaining IMQ_H_2O. The same procedure was also applied to EtOH, MeOH, and ACN, with the only difference that the final dilution was 1:50 instead of 1:5; the diluted solutions obtained were then coded as IMQ_EtOH, IMQ_MeOH, and IMQ_ACN. Being IMQ salified in HCl 0.1 M, which makes the solubility in this solvent very high compared to other solvents, a 5 µg/mL solution (IMQ_HCl) was prepared by simply dissolving 0.2 mg of drug in 4 mL of solvent and subsequent 1:10 dilution.

2.3.2.6 UV-Vis absorption spectroscopy of IMQ solutions in different solvents

UV-Vis absorption spectra of IMQ_H_2O were recorded at 25, 40, 60, and 85 °C, of IMQ_EtOH, IMQ_MeOH, and IMQ_ACN at 25, 40, and 60 °C, and of IMQ_HCl at 25 and 85 °C, using a Cary 60 UV-Vis spectrophotometer (Agilent Technologies, Santa Clara, United States) equipped with a 5 cm optical length cuvette for IMQ_H_2O and a 1 cm optical length cuvette for

other solutions. Temperature control was obtained by placing the solution tube in a thermostatic water bath (AREX-6 Digital, VELP Scientifica Srl, Usmate, Italy).

2.3.2.7 IMQ pKa determination

The IMQ pKa was estimated by adding an excess amount of IMQ to HCl 0.037 M for 24 h. After that, solid IMQ was removed by 15 min centrifugation at 25 °C, 10050 × g (NEYA 16R, Remi Elektrotechnik Limited, Mumbai, India), the supernatant pH was measured with a pH meter (SevenCompact™ pH meter S210, Mettler Toledo, Columbus, United States) and IMQ pKa was calculated with Equation 1 [13]:

$$pH = \frac{1}{2}\left(pK_a - \log c\right) \qquad \textit{Equation 1}$$

Where c is the molar concentration of HCl.

2.3.2.8 NMR measurements

NMR spectra were recorded on an AV400 (Bruker, Milan, Italy) spectrometer equipped with a multinuclear cryoprobe. The ppm scale was calibrated on the solvent signals (CD_2HOD resonance peak set at 3.35 ppm, $CHCl_3$ at 7.26 ppm, CD_2HCN at 1.93 ppm, $CD_2HS(=O)CD_3$ at 2.50 ppm). Samples were prepared as follows: 1.5 mg of IMQ were put in a screw cap vial with 1 mL of deuterated solvent. The vial was closed, and the solution was kept at 60 °C for 3 h under magnetic stirring. Then, the solution was allowed to cool to room temperature. When the vial was at room temperature, 0.7 mL solution was filtered and put in an NMR tube. The spectra at high temperatures were recorded after 20 min from the temperature setting.

2.3.2.9 Statistical analysis

All experiments were conducted at least in triplicate. Unless otherwise stated, data are presented as mean value ± standard deviation. Analysis of variance was made with KaleidaGraph (Version 4.5.2, Synergy Software, Reading, PA, USA), and statistical significance was assumed at $p < 0.05$.

2.4 Theory

The ideal solubility (X_2^i) of a solute in a liquid expressed in mole fraction is calculated with Equation 2 [14]:

$$\log X_2^i = -[\Delta H_f (T_0 - T)] RT_0T + \frac{\Delta C_p}{R}\left(\frac{T_0-T}{T} + \ln\frac{T}{T_0}\right) \quad \textit{Equation 2}$$

Where T_0 is the melting point of the solute in absolute degrees, T is the absolute temperature of the solution, R is the gas constant, 1.987 cal/K mol, ΔH_f is the enthalpy of fusion of the solute, and ΔC_p is the difference between the molar heat capacity of the solid and that of the liquid. It has been assumed that the ΔC_p value of a solute in a liquid is approximately equal to the entropy of fusion so that it can be calculated with Equation 3 [14]:

$$\Delta C_p = \frac{\Delta H_f}{T_0} \quad \textit{Equation 3}$$

For regular solutions, the solubility (X_2) of a solute in a liquid is calculated with the Scatchard-Hildebrand equation [15]:

$$-\log X_2 = \frac{\Delta H_f}{2.303RT}\left(\frac{T_0-T}{T_0}\right) + \frac{V_2\phi_1^{\,2}}{2.303RT}(\delta_1-\delta_2)^2 \quad \textit{Equation 4}$$

Where V_2 is the molar volume of the solute, Φ_1 is the volume fraction of the solvent in the saturated solution, and δ_1 and δ_2 are the solubility parameters of the solvent and solute, respectively. In dilute solutions, Φ_1 may be approximated to 1. Equation 4 cannot be applied when solvation or association occurs [15].

2.5 Results and discussion

2.5.1 Forced degradation studies

The solubility studies were carried out for a long time (up to 21 days), implying the risk of a possible degradation of IMQ in solution. For this reason, the analytical method's capability to put possible degradation products into evidence was assessed by conducting forced

degradation studies. HPLC analysis of IMQ exposed to acid hydrolytic conditions gave a chromatogram with a peak at 2 min (Figure 2B). Also, the chromatogram of a freshly prepared IMQ solution showed a peak at 2 min (Figure 2A). Noteworthy, the peak of IMQ exposed to acid hydrolysis presented an area under the curve that corresponded to that expected for the initial IMQ solution concentration (0.2 mg/mL), which suggested the absence of degradation products with the same retention time as IMQ. Analysis of IMQ exposed to oxidative degradation gave a chromatogram with a main peak at 0.7 min, which means that most of IMQ was degraded into uncharacterized products, which eluted at 0.7 min (Figure 2C). These data agreed with previous literature, which reports that IMQ is an exceptionally stable compound and does not undergo degradation upon exposure to acid hydrolysis, but also to photolytic degradation, alkaline degradation, and thermal degradation [16,17]. Therefore, the capability of the HPLC method to identify possible products present was assumed to guarantee the reliability of the IMQ concentration data in solution measured in equilibrium experiments conducted for prolonged times.

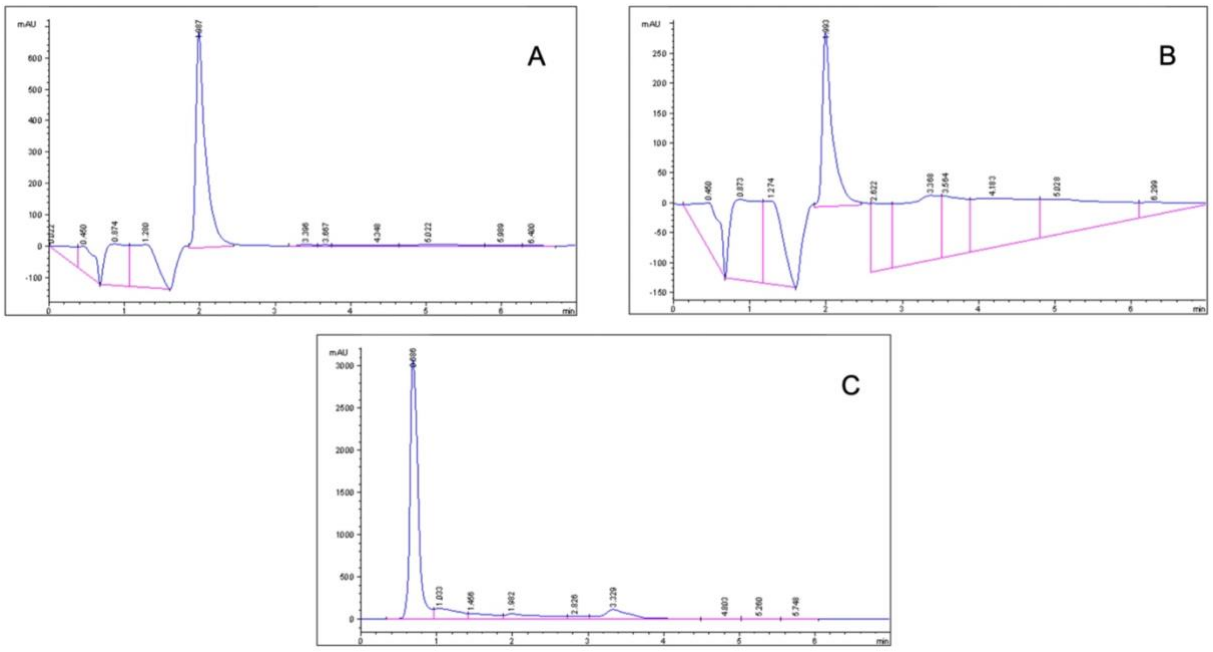

***Figure 2**. Chromatograms of a freshly prepared IMQ standard solution (A), IMQ submitted to acid hydrolytic conditions (B), and oxidative degradation (C).*

2.5.2 Experimental IMQ solubility in different solvents

The IMQ solubility was investigated by adding an excess amount of IMQ to H_2O, EtOH, MeOH, DMSO, acetone, and ACN. Samples were kept at 30 °C under magnetic stirring until the solid–liquid equilibrium was reached. The attainment of the equilibrium was checked by measuring drug concentration until it became constant. Based on preliminarily solubility tests (data not shown), the first measurement was set after 11 days of magnetic stirring. However, such time was insufficient to reach equilibrium because the data variability was extremely high, especially for H_2O and acetone (Figure 3). In addition, after 12 days of magnetic stirring, the measurement was repeated, and the concentrations were slightly higher. One day later the concentrations further increased, and the data variability became negligible. This evidence was interpreted as a sign that equilibrium was reached in all the studied solvents. This observation applied to 4 out of 6 studied solvents. Thus, considering 13 days of magnetic stirring as necessary to attain the equilibrium, it was hypothesized that the discrepancies found in the literature (Table 1) could be partly ascribed to the fact that the IMQ/solvent contact time may not be sufficient to reach the equilibrium. In addition, in the absence of stirring, IMQ concentration in solutions was close or even below the LOD of the calibration curve, whereas, at the same time, with magnetic stirring, the values were significantly higher, which confirms the strong effect of stirring on the peculiar IMQ dissolution.

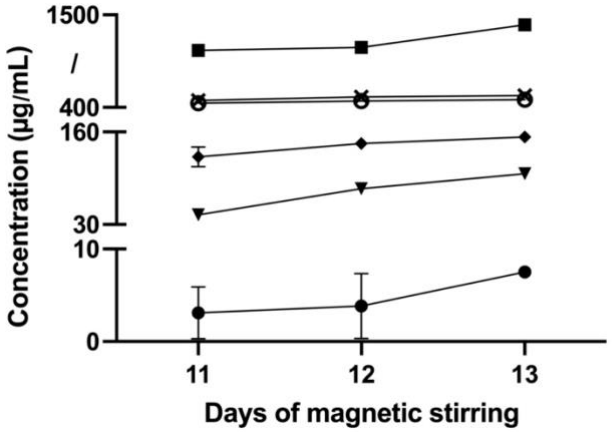

***Figure 3**. Mean concentration of IMQ in the supernatant solutions after 11, 12, and 13 days of magnetic stirring at 30°C in H_2O (solid circle), EtOH (cross), MeOH (open circle), ACN (solid triangle), acetone (solid diamond), and DMSO (solid square). The bars represent the standard deviation (n = 3).*

Experimental solubilities of IMQ in H_2O, EtOH, MeOH, DMSO, acetone, and ACN at 30, 25, 20, 16 and 4 °C are summarized in Table 3.

***Table 3**. Experimental equilibrium solubility values of IMQ in H_2O, EtOH, MeOH, ACN, acetone, and DMSO at 30, 25, 20, 16, and 4 °C expressed in µg/mL. Mean value ± standard deviation (n = 3).*

	30 °C	**25 °C**	**20 °C**	**16 °C**	**4 °C**
H_2O	7.52 ± 0.08	6.10 ± 2.12	-	2.86 ± 0.62	0.58 ± 0.47*
EtOH	541.06 ± 0.42	355.30 ± 41.21	288.96 ± 14.39	270.96 ± 13.70	191.18 ± 4.21
MeOH	491.16 ± 6.41	473.27 ± 7.09	373.25 ± 12.03	356.49 ± 53.90	348.80 ± 20.61
ACN	101.32 ± 4.75	100.14 ± 8.44	101.71 ± 10.76	101.40 ± 11.97	82.93 ± 1.20
Acetone	152.81 ± 3.97	147.15 ± 11.67	149.76 ± 15.44	143.23 ± 2.09	113.12 ± 3.92
DMSO	1382.27 ± 50.52	1116.78 ± 76.07	669.23 ± 6.16	-	-

*Below LOQ

The solubility of IMQ in DMSO at 16 and 4 °C was not determined because DMSO solidifies at temperatures below 20 °C.

It has been reported [6] that slight variations in the pH strongly influence the aqueous solubility of IMQ due to the presence of dissolved anhydrides such as carbon dioxide. We have carefully degassed the solvent to address this issue before adding IMQ. Although solubility values in H_2O at 30 and 25 °C were not statistically different ($p = 0.44$), a clear trend of decreasing solubility is observed as the temperature drops, so much that it is impossible to experimentally determine the solubility at 4 °C as this is below the LOQ. Among literature data (18, 0.6, and 2 µg/mL, Table 1), 0.6 µg/mL, which was measured at 24 °C, is close to the experimental solubility at 4 °C (0.58 ± 0.47 µg/mL), and 2 µg/mL, for which temperature was not provided, is close to the experimental solubility at 16 °C (2.86 ± 0.62 µg/mL).

Data in Table 3 indicate that IMQ solubility in EtOH increased with temperature, ranging from a maximum of about 541 µg/mL at 30°C to a minimum of about 190 µg/mL at 4°C. This suggests that discrepancies in literature data about EtOH solubility of IMQ (180, 240, and 472 µg/mL, Table 1) could be partly ascribed to possible temperature variability at which experiments were conducted. It should also be noted that said literature data lay almost perfectly between the experimental solubility at 30 °C (about 541 µg/L) and 4°C (190 µg/mL).

However, the literature value at 25 °C was significantly lower than that of the present study, likely due to the different IMQ/solvent contact times and the above-evidenced stirring effect.

A similar temperature-dependent solubility was also observed in MeOH, although less pronounced compared to EtOH ($\Delta_{30\text{-}4\ °C}$ solubility in MeOH = 142.36 µg/mL, $\Delta_{30\text{-}4\ °C}$ solubility in EtOH = 349.88 µg/mL). To our best knowledge, the only datum available in the literature is 460 µg/mL, and we assume that it was likely obtained at ambient temperature since it was substantially in agreement with our experimental solubility at 25 °C (about 473 µg/mL).

Solubility values obtained in ACN consistently leveled around 100 µg/mL, and only the value obtained at 4 °C resulted statistically different from that obtained at 30 °C, although at a low level of significance ($p = 0.03$). In any case, these data were higher than the only one reported in the literature (55 µg/mL).

Similarly, all experimental solubilities in acetone ranged between 150 and 140 µg/mL, except for the value recorded at 4 °C, which was statistically different from both experimental solubilities at 30 and 16 °C ($p = 0.01$). Once again, the equilibrium solubility values were higher (although not dramatically) than those available in the literature (96 and 120 µg/mL).

Overall, the variations observed between literature and experimental data of the present study, and between literature data themselves, may be reasonably ascribed to insufficient IMQ/solvent contact time and lack of stirring.

Finally, DMSO solubility values at 30 and 25 °C were positively related to the temperature and quite in agreement with the only one datum available in the literature (1290 µg/mL). At 20 °C, a significant drop of the IMQ concentration in solution was observed. It is worth underscoring that 20 °C is very close to the solidification temperature of the solvent (19 °C).

Finally, it is essential to point out that, as expected for obvious thermodynamic reasons, the attainment of the solid-liquid equilibrium starting from a solid compound required a much longer time (13 days) than that from a cooled-down supersaturated solution (2 days).

2.5.3 Solvent solubility parameter and IMQ experimental solubility

Total (δ_{tot}) and partial (δ_D, δ_P, and δ_H) Hansen solubility parameters at 25 °C were obtained from the literature for H_2O, EtOH, MeOH, and DMSO [15]. For ACN δ_D, δ_P, and δ_H were obtained from the literature [18], while δ_{tot} was computed with Equation 5 [15]:

$$\delta_{tot}^2 = \delta_D^2 + \delta_P^2 + \delta_H^2 \qquad \textit{Equation 5}$$

Where δ_D, δ_P, and δ_H represent dispersion, polar, and hydrogen-bond Hansen solubility parameters, respectively. δ_{tot}, δ_D, δ_P, and δ_H are listed in Table 4. Acetone was not considered, and the reason will be explained in paragraph 2.5.4.

***Table 4**. δ_{tot}, δ_D, δ_P, and δ_H [(cal/cm)$^{1/2}$] for different solvents along with IMQ experimental mean solubility at 25 °C expressed as mole fraction (X_e).*

	δ_{tot}	δ_D	δ_P	δ_H	X_e
H_2O	23.4	7.6	7.8	20.7	$4.59\ 10^{-7}$
EtOH	13	7.7	4.3	9.5	$8.72\ 10^{-5}$
MeOH	14.5	7.4	6	10.9	$8.07\ 10^{-5}$
ACN	12	7.5	8.8	3	$2.22\ 10^{-5}$
DMSO	13	9	8	5	$3.31\ 10^{-4}$

Considering the experimental solubilities of IMQ at 25 °C (Table 3), a correlation between the solubility of IMQ and δ_{tot} was excluded. Similarly, it was possible to exclude a correlation between the solubility of IMQ and one of the three partial solubility parameters.

2.5.4 Fitting of experimental solubilities with ideal and regular solution models

To check whether the experimental solubilities of IMQ in the studied solvents and temperatures fitted the ideal or regular solution models, X_2^i of IMQ was computed with Equation 2. In contrast, X_2 was calculated with Equation 4 considering ΔH_f and T_0 obtained from DSC (Figure 4) as 240 J/g (13.77230 kcal/mol) and 297 °C (570.15 K), respectively.

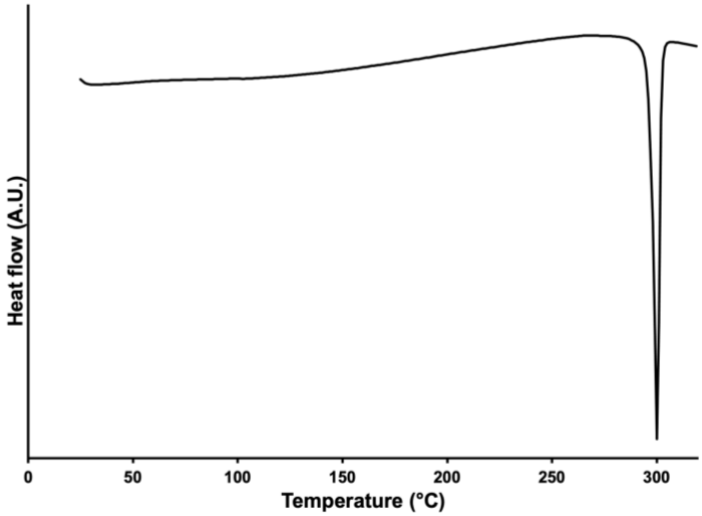

***Figure 4**. DSC trace of IMQ. T_0 = 297 ± 1 °C, ΔH_f = 240 ± 4 J/g.*

V_2 and δ_2 of IMQ were computed according to the Fedors method [19] (Table 5), resulting in 158.9 cm^3/mol and 0.85 $MPa^{1/2}$ [(0.42 $cal/cm^3)^{1/2}$], respectively; Φ_1 was approximated to 1 because the solutions considered were diluted [13].

***Table 5**. Internal energy, molar volume, and Hildebrand solubility parameter of IMQ computed according to the Fedors method [18].*

Group	Group number	ΔE_i (cal/mol)	ΔV_i (cm^3/mol)	E (Kj/mol)	V (cm^3/mol)
CH_3	2	1125	33.5	9.42	67
CH_2	1	1180	16.1	4.94	16.1
CH	1	820	-1	3.43	-1
-CH=	1	1030	13.5	4.31	13.5
C=	3	1030	-5.5	12.94	-16.5
Phenylene	1	7630	52.4	31.94	52.4
Ring closure 5 or more atoms	1	250	16	1.05	16
Conjugate bonds	4	400	-2.2	6.70	-8.8
NH_2	1	3000	19.2	12.56	19.2
N	1	1000	-9	4.19	-9
-N=	2	2800	5	23.45	10
				E_{total} = 114.93 Kj/mol	V_{total} = 158.9 cm^3/mol
				$\delta_2 = (114.93/158.9)^{1/2}$ = 0.85 $MPa^{1/2}$	

Table 6 summarizes X_2^i, X_2, and mean experimental solubilities, expressed as X_e.

Table 6. *X_2^i, X_2, and mean X_e of IMQ in H_2O, EtOH, MeOH, ACN, and DMSO at different temperatures.*

°C	X_2^i	X_2					X_e				
		H_2O	EtOH	MeOH	ACN	DMSO	H_2O	EtOH	MeOH	ACN	DMSO
30	$4.62\ 10^{-4}$	$7.03\ 10^{-66}$	$1.60\ 10^{-23}$	$4.29\ 10^{-28}$	$5.97\ 10^{-13}$	$1.60\ 10^{-23}$	$5.66\ 10^{-7}$	$1.33\ 10^{-4}$	$8.37\ 10^{-5}$	$2.24\ 10^{-5}$	$4.10\ 10^{-4}$
25	$3.78\ 10^{-4}$	$4.63\ 10^{-67}$	$5.41\ 10^{-24}$	$1.22\ 10^{-28}$	$3.04\ 10^{-13}$	$5.41\ 10^{-24}$	$4.59\ 10^{-7}$	$8.72\ 10^{-5}$	$8.07\ 10^{-5}$	$2.22\ 10^{-5}$	$3.31\ 10^{-4}$
20	$3.08\ 10^{-4}$	$2.78\ 10^{-68}$	$1.76\ 10^{-24}$	$3.30\ 10^{-29}$	$1.51\ 10^{-13}$	$1.76\ 10^{-24}$	-	$7.10\ 10^{-5}$	$6.36\ 10^{-5}$	$2.25\ 10^{-5}$	$1.98\ 10^{-4}$
16	$2.60\ 10^{-4}$	$2.73\ 10^{-69}$	$6.99\ 10^{-25}$	$1.13\ 10^{-29}$	$8.48\ 10^{-14}$	$6.99\ 10^{-25}$	$2.15\ 10^{-7}$	$6.65\ 10^{-5}$	$6.08\ 10^{-5}$	$2.25\ 10^{-5}$	-
4	$1.55\ 10^{-4}$	$1.74\ 10^{-72}$	$3.72\ 10^{-26}$	$3.72\ 10^{-31}$	$1.36\ 10^{-14}$	$3.72\ 10^{-26}$	$4.37\ 10^{-8}$	$4.69\ 10^{-5}$	$5.95\ 10^{-5}$	$1.84\ 10^{-5}$	-

The solutions considered were neither ideal nor regular because the values of X_2^i and X_2 significantly differed from X_e.

It was obvious that the studied IMQ solutions could not be ideal. Still, it was not evident that they were not regular, so it was worth investigating why IMQ solubilities cannot be fitted with Equation 4. As mentioned, Equation 4 cannot be applied when solvation or association occurs [15]. The hypothesis of solvation, namely the formation of extensive and strong hydrogen bonds between IMQ and the solvent, was unlikely because of the measured low solubility values even though the effect of the apolar moiety of the molecule cannot be disregarded. On the other hand, association, which implies interactions between like molecules in solution, was highly possible thanks to both intermolecular hydrogen bonds involving the lone pair of the nitrogen atoms and the $-NH_2$ group, and to the π-π interactions due to intermolecular overlapping of *p*-orbitals in the π-aromatic system. These two intermolecular bonding types (hydrogen bonding and π-stacking) can contribute to the association phenomenon differently, depending on the solvent used. Strong intermolecular hydrogen bonds, particularly favored by the geometric complementarity of the H-donor and H-acceptor groups, were already highlighted in the IMQ crystal structure [20] and should be mainly favored in apolar solvents or low polar aprotic solvents, such as ACN, compared to high polar aprotic solvents, such as DMSO, and dipolar protic solvents, such as MeOH and H_2O. Conversely, the π-stacking is favored in aqueous solution, thanks to the contribution of the hydrophobic interaction [21]. To confirm these hypotheses, the UV-Vis absorption spectra of IMQ and ^1H NMR spectra were

registered in different solvents and temperatures. In particular, IMQ_H_2O, IMQ_EtOH, IMQ_MeOH, and IMQ_ACN were recorded at 25, 40, and 60 °C. For IMQ_H_2O, the spectrum at 85 °C was also recorded. The spectrum of IMQ in DMSO was not considered because of the high UV cutoff of this solvent. In the case of H_2O, a 5 cm optical length cuvette was selected to increase the absorbance due to the very low solubility of IMQ in this solvent.

The obtained UV-Vis absorption spectra of IMQ_H_2O, IMQ_EtOH, IMQ_MeOH, and IMQ_ACN are presented in Figure 5.

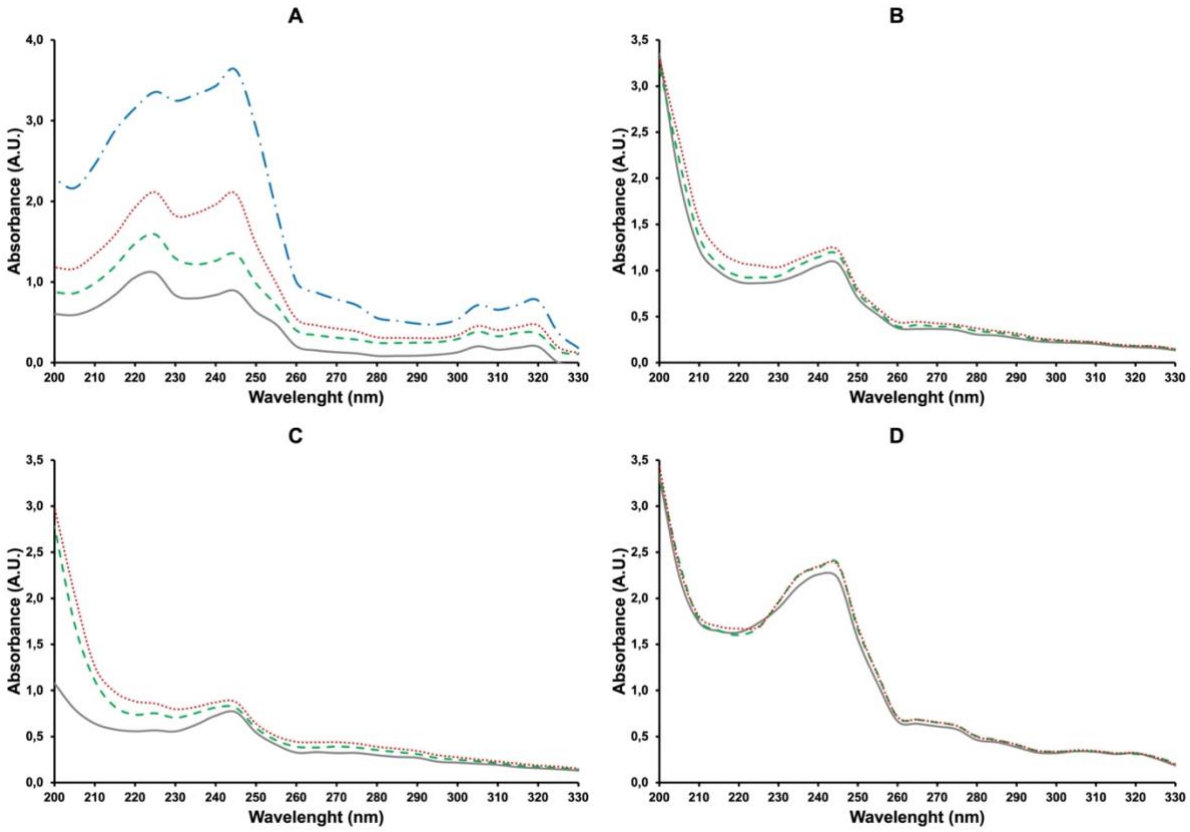

***Figure 5**. UV-Vis absorption spectra of solutions of IMQ in H_2O (A), EtOH (B), ACN (C), and MeOH (D) at 25 (grey solid line), 40 (green dashed line), 60 (red dotted line), and 85 (blue dashdotted line) °C.*

In the case of H_2O (Figure 5A), two main absorption peaks were observed at 225 and 245 nm, followed by two secondary peaks at 305 and 320 nm. The absorbance increased significantly with the temperature, reaching very high values for the spectrum recorded at 85 °C, with the position of the peaks unchanged.

In the case of the organic solvents, this effect was also present, although much less pronounced than H_2O, and was almost negligible for MeOH (Figure 5D). We can exclude that

the increase in the absorbance was due to the evaporation of the solvent since the experiments were conducted with great care by capping the test tubes with tight screw caps to avoid any evaporation and transferring the solution from the test tube to the reading cuvette as quickly as possible. In addition, the observed phenomenon was the least with the most volatile solvent (MeOH).

The phenomenon of increased absorbance with temperature is known as the hyperchromic effect, which is typically observed on DNA heat denaturation, but can also apply to small molecules such as IMQ, and it is due to the increase in the molar extinction coefficient of the solution, ε [22]. As evident from Figure 5, the hyperchromic effect was very pronounced in the case of the most polar solvent, which is H_2O [23]: in a very polar solvent, IMQ hydrophobic molecules tended to associate to lower the system's free energy through intermolecular interactions. The increase in temperature increased the molecular kinetic energy, which resulted in breaking these bonds. It is known that the stacking interaction decreases the absorption intensity of the aromatic chromophores, giving rise to hypochromism [21]; consequently, the loss of these interactions resulted in a hyperchromic effect. Also, the break of intermolecular hydrogen bonds can contribute to a hyperchromic effect, with the lone pairs of nitrogen atoms more available for influencing the electronic energy of the *p*-orbitals in the π-aromatic rings, affording, in turn, an increase in the ε value, even if an expected bathochromic effect was not observed.

To verify the correctness of this interpretation, UV-Vis absorption spectra of IMQ_HCl at 25 and 85 °C were recorded. Being IMQ a weak base, we expect that in HCl 0.1 M N3 and N5 are both protonated [6], making the intermolecular hydrogen bonding impossible and preventing the stacking between charged molecules. The obtained spectra are reported in Figure 6.

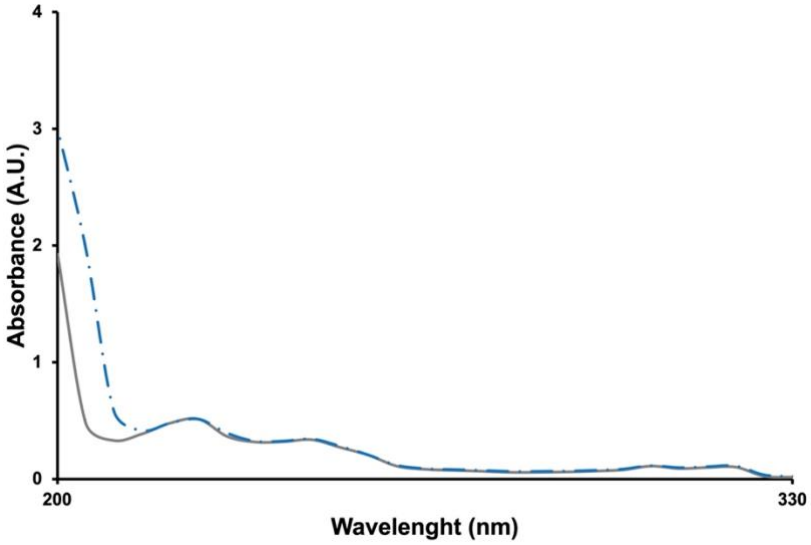

***Figure 6**. UV-Vis absorption spectra of a solution of IMQ in HCl 0.1 M at 25 (grey solid line) and 85 (blue dashdotted line) °C.*

It can be observed that, as expected, the hyperchromic effect was absent, and the salified IMQ lost the capacity to associate.

The IMQ pKa was computed from Equation 1 by measuring the pH of a saturated IMQ solution in diluted HCl and resulted in 6.52 ± 0.07. IMQ pKa can be found only in a few discordant literature reports. The first one (pKa = 5.4) is reported by Layek et al. but, unfortunately, the method of measurement/calculation, or a possible bibliographic reference, is not provided [24]. The second one (pKa = 7.3) was calculated using the Henderson-Hasselbach equation by extrapolating to zero methanol concentration the apparent pKa measured in water-methanol solutions [6]. The third paper [25] reports a pKa of 6.8 based on the spectroscopic analysis in water at different pH, and it was attributed to the quinoline nitrogen. Interestingly, this value is not significantly different from the experimental value determined in this work.

NMR studies were performed to further explain the solubility behavior of IMQ in different solvents. Unfortunately, because of the extremely low water solubility of IMQ, the NMR spectrum in D_2O could not be registered. Figure 7 reports the spectrum region of aromatic protons (7.0 - 8.3 ppm) with the attribution of the signals. These signals are the most influenced by the aggregation phenomena and could add some information on the solvation of IMQ.

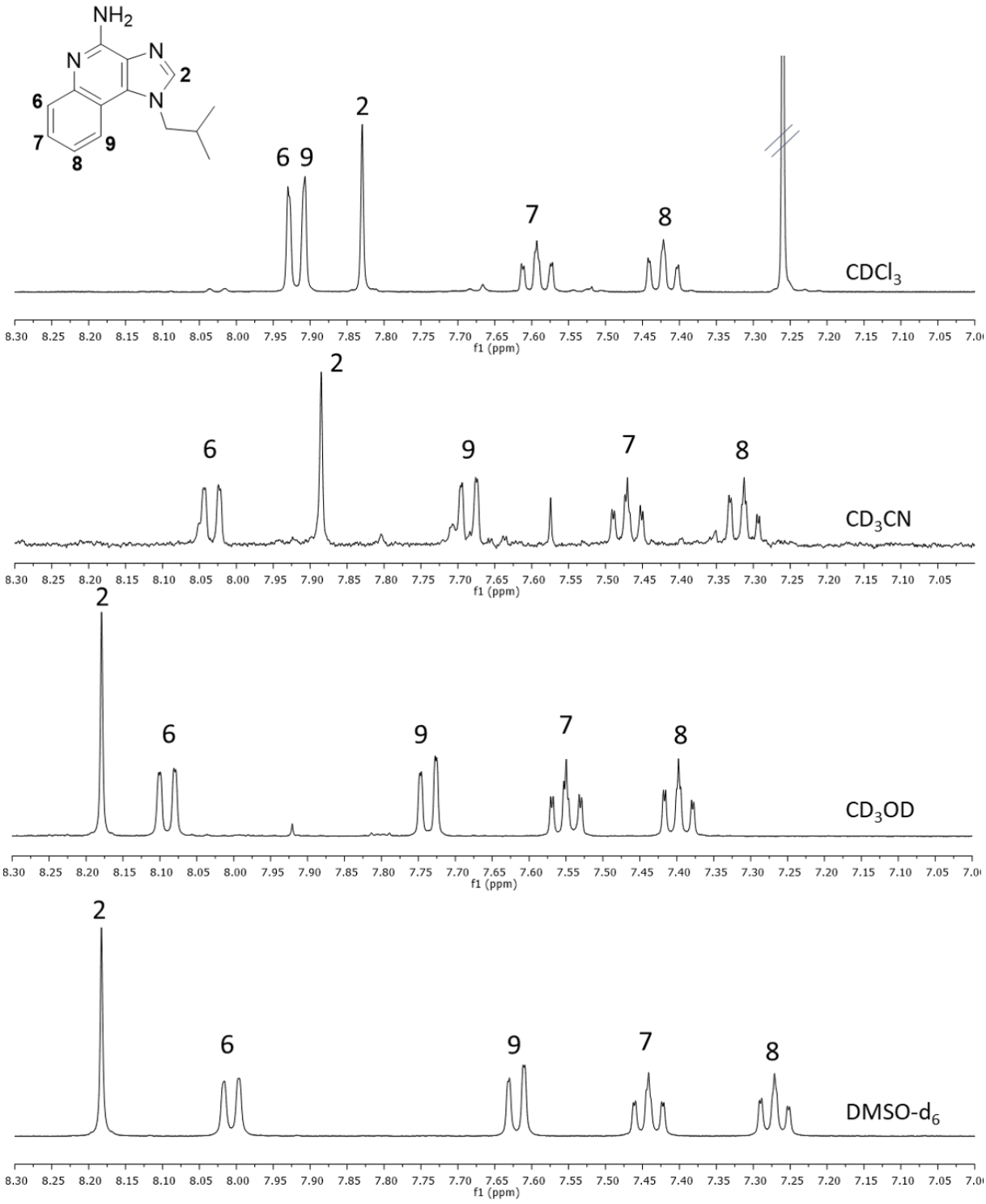

***Figure 7**. [1]H NMR spectra of IMQ, 400 MHz at 25 °C (spectrum region 7.00-8.30 ppm).*

The chemical shifts change significantly depending on the solvent, and the ones that shift most are the signals of the protons close to the nitrogen atoms (H2, H6, and H9). The pattern of the signals in DMSO is very similar to that in MeOH, indicating a similar kind of solvation. It looks like both solvents can break intermolecular H-bonding and solvate the amino group in the 4-

position. DMSO is a significantly better hydrogen-bond acceptor than ACN [26] and, in fact, the signal of H2 in CD_3CN is less deshielded, with a value closer to that in $CDCl_3$. The spectrum in acetone (Figure 8A) could not be compared with the others because it is clear the presence of a mixture of molecules likely due to the formation of an imine between the -NH_2 of IMQ and carbonyl of the solvent. This hypothesis is confirmed by the NMR spectrum taken by adding about 10% v/v D_2O into the NMR tube containing the IMQ-acetone solution: a remarkable reduction of the complexity of the signals was observed (Figure 8B), indicating that most of the species were in equilibrium with IMQ.

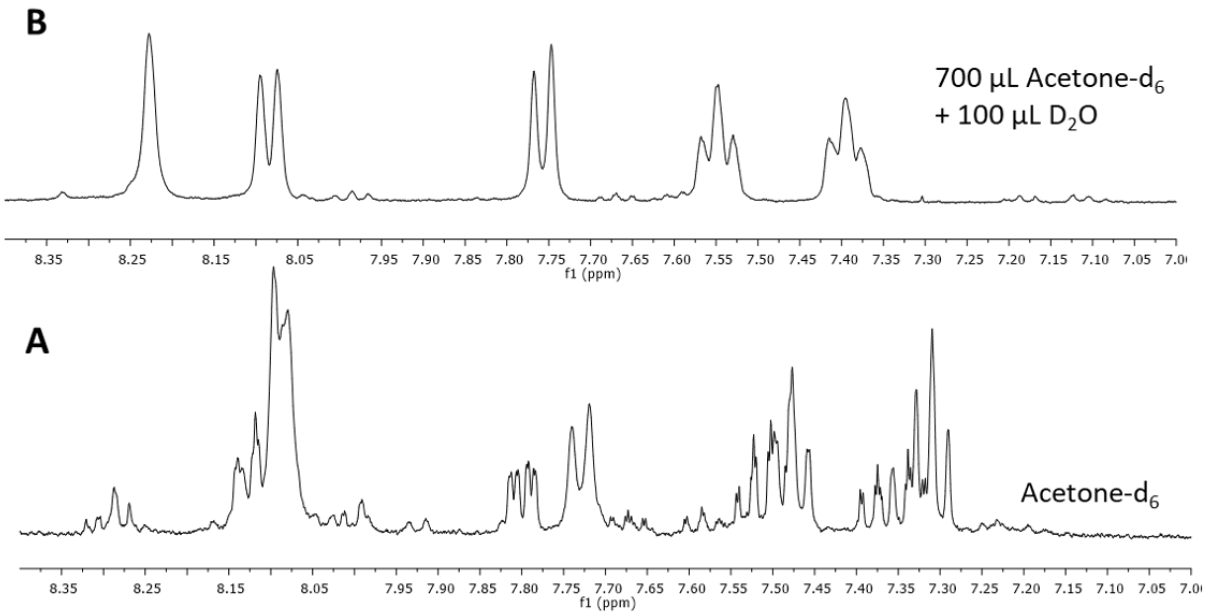

***Figure 8**. [1]H NMR spectra of IMQ in acetone (A) and acetone added with about 10% v/v D_2O (B) (400 MHz) (spectrum region 7.00-8.35 ppm).*

We also carried out NMR experiments at 60 °C (Figure 9) and, in every case, we recorded a high-field shift of the signal of H2, confirming that when higher kinetic energy is provided to the system, the H-bonding involving N3 is weakened.

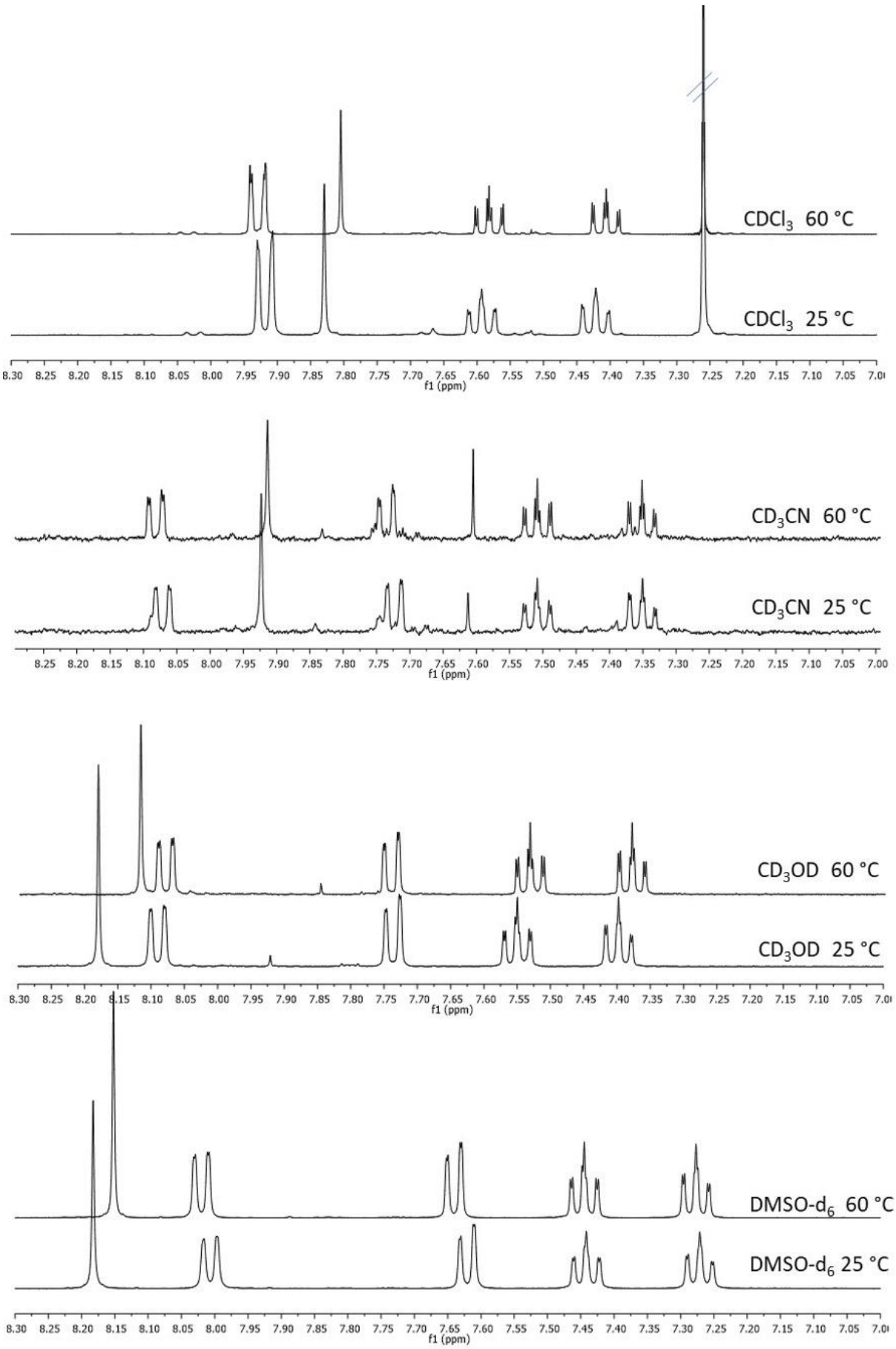

Figure 9. *^{1}H NMR spectra of IMQ, 400 MHz at 25 and 60 °C (spectrum region 7.00-8.30 ppm).*

2.6 Conclusions

This work systematically studied IMQ solubility in H_2O, EtOH, MeOH, ACN, acetone, and DMSO at different temperatures to collect robust and reliable data, which are difficult to catch from the literature due to significant discrepancies. These inconsistencies in IMQ solubility in several solvents found in the literature are likely due to the different experimental conditions, such as temperature, IMQ/solvent contact time, stirring mechanism, and intensity.

The strong influence on the solubility of IMQ of IMQ/solvent contact time and agitation and of the temperature in the case of H_2O, EtOH, and MeOH is confirmed. IMQ requires about two weeks to reach solid-liquid equilibrium in the studied solvents.

Experimental solubilities show that IMQ solutions in the solvents considered were not ideal. They are not even regular and do not follow the Scatchard-Hildebrand equation. We demonstrated that this behavior, as well as the literature discrepancies, can be explained by considering the fact that IMQ molecules give rise to association due to the intermolecular hydrogen bonds involving the lone pair of the nitrogen atoms and the $-NH_2$ group and to the π-π interactions due to intermolecular overlapping of *p*-orbitals in the π-aromatic system, as indicated by the hyperchromic effect observed in UV-Vis absorption spectra recorded at different temperatures, as well as NMR spectra. This phenomenon is more evident in very polar solvents, such as H_2O, where IMQ molecules tend to associate to lower the system's free energy. This hypothesis is strengthened by the absence of the hyperchromic at pH values much below the pKa of IMQ, such as in HCl 0.1 M where IMQ salifies, thus making the lone pair no longer available to form intermolecular bonds.

Finally, IMQ solubility values measured in acetone cannot be considered reliable due to the reaction with the solvent leading to the formation of new species, such as imine, in solution.

3 CHAPTER II: DEVELOPMENT AND CHARACTERIZATION OF A RESPIRABLE IMQ POWDER FOR INNATE IMMUNITY STIMULATION

This chapter allowed the writing of the article 'Imiquimod powder for inhalation to stimulate innate immunity' submitted on 27 February 2024 to *Journal of Drug Delivery Science and Technology*, to which Daisy Sorgi contributed with conceptualization, methodology, investigation, writing of the original draft.

3.1 Introduction

3.1.1 Innate immunity

Innate immunity comprises two main branches: the afferent arm, responsible for perceiving infections, and the efferent arm, dedicated to eliminating them. Both arms can be divided into cellular and humoral components [27].

3.1.1.1 The cellular components of innate immunity

The cellular components are myeloid cells, which include mononuclear and polymorphonuclear phagocytes. Mononuclear phagocytes encompass macrophages and dendritic cells, originating from monocytes and playing a crucial role in presenting antigens to T cells within the adaptive immune system. Macrophages are widely distributed throughout the body, within the parenchyma of major organs like the heart, brain, lung, and liver. They exhibit diverse morphologies, such as the spindle-shaped tissue histiocyte, the flattened Küpffer cell of the hepatic sinusoids, and the stellate microglial cell of the central nervous system. Osteoclasts, a type of macrophage, also exist. Dendritic cells take on various forms, including the skin's Langerhans and the spleen's plasmacytoid dendritic cells. Macrophages exhibit the ability to engulf and eliminate microbes, and through chemotactic cytokines, they can attract other myeloid cells, particularly polymorphonuclear phagocytes, to the infection site.

Additionally, macrophages and dendritic cells are pivotal in initiating the adaptive immune response by presenting antigens to $CD4^+$ T cells using class II MHC antigens. Polymorphonuclear phagocytes comprise neutrophils, basophils, and eosinophils. Neutrophils specialize in killing pathogens, whereas eosinophils and basophils are primarily involved in generating mediators that shape the inflammatory environment and respond to cytokines released by the adaptive immune system. While these cells are less abundant than neutrophils, eosinophils can be significantly produced during parasitic infections or because of allergic adaptive immune responses. Mast cells, tissue-dwelling descendants of the myeloid line, share a similar role with eosinophils and mediate allergic responses [27].

The innate immune system typically identifies pathogens through receptors specifically designed to recognize microbial molecules that are essential components of microbes and, for this reason, are less prone to alteration through mutation and selection. To a significant extent, innate immune receptors need to remain indifferent to molecules of host origin, forming the foundation for the innate immune system's ability to distinguish between self and non-self [27].

Among the molecules detected by the innate immune system, one of the most extensively studied is lipopolysaccharide [27], which was discovered to be recognized by TLR4 [28,29]. This discovery made it possible to identify ten TLRs in humans, which play a significant role in microbial sensing. Each TLR recognizes one or more specific ligands from bacteria, fungi, protozoa, and viruses. Certain TLRs form heteromeric complexes with others, expanding the range of microbial stimuli that can signal via the TLR, while others appear to work on their own. Once the host detects the presence of a microbe, it initiates the process of killing it. In the phagosomes of neutrophils and macrophages, reactive oxygen intermediates are generated through a sequence of reactions initiated by NADPH oxidase. These reactive oxygen intermediates effectively eliminate microbial targets by interacting with various molecules within them, including lipids, proteins, and nucleic acids. However, it's important to note that these reactive oxygen intermediates, effective against microbes, can also cause substantial injury to the host’s healthy tissues [27].

Before leukocytes in the periphery can engulf and destroy microbes, they must first reach the site of infection. In a localized infection, chemotactic mediators, especially proteins from the chemokine family, are released alongside cytokines like interleukin 1 and tumor necrosis factor and autacoid substances such as histamine, bradykinin, and other small molecules. Autacoids induce localized vasodilation, increasing the blood volume in the infected area. Leukocytes slow down their rolling along the vessel surface and eventually adhere to it, a crucial step preceding diapedesis, which is the process through which leukocytes cross the vascular barrier. Tumor necrosis factor and interleukin 1 play key roles in promoting the presence of leukocytes, slowing down their rolling, and facilitating their adhesion to the vessel. Chemokines, such as interleukin 8 (IL-8), further stimulate leukocyte diapedesis and chemotaxis in the extravascular space [27].

3.1.1.2 The humoral components of innate immunity

In extracellular compartments, microbes and host molecules, usually proteins, may engage in direct and specific contact for sensing microbes. However, it's important to note that these plasma proteins, while involved in the detection process, cannot kill microbes on their own [27].

Several extracellular proteins, such as complement, lysozyme, lactoferrin, and antimicrobial peptides, are recognized for killing microbes. Lysozyme functions by enzymatically breaking down the cell walls of both Gram-negative and Gram-positive bacteria [27]. Lactoferrin helps to eliminate bacteria by modifying their motility and disrupting their ability to form biofilms [30]. Complement proteins and antimicrobial peptides are primarily intracellular and are constitutively expressed in mammals. Complement is a group of proteolytic enzymes that can be activated through three distinct pathways (classical, properdin, and MASP), all triggered by microbes. Activation of the complement cascade results in various effects, including the opsonization of microbes for phagocytosis by C3b, the generation of inflammatory and chemotactic C5a, and the assembly of a ring-shaped structure from C5 through C9, which can lyse Gram-negative bacteria and inactivate viruses. Antimicrobial peptides in mammals include

defensins and cathelicidins, respectively expressed in neutrophils and epithelia. Both families are known for their ability to disrupt biological membranes and exhibit high specificity for microbial cells [27].

Infections typically induce various secondary effects within the host, including fever, a decrease in plasma iron, and the production of proteins like haptoglobin, fibrinogen, and serum amyloid A, each of which may contribute to the immune response in different ways [27].

3.1.1.3 The bridge between innate and adaptive immunity

The origins of adaptive immunity trace back to the innate immune system that precedes it, which is evident in the fact that antigen presentation occurs through specialized molecules known as class I and class II MHC antigens found on innate immune cells. However, merely presenting antigens to the T cell receptor via MHC antigens is insufficient to trigger an adaptive immune response. Additional stimuli are required, which involve the upregulation of surface molecules like CD80, CD86, and CD40. These molecules interact with specific activating receptors on T cells, such as CD28 and CTLA, to initiate the adaptive response. The upregulation of co-presentation antigens is believed to contribute to the adjuvant effect of various microbial products [27]. In this regard, the adjuvant effect of LPS was first observed almost 70 years ago [31].

3.1.1.4 Innate immunity in the lungs

In the airways, the main cellular components of innate immunity are the epithelium, macrophages, dendritic cells, natural killer cells, and neutrophils [32].

The nasopharynx, middle ear, paranasal sinuses, and conducting airways (trachea, bronchi, bronchioles) are lined by a ciliated pseudostratified columnar epithelium with tight junctions among cells that prevent paracellular permeation. Additionally, it features submucosal glands that contribute to forming a protective mucus layer, typically 5-10 µm thick. The mucus contains mucins, negatively charged glycosylated proteins, and traps pathogens. The coordinated

movement of lung cilia, directed towards the trachea, facilitates the removal of trapped pathogens through mucociliary motility. Remarkably, this mechanism allows the lungs to eliminate approximately 90% of inhaled particles. In addition to being a physical barrier, the respiratory epithelium is responsible for maintaining the volume and composition of the airway surface liquid (ASL) and regulates the secretion of functional compounds with bacteriostatic or bactericidal activity. ASL provides the antimicrobial molecules secreted by cells with the optimal microenvironment to perform their functions. Cathelicidins, for example, are small cationic peptides released by neutrophil granules with a bactericidal action whose positive surface charges interact with the negative charges of the mucins present in the ASL, allowing strategic placement on the lung surface for timely pathogen neutralization. Functional compounds in the ASL with bacteriostatic or bactericidal activity include lysozyme, an enzyme capable of hydrolyzing the β-glycosidic bonds of peptidoglycan, and lactoferrin, which sequesters ions essential for microbial survival. Additionally, there may be a synergistic antimicrobial effect between proteins in the ASL and small cationic peptides produced by immune system cells and the respiratory epithelium. This collaborative action enhances the overall antimicrobial defense in the respiratory tract [32].

Surface epithelia are the most common entry point for pathogenic microorganisms, so an essential function of the airway's innate immune system is the rapid recognition and initiation of appropriate responses. The ability to distinguish between self and non-self is due to pattern recognition receptors recognizing conserved molecular patterns originating from diverse microorganisms, including bacteria, viruses, fungi, and protozoans. These receptors include TLRs, Nod1, and Nod2. TLRs, specifically TLR2 and TLR4, have been extensively studied in the airways. TLR2 acts as a receptor for di- and triacylated lipopeptides from mycobacteria, lipoteichoic acid, zymosan, and other molecules. It is present in human airway epithelia and resident macrophages. TLR4, on the other hand, recognizes LPS and various bacterial, viral, and parasitic proteins. Nod1 and Nod2 are cytoplasmic receptors responsible for intracellular detection of bacterial peptidoglycan. Nod1 recognizes peptides containing an amino acid found

mainly in Gram-negative bacteria, whereas the ligand for Nod2 is a dipeptide present universally in bacterial peptidoglycans. Thus, Nod2 is considered a general bacteria sensor, while Nod1 detection is more specific to Gram-negative bacteria [32,33].

3.1.2 Vaccine adjuvants

An adjuvant is formulated as a part of a vaccine and aims to enhance the immune response [34].

Thus far, adjuvants employed in human vaccines approved by the FDA and European Medicines Agency include aluminum salt-based vaccine adjuvants, oil-in-water emulsion adjuvants, and TLR agonist-based adjuvants [34].

Aluminum-containing adjuvants were introduced almost a century ago in diphtheria vaccines because the diphtheria toxoid alone could not produce sufficient antibody response [34,35]. Aluminum salt-based adjuvants in FDA-approved vaccines include aluminum hydroxide, aluminum phosphate, and amorphous aluminum hydroxyphosphate sulfate. All aluminum salts have specific physicochemical properties, affecting their immunostimulatory activity [34,36]. Mechanisms proposed to explain the adjuvant effect of aluminum-containing adjuvants are depot effect with continuous antigens release and presentation to immune cells, enhanced antigen uptake and presentation by antigen-presenting cells, the NLRP3 inflammasome activation, induction of the differentiation of $CD4^+$ T cells in Th2 cells, perturbation of dendritic cell membrane which further lead to antigen uptake and upregulation of $CD4^+$ T cells, and complement activation [34].

Oil-in-water emulsions were introduced in the late 1980s to increase the immunogenicity of new protein antigens produced through recombinant DNA technology [34]. MF59, approved for human vaccines in Italy in 1997, comprises squalene, polysorbate 80, sorbitan trioleate, and trisodium citrate dihydrate, and is primarily used in influenza vaccines. It enhances antigen uptake at the injection site and, involving antigen-presenting cells, the antigen transportation to the draining lymph nodes. AS03, which appeared for the first time on the European market

in 2009, plays an important role in influenza and malaria vaccines. It comprises squalane, polysorbate 80, and DL-α-tocopherol, and it can trigger the production of cytokines and chemokines in both muscle tissue and draining lymph nodes, leading to the recruitment of monocytes, dendritic cells, and granulocytes into the lymph nodes. Furthermore, AS03 has demonstrated the ability to stimulate a specific immune response mediated by $CD4^+$ T cells [34].

Cytosine phospho-guanosine oligodeoxynucleotides are synthetic DNA molecules, TLR9 agonists, which appeared in 2017 in an FDA-approved hepatitis B vaccine. AS04, used in HPV and HBV vaccines, appeared on the market for the first time in 2009. It is an adjuvant formed by an aluminum salt as a platform on which a TLR agonist is adsorbed. In particular, 30-O-deacylated monophosphoryl lipid A (MPL), a detoxified LPS, is a TLR4 agonist. AS01B is an adjuvant developed by GlaxoSmithKline Biologicals in the recombinant zoster vaccine Shingrix, which was FDA-approved in 2017 and is formulated in liposome with MPL and QS-21; this latter purified from *Quillaja Saponaria* [34].

Currently, numerous vaccine adjuvants are in various stages of clinical trials, including lipid-based adjuvants, emulsions, saponins, nucleotides, cytokines, and others [34].

3.1.3 Potential therapeutic uses of TLR agonists

There is strong evidence that TRL agonists administered directly to the lung can increase defenses against pathogens that enter the body through the respiratory tree. In this regard, very promising is PUL-042, an inhaled therapeutic currently in the clinical stage based on two synthetic TLR agonists, activating the innate immune system within the lungs for rapid and efficient protection against a broad spectrum of pathogens, including viruses, bacteria, and fungi. Animal studies, including those involving immunosuppressed models, have demonstrated its effectiveness. Phase I/2a clinical trials showed that PUL-042 is well-tolerated in healthy individuals and those with chronic obstructive pulmonary disease. Additionally, exploratory phase 2 trials have showcased its anti-viral properties. Future phase 2 studies will

evaluate PUL-042's efficacy in preventing respiratory complications such as pneumonia and its potential to enhance outcomes in immunocompromised cancer patients [37]. The underlying concept lies in the so-called trained immunity: cells of the innate immune system appear to be able to gain memory characteristics after transient stimulation, resulting in an enhanced response upon secondary challenge. Trained immunity is characterized by nonspecific increased responsiveness and explains the heterologous effects of vaccines, which result in increased protection against secondary infections [38].

TLR agonists have been tested not only to prevent infections, but also to improve their course. In this regard, the first of two phase 2 clinical trials undertaken with the support of the US Department of Defense to evaluate PUL-042 against COVID-19 showed that patients treated with inhaled PUL-042 had a statistically significant reduction in the time to improve the combined respiratory symptoms of cough and shortness of breath [39]. Similarly, the intranasal delivery of IMQ in mice reduced viral replication, bodyweight loss, and airway inflammation following influenza A virus infection [40]. Moreover, it has been recently reported that in a murine model of respiratory syncytial virus infection, intranasal administration of IMQ improves the course of the acute disease as evidenced by decreased weight loss, reduced viral lung titers, and attenuated airway inflammation [41]. IMQ has also been proposed to help eliminate SARS-CoV-2, at least during the early phases of infection, thanks to its ability to offer good stimulation of innate and acquired immunity [42].

Since TLR agonists' immunomodulatory action stimulates anti-allergic T lymphocyte responses, they can potentially be exploited as adjuvants in allergen immunotherapy for allergic rhinitis and asthma. In this respect, synthetic TLR4 and TLR9 agonists are being tested in clinical trials, while TLR2, TLR5, and TLR7 agonists showed anti-allergic properties in both *in vitro* and *in vivo* experiments [43]. In general, an inhalation therapy based on TLR7 agonists might be successful for allergic asthma because they can produce airway relaxation and suppress Th2 immune responses, contrasting bronchoconstriction and allergic inflammation. In this context, it has been demonstrated that guinea pig tracheal segments cultured for 3 days

with IMQ, a TLRs 7 and 8 agonist, reduced the airway contractile responses to 5-hydroxytryptamine. Consequently, activation of TLR7 might prevent the development of airway hyperresponsiveness due to the action on the airway smooth muscle [44]. Moreover, IMQ produced a rapid dose-dependent relaxation of methacholine-contracted human airway smooth muscle strips *in vitro*. This TLR7-mediated relaxation was also found in inflamed guinea pigs' airways *in vivo* [45]. An inhalation therapy based on TLR7 agonists might also be helpful because, as stated above, it prevents viral respiratory infections, one of the leading causes of asthma exacerbations [44]. In this regard, it is essential to point out that cardiovascular effects in humans due to TLR7 agonism are implausible because human systemic and pulmonary vascular endothelium does not express TLR7 [45].

As stated in paragraph 3.1.2, among FDA-approved adjuvants employed in human vaccines, there are TLR agonists. In this regard, IMQ has been proposed in association with the recombinant hepatitis B surface antigen within multifunctional chitosan nanocapsules as a new nanotechnology-based nasal vaccination intended to elicit specific humoral and cellular immune responses [46].

The implications of these findings lead to the potential use of agents stimulating the immune system, including TLR agonists like IMQ, to prevent and fight infectious diseases, but also as adjuvants in allergen immunotherapy, for example, for asthma and in association with antigens for the formulation of vaccines for inhalation or nasal administration.

3.1.4 Inhalation drug delivery

Inhalation has been used for thousands of years to administer drugs [47] and, nowadays, it is used for three primary purposes: the maintenance therapy of asthma and chronic obstructive pulmonary disease with bronchodilators and glucocorticosteroids, topical delivery in various uncommon conditions such as cystic fibrosis and pulmonary arterial hypertension, and systemic applications [48]. Recently, increasing attention in new therapeutic areas of interest for inhalation drug delivery has been observed: antibiotic lung delivery to treat lung infectious

diseases like bronchiectasis, tuberculosis, and cystic fibrosis-associated infections, vaccine lung delivery against viral infections like influenza and measles, lung delivery of systemically acting drugs that cannot effectively be orally delivered like insulin for diabetic patients or levodopa for Parkinson patients in an off-period, and drugs that need a rapid onset of action like fentanyl [49].

3.1.4.1 Advantages of inhalation administration

In comparison with the oral route of administration, inhalation presents some benefits. Regarding topically acting drugs, pulmonary delivery offers advantages such as the possibility of using a relatively low dose, a reduced occurrence of systemic side effects, and, for specific medications, a rapid onset of action [48,50]. Pulmonary delivery of systemically acting drugs permits the avoidance of injections for drugs with poor absorption through the gastrointestinal tract. Additionally, it can provide more favorable pharmacokinetic profiles, such as achieving plasma levels of insulin in a timescale appropriate for meal-time delivery [48,51]. Furthermore, inhalation administration allows the self-administration of the drug, removing the need for intervention by medical staff, which would be of great help, for example, in an influenza pandemic, a situation in which large-scale administration is necessary and where healthcare facilities typically have limited capacity.

3.1.4.2 Obstacles in inhalation drug delivery

The inhalation administration of drugs is a relatively intricate process because the respiratory tract has developed defense mechanisms designed to prevent inhaled substances from entering the lungs and eliminate or deactivate them upon deposition [48,50]. In summary, the defense mechanisms within the lungs that an inhaled drug particle may confront can be categorized as mechanical, chemical, and immunological. Mechanical barriers are represented, for example, by the lungs' structure itself, the impact and consequent loss of inhaled drug particles and droplets in large airways, the effects of diseases like airway narrowing, mucus hypersecretion, and mucus plugging, and the removal of the drug by lung

mucociliary clearance. Chemical barriers include drug degradation by proteolytic enzymes and effects of other chemicals like surfactants, while an immunological barrier is the particle engulfment by alveolar macrophages. Besides, there are also behavioral barriers, including non-adherence to the treatment regimen and poor inhaler technique [48], which are factors attributable to the patient and not to the lung.

3.1.4.3 Respiratory tree's structure

As mentioned above, the respiratory tree's structure represents an obstacle to accessing and depositing exogenous agents, such as drugs, in the lower airways, a process necessary to achieve the desired therapeutic effect. In this regard, a detailed description of the respiratory tree will be provided. For this purpose, one of the most used models is Weibel's [52], which distinguishes 23 subsequent bifurcations of the airways, starting at the trachea (generation 0) with a diameter of 18 mm (for adults) that decrease to 0.41 mm in the alveolar sac (generation 23) [53] (Figure 10).

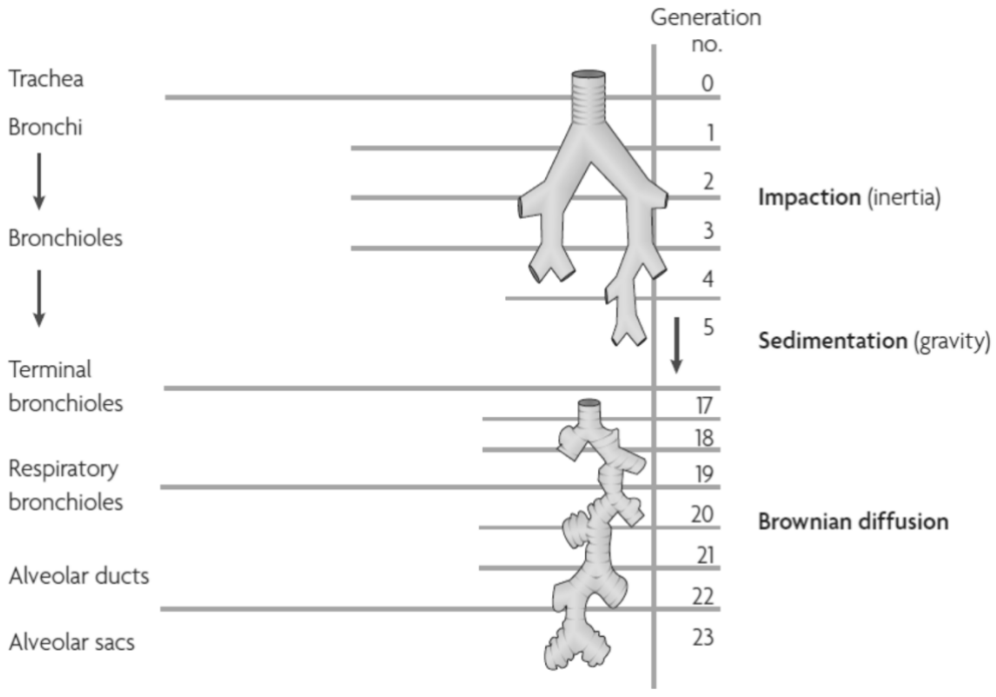

***Figure 10**. Airways structure according to Weibel's model* [54].

In the respiratory system, two primary sections can be identified: the conducting region, spanning generations 0 to 16, and the respiratory region, spanning generations 17 to 23. The conducting airways consist of the trachea, which divides into right and left bronchi, which branch into bronchioles with gradually diminishing diameters. The function of this region is to form a path for the conduction of inhaled air. In contrast, the respiratory airways initiate with the respiratory bronchioles and include all structures involved in the gas exchange, such as alveolar ducts and sacs [55].

3.1.4.4 Deposition mechanisms

Inhaled drugs could deposit or be trapped in the respiratory tract mainly through impaction, sedimentation, and diffusion (Figure 10). Impaction occurs in the upper airways and involves larger particles: due to their inertia, they deviate from the airflow, collide with the walls of the airway duct, and are consequently removed. In the middle airways, slightly smaller particles deposit by sedimentation under gravity. Finally, for tiny particles, particle motion is determined by Brownian diffusion, which accounts for the dominant mechanism of deposition in the alveolar region [54]. Finally, less relevant mechanisms that can determine deposition in the airways are turbulence, electrostatic precipitation, and interception [56]. Turbulent mixing denotes the mixing experienced by fluid in a turbulent regime. In this state, the fluid speed and, consequently, the trajectories of particles continuously undergo fluctuations in both magnitude and direction. Ultimately, these particles may deposit on the walls of airways due to the dynamic nature of turbulent flow. Electrostatic precipitation occurs when an electrically charged particle approaches a surface in the airways, inducing an opposite charge, with consequent electrostatic attraction and deposition. Interception is the process by which particles, while following the main flow, contact an airway wall due to their specific shape and size, which could be the dominant factor for elongated particles, such as fibers [57].

3.1.4.5 Factors that affect the deposition

Among factors attributable to the formulation aspect that influence the location and extent of the deposit within the lungs, the most important is the aerodynamic diameter, which is the most appropriate measure of aerosol particle size. Aerodynamic diameter (D_{ae}) is defined by the diameter of an equivalent volume sphere of unit density (D_{eq}) with the same terminal settling velocity as the actual particle. For particles larger than 1 μm, the relationship between these dimensions can be expressed with Equation 6 [58]:

$$D_{ae}=D_{eq}\sqrt{\frac{\rho_p}{\rho_0 X}} \qquad \textit{Equation 6}$$

Where ρ_p and ρ_0 are particle and unit density, respectively, and χ is the dynamic shape factor. χ, which is equal to 1 in the case of a sphere, is a dimensionless measure of the deviation from sphericity and is the ratio of the actual resistance force experienced by the non-spherical falling particle to the resistance force experienced by a sphere with the same volume [58]. Particles larger than 5 μm tend to deposit predominantly in the upper and larger airways, limiting the aerosols reaching the deeper lung regions. Particles within the range of 2 to 5 μm deposit mainly in the central and small airways, while particles smaller than 2 μm primarily deposit in the alveolar region [56]. Since the aerodynamic diameter of a particle is influenced by the square root of its density, the aerodynamic diameter can be decreased by decreasing particle density [58]. As a result, even particles with a geometric particle size around 20 μm can be made in the respirable aerodynamic diameter range [59].

In addition to aerodynamic diameter, the location and extent of deposition within the lung are influenced by other aerosols' physical properties, such as hygroscopicity and electric charge. he hygroscopicity of a particle, in fact, can influence its deposition in the lungs, for example due to the change in crystallinity and morphology following the absorption of moisture from the environment [58].

All these factors, combined with possible variables from the patient, such as lung geometry, age, gender, breathing style, and diseases, from the formulation and the inhalation device, make ad efficient inhalation drug delivery extremely challenging.

3.2 Aim

This second chapter aimed to design an IMQ powder for inhalation administration that is potentially useful in future preclinical or clinical studies aimed at evaluating its ability to stimulate the immune response in the airways for broad-spectrum, short-term protection against infections, but also its potential use in fighting infectious diseases, as adjuvant in allergen immunotherapy or in vaccines for pulmonary or nasal administration. Besides the technological development and characterization, a first biological evaluation was carried out through *in vitro* studies aimed at investigating the toxicity of this IMQ inhalation powder on a lung cell line and elucidating the powder's potential ability to induce a controlled production of inflammatory cytokines.

3.3 Materials and methods

3.3.1 Materials

- Acetone (C_3H_6O, Acetone ≥99%, TECHNICAL, VWR International, Radnor, United States)
- ACN (CH_3CN, Acetonitrile ≥99.9%, HiPerSolv CHROMANORM®, analytical grade for HPLC, VWR International, Radnor, United States)
- Calu-3 cells (American Type Culture Collection, Manassas, United States)
- 100x20 mm culture dishes (Corning®, New York, United States)
- DMSO (C_2H_6OS, Dimetilsolfossido ≥99.9% USP, Multi-Compendial, J.T.Baker®, Avantor, Radnor, United States)
- Dulbecco's Modified Eagle's Medium with 1000 mg/L of D-Glucose Anhydrous, 584 mg/ml of L-Glutamine and 5958 mg/ml of Hepes Free Acid (DMEM, Biowest, Nuaillé, France)

- EtOH (C_2H_6O, Etanolo ≥96% (v/v) Reag. Ph. Eur., Supelco®, VWR International, Radnor, United States)
- Fetal bovine serum (FBS, Gibco™, Thermo Fisher Scientific, Waltham, United States)
- Hank's balanced salt solution (HBSS, Corning®, New York, United States)
- Human IL-6 ELISA Kit (Product Number #RAB0306, Merck Millipore, Burlington, United States)
- Human IL-8/CXCL8 ELISA Kit (Product Number #RAB0319, Merck Millipore, Burlington, United States)
- Hydrochloric acid 37% (HCl, Ph. Eur., Lot #18F064006, VWR International, Radnor, United States)
- Imq_RM ($C_{14}H_{16}N_4$, Lot #210307, Dayang chem Co., Ltd., Hangzhouzhejiang, China)
- Lactohale 100 (LH100, $C_{12}H_{22}O_{11}$, Lot #743632, DFE Pharma, Goch, Germany)
- Lipopolysaccharide (LPS, lipopolysaccharide from Escherichia coli O111:B4, Sigma-Aldrich, Saint Louis, United States)
- The generic term ‘medium’ stands for DMEM supplemented with 10% FBS, 1% MEM Nonessential Amino Acids Solution 100X, and 1% Penicillin-Streptomycin Solution 100X
- MEM Nonessential Amino Acids Solution 100X (Corning®, New York, United States)
- MeOH (CH_3OH, Metanolo ≥99.8%, HiPerSolv CHROMANORM® Reag. Ph. Eur., HPLC grade, VWR International, Radnor, United States)
- Milli-Q water was purified (0.055 µS/cm, TOC 1 ppb) with Purelab pulse + Flex ultra-pure water (Elga Veolia, Milan, Italy)
- 3-(4,5-dimethylthiazol-2-yl)-2,5-diphenyl tetrazolium bromide (MTT, Sigma-Aldrich, Saint Louis, United States)
- Penicillin-Streptomycin Solution 100X (Corning®, New York, United States)
- PG ($C_3H_8O_2$, FU USP, ACEF; Fiorenzuola d’Arda, Italia)
- Potassium chloride (KCl, POTASSIO CLORURO FU-BP-Ph.Eur., Lot #M0118701, ACEF; Fiorenzuola d’Arda, Italia)

- Potassium dihydrogen phosphate (KH_2PO_4, potassio fosfato monobasico anidro E 340, Lot #H1191004, ACEF; Fiorenzuola d'Arda, Italia)
- Sodium chloride (NaCl, Sodio cloruro 99.0-100.5% Ph. Eur., USP, BP, Lot #20E074106, VWR International, Radnor, United States)
- Sodium phosphate dibasic anhydrous (Na_2PO_4, Sodio fosfato bibasico, anidro ≥99.0%, AnalaR NORMAPUR® ACS, Reag. Ph. Eur. per analisi, VWR International, Radnor, United States)
- Triethylamine ($C_6H_{15}N$, Thermo Fisher Scientific, Waltham, United States)
- Tween 20 ($C_{58}H_{114}O_{26}$, TWEENTM 20 HP-LQ-(MH), Lot #0000810410, Croda International, Snaith, United Kingdom)

3.3.2 Methods

3.3.2.1 Production of IMQ spray-dried particles

IMQ spray-dried particles (Imq_SD) were produced from IMQ raw material (Imq_RM) that was dissolved under magnetic stirring at two concentrations, 250 µg/mL and 375 µg/mL, in three solvents, EtOH and two mixtures of propylene glycol (PG) and EtOH, at 1:9 and 2:8 volume ratio, respectively. These solutions were subjected to spray drying to obtain Imq_SD employing a Mini Spray Dryer B-290 (BÜCHI Labortechnik AG, Flawil, Switzerland) with the following process parameters: nebulization pressure 5 bar, nebulization gas rate 1686 L/h (at standard conditions), drying air flow rate (aspiration) 27 m^2/h, solution feed rate 3 mL/min and spray nozzle diameter 0.7 mm. The inlet temperature was set to 80 °C for the solution in EtOH, 127 °C for PG:EtOH 1:9, and 155 °C for PG:EtOH 2:8. The abovementioned conditions are summarized and numbered in Table 7. The spray dryer was combined with the Inert Loop B-295 (BÜCHI Labortechnik AG, Flawil, Switzerland) to work in a closed loop configuration using N_2 as nebulizing gas. The yield of the spray drying process was calculated for each condition as the percentage ratio between the quantity of solute dissolved in the solvent and the quantity of powder collected at the end of the process.

***Table 7**. Conditions of the spray drying process.*

Condition	Solvent	Inlet temperature (°C)	Concentration (µg/mL)
1	EtOH	80	250
2	EtOH	80	375
3	PG:EtOH 1:9	127	250
4	PG:EtOH 1:9	127	375
5	PG:EtOH 2:8	155	250
6	PG:EtOH 2:8	155	375

3.3.2.2 Production of IMQ micronized particles

IMQ micronized particles (Imq_M) were produced by micronization of Imq_RM using a spiral jet mill (LaboMill-1, FPS Food and Pharma Systems, Fiorenzuola d'Arda, Italy) fed with nitrogen with a Venturi pressure of 8.2 bar, a ring pressure of 7 bar, and a feed rate of 0.6 g/min. The yield of the micronization process was calculated as the percentage ratio between the quantity of Imq_RM fed in the micronizer and the amount of Imq_M collected at the end of the process.

3.3.2.3 Scanning electron microscopy

The morphology and surface characteristics of Imq_RM, Imq_SD, and Imq_M were visually investigated via scanning electron microscopy (SEM) using a FESEM SUPRATM 40 (Carl Zeiss, Jena, Germany). Each powder sample was deposited on adhesive black carbon tabs mounted on aluminum stubs to allow charge dispersion. The particles in excess were gently removed with a nitrogen flow. The samples were analyzed, without metalization, under high vacuum conditions, 1.33×10^{-2} Pa for 30 min, and the images were collected using an accelerating voltage of 1 kV at different magnifications, from 500X to 10000X for Imq_RM, from 500X to 30000X for Imq_M and from 1000X to 30000X for Imq_SD.

3.3.2.4 Particle size distribution

Images acquired via SEM at 10000x, 20000x, and 30000x magnifications were used to determine the arithmetic mean diameter of Imq_M and Imq_SD obtained under conditions listed in Table 7 using ImageJ software (NIH, Bethesda, MD, USA). More precisely, at least 300 particles were manually measured for each condition and divided into dimensional ranges from 300 to 4950 nm, using 50 nm as a dimensional range from one interval to the next. The obtained results were used to construct the cumulative undersize distribution. The particle size distribution of Imq_RM, Imq_M, and Imq_SD obtained under condition 2 as reported in Table 7 (the latter selected for reasons that will be explained later) was also determined using laser diffraction (Spraytec®, Malvern Panalytical, Worcestershire, United Kingdom). Briefly, 10 mg of powder were dispersed in 10 mL of water with the help of two drops of 2% w/v Tween 20 solution in water. The sample was sonicated (8510, Branson Ultrasonics Corporation, Danbury, USA) for 3 min at 40 kHz. Data were expressed as volume diameter of the 50^{th} percentile of the particle population and Span value, which measures the width of the distribution and is calculated with Equation 7:

$$\text{Span} = \frac{Dv90 - Dv10}{Dv50} \qquad \textit{Equation 7}$$

Where Dv10 and Dv90 are the 10^{th} and 90^{th} percentiles of the particle population, respectively.

3.3.2.5 Thermogravimetric analysis

Thermogravimetric analysis (TGA) performed with the TGA/DSC1 instrument (Mettler Toledo Inc., Columbus, United States) was used to evaluate the residual content of solvents in Imq_SD. An accurately weighed quantity, approximately 5 mg, of Imq_SD was placed in a 40 µL aluminum crucible and heated in the temperature range between 25 and 140 °C with a heating rate of 10 °C/min under nitrogen purging of 80 mL/min.

3.3.2.6 DSC

DSC analyses were performed on Imq_RM, Imq_M, and Imq_SD with indium calibrated (onset of melting T_m = 157.1 °C, enthalpy of melting ΔH_m = 27.84 J/g) DSC821e (Mettler Toledo Inc., Columbus, United States) driven by a STARe software (Version 11, Mettler Toledo Inc., Columbus, United States): accurately weighed quantities, approximately 5 mg, of powder samples were placed in a 40 µL aluminum crucible, which was then sealed and pierced twice. DSC traces were acquired between 25 °C and 320 °C with a heating rate of 10 °C/min and under nitrogen purging of 100 mL/min.

3.3.2.7 Powder X-ray diffraction

Powder X-ray diffraction (PXRD) analysis was performed on Imq_RM, Imq_M, and Imq_SD. XRPD data were collected in Bragg−Brentano geometry with Cu Kα radiation and Ni filter on a Smartlab XE diffractometer (Rigaku, Tokyo, Japan) with a solid-state Hypix3000 2D detector. 0.05° incident and receiving Soller slits were used. The degree of crystallinity, C, was assumed to be 100% for Imq_RM and was calculated for Imq_SD and Imq_M with Equation 8:

$$C = 100R_X \qquad \textit{Equation 8}$$

R_x is the ratio between the area under the X-ray diffraction pattern of the powder in the 2θ range 1.5-35° and the area under the X-ray diffraction pattern of Imq_RM in the same range. Areas were computed using KaleidaGraph software (Version 4.5.2, Synergy Software, Reading, PA, USA).

3.3.2.8 Density measurement

The skeletal density of IMQ was measured with a gas pycnometer (AccuPyc II 1340 Gas Displacement Pycnometry System, Micromeritics Instrument Corporation, Norcross, United States). The instrument was first calibrated with a 1 cm^3 stainless steel sphere; then, 250 mg of Imq_RM were accurately weighed, placed in a 3.5 cm^3 measuring sealed cell, and inserted into the sample chamber. Helium was introduced to the sample chamber, and then expanded

into a second empty chamber with a known volume. The pressure observed after filling the sample cell and the pressure discharged into the expansion chamber was measured. Thus, the volume was calculated. The density was determined by dividing the sample weight by the volume measured.

3.3.2.9 HPLC

IMQ was quantified by HPLC analysis with an Agilent 1200 Series (Agilent Technologies, Santa Clara, United States) driven by ChemStation software version B.04.03-SP1 and using a UV detector set at a wavelength of 242 nm. The HPLC method was developed by adapting the one described by Ghezzi et al. [2] and Telò et al. [5]. The mobile phase, composed of 180 volumes of MeOH, 270 volumes of ACN, 530 volumes of water, and 5 volumes of triethylamine, was pumped at a flow rate of 0.9 mL/min through a reverse-phase C_{18} column (Kinetex C18 2.6 µm, 100 Å, 100 × 4.6 mm, Phenomenex, Torrance, United States) kept at 29 °C. In these conditions, the retention time of IMQ was about 2 min. The injection volume for each sample was 10 µL. The analytical method was assessed regarding the linearity of response (AUC vs. concentration) in the 4–100 µg/mL concentration range. LOD and LOQ were calculated as the analyte concentration at 10 and 33% RSD of the RSD versus IMQ concentration curve, respectively, and are equal to 0.69 ± 0.43 and 2.09 ± 1.29 µg/mL, respectively.

3.3.2.10 Preparation of adhesive mixtures and homogeneity evaluation

Four adhesive mixtures (each of about 1 g) with lactose LH100, two of Imq_M named Imq_M1L and Imq_M5L, and two of Imq_SD named Imq_SD1L and Imq_SD5L, were manually prepared in a mortar employing the geometric dilution method with 1:99 and 5:95 % weight ratio, respectively. The compositions of mixtures are summarized in Table 8. The homogeneity of the prepared mixtures was checked at the end of the manual mixing procedure. For each adhesive mixture, three samples of about 20 mg each were collected from different spots of the powder bed, then each sample was dissolved in HCl 0.1 M and analyzed via HPLC. Homogeneity was assumed at a coefficient variation (CV), calculated as the percentage of the

ratio between the standard deviation and the mean value of the three measurements, lower than 5%.

***Table 8**. Composition of adhesive mixtures expressed in % w/w.*

Adhesive mixture	Imq_SD (% w/w)	Imq_M (% w/w)	Lactose LH100 (% w/w)
Imq_SD1L	1	-	99
Imq_SD5L	5	-	95
Imq_M1L	-	1	99
Imq_M5L	-	5	95

3.3.2.11 Purity evaluation of Imq_SD

Three accurately weighted quantities of Imq_SD were dissolved in 0.1 M HCl; then, the solutions were analyzed with HPLC. Imq_SD were considered pure if the solution concentration found with HPLC analysis was between 95% and 105% of that expected.

3.3.2.12 In vitro aerodynamic assessment

The aerodynamic performance of Imq_M, Imq_SD, Imq_SD1L, Imq_SD5L, Imq_M1L, and Imq_M5L was investigated with an Andersen Cascade Impactor (ACI; Apparatus 3, USP 41, Copley Scientific, Nottingham, United Kingdom) upon aerosolization of the powders with a mid-high resistance device (RS01®, Plastiape, Osnago, Italy). Before running the experiment, 2 mL of a solution of Tween 20 at 2% w/v in EtOH was applied to the particle collection surface of each stage so that after complete solvent evaporation, a thin layer of surfactant was obtained on the stage surfaces, ensuring efficient particle capture and avoiding particle bouncing. The system was connected to a vacuum pump (SCP5Super Capacity Pump, Copley Scientific, Nottingham, United Kingdom), creating the airflow necessary to aerosolize the powder and entrain it into the ACI. The flow rate used during each test was adjusted according to USP-NF <601>, with a critical flow controller (TPK, Copley Scientific, Nottingham, United Kingdom) to produce a pressure drop of 4 kPa over the inhaler. Thus, a flow rate of 60 L/min was set before each experiment using a flow meter (DFM 2000 Copley Scientific, Nottingham, United Kingdom). The pump was activated for 4 s in each test, so a total volume of 4 L of air was

drawn through the inhaler during the experiment. At the flow rate of 60 L/min, the cut-off diameters of stages −1, −0, 1, 2, 3, 4, 5, and 6 were the following: 8.60, 6.50, 4.40, 3.20, 1.90, 1.20, 0.55 and 0.26 μm (USP-NF <601>). A glass microfiber filter (Whatman, Little Chalfont, United Kingdom) was placed right below stage 6 to collect particles with a diameter smaller than 0.26 μm. The drug was recovered from the apparatus by washing with HCl 0.01 N. The powder deposited in the induction port (IP) was solubilized in 50 mL of HCl 0.01 N. The glass microfiber filter, at the end of the aerosolization, was transferred in a glass crystallizer, washed with 20 mL of HCl 0.01 N, and put in an ultrasonic bath (8510, Branson Ultrasonics Corporation, Danbury, USA) for 15 min at 40 kHz to allow the complete dissolution of the powder deposited and filtered with RC filters (Minisart® RC, 0.45 μm regenerated Cellulose, Sartorius). The solutions obtained were analyzed by HPLC, as reported above. The test was executed by loading the device with a size 3 Quali-V® HPMC capsules (Qualicaps, Madrid, Spain) manually filled either with 5 mg of Imq_M or Imq_SD, or 20 mg of Imq_M, Imq_SD, Imq_SD1L, Imq_SD5L, Imq_M1L or Imq_M5L; 20 mg of Imq_SD1L or Imq_M1L corresponded to 0.2 mg of the active ingredient, while 20 mg of Imq_SD5L or Imq_M5L to 1 mg. For each aerosolization test, the content of one capsule for Imq_M and Imq_SD, three capsules for Imq_SD5L and Imq_M5L, and four capsules for Imq_SD1L and Imq_M1L was discharged. These conditions are summarized in Table 9. The quantification of the drug deposited in the impactor allowed for calculating the following aerodynamic parameters: the delivered dose (DD) as the amount of drug collected from IP to F, the fine particle dose (FPD) as the mass of the drug with an aerodynamic diameter lower than 5 μm calculated from the log-probability plot fitting equation, and the fine particle fraction (FPF) as the ratio between FPD and DD in percent. The mass median aerodynamic diameter (MMAD) was determined by plotting the cumulative percentage of mass less than the stated aerodynamic diameter for each ACI stage on a probability scale versus the aerodynamic diameter of the stage on a logarithmic scale. The emitted dose (ED) is the percentage ratio between the powder delivered from the capsule upon aerosolization and the loaded quantity.

***Table 9**. Conditions of each ACI test.*

Powder	Capsules discharged for each ACI test	Loaded powder dose in one capsule (mg)
Imq_SD	1	5, 20
Imq_SD1L	4	20
Imq_SD5L	3	20
Imq_M	1	5, 20
Imq_M1L	4	20
Imq_M5L	3	20

3.3.2.13 Cell culture

Calu-3 cells, used between passages 4-8, were grown in culture dishes incubated at 37 °C, 5% CO_2, 95% relative humidity, and cultured in medium (see paragraph 3.3.1 for details). For *in vitro* tests, cells were seeded in a 48-well plate at a density of 50.000 cells per well (in 400 µL of medium) and incubated until the cells were attached and formed a monolayer (24 or 48 h).

3.3.2.14 Determination of IMQ solubility in medium

The solubility of IMQ in the medium was investigated by adding an excess amount of Imq_RM to 2 ml of the medium under magnetic stirring for 72 h at 37 °C. At the end of the 72 h, the medium was filtered and centrifugated twice for 10 min at 10050 × g (NEYA 16R, Remi Elektrotechnik Limited, Mumbai, India) to ensure that it was free of undissolved Imq_RM and subsequently deprived of proteins by precipitating them with acetone: the 2 ml of filtered supernatant was added to 8 ml of cold acetone (-20 °C), vortexed, incubated for 60 min at -20°C, centrifugated for 10 min at 10050 × g (NEYA 16R, Remi Elektrotechnik Limited, Mumbai, India) and, finally, analyzed by HPLC for the accurate determination of IMQ concentration.

3.3.2.15 Cell stimulation

Cells seeded in a 48-well plate with a density of 50.000 cells/well were exposed for 24 h to three different concentrations of a suspension of Imq_SD or Imq_RM in medium, namely 5,

25, and 45 µg/ml, or to a 5 µg/ml solution of Imq_RM in medium. A solution of 10 µg/ml of LPS in medium was used as a positive control. In contrast, the medium alone was used as a negative control. Table 10 summarizes all the conditions to which cells were exposed. 400 µL of solution, suspension, or medium was placed in each well for each condition.

***Table 10**. Conditions to which cells were exposed for 24 h.*

Condition	Treatment
A	medium (negative control)
B	Imq_RM 5 µg/ml solution in medium
C	Imq_SD 5 µg/ml suspension in medium
D	Imq_SD 25 µg/ml suspension in medium
E	Imq_SD 45 µg/ml suspension in medium
F	Imq_RM 5 µg/ml suspension in medium
G	Imq_RM 25 µg/ml suspension in medium
H	Imq_RM 45 µg/ml suspension in medium
I	10 µg/ml LPS solution in medium (positive control)

About 1.5 mg of Imq_SD were added to 1 ml of HBSS and 24 µL of a 2% w/v Tween 20* solution in water for preparing conditions from C to E. Tween 20 was added as it was essential to break up any powder agglomerates and help obtain a homogeneous suspension. Moreover, to make the suspension as homogeneous as possible, it was subjected twice to intermittent vortexing followed by sonication for 15 min (2510 Ultrasonic Cleaner, Branson Ultrasonics, Brookfield, United States). Finally, an appropriate volume of the homogeneous suspension thus obtained was diluted in a proper medium volume to get the desired concentrations, namely 5, 25, and 45 µg/ml.

The procedure described above was followed for the preparations of conditions from F to H; only Imq_RM was used instead of Imq_SD.

*The absence of toxic effect of Tween 20 on cells at this concentration was previously evaluated.

For the preparation of condition B, 1 mg of Imq_RM was dissolved in 1 ml of DMSO, and an appropriate volume of the obtained 1 mg/ml solution was diluted in a proper volume of medium to get a 5 µg/ml final concentration of IMQ.

At the end of 24 h of treatment, the medium of each well was analyzed for the presence of interleukin 6 (IL-6) and IL-8, as described in paragraph 3.3.2.17, while cell viability analysis was performed, as described in paragraph 3.3.2.16. Each condition was repeated 6 times in the same 48-well plate, and 2 48-well plates were tested.

3.3.2.16 Cell viability analysis

The effect of 24 h of treatment with conditions from A to I (Table 10) on the viability of cells was studied with the MTT test. Briefly, the medium in each well was removed and replaced with 200 µL of a 0.5 mg/ml solution of MTT in HBSS. The 48 well-plate was incubated at 37 °C, 5% CO_2, and 95% relative humidity for 3 h, then the MTT solution in each well was removed and replaced by 200 µL of DMSO. To ensure complete solubilization of the formed blue formazan crystals, the plate was placed on a microplate shaker for 15 min (MTS 2/4 digital, Ika Werke, Staufen im Breisgau, Germany). Finally, the absorbance values were read at 570 nm using a fluorescence microplate reader (Spark™ 10M multimode microplate reader, Tecan, Männedorf, Switzerland). The cell viability was expressed as a percentage of negative control, set at 100% metabolic activity.

3.3.2.17 IL-6 and IL-8 immunoassays

IL-6 and IL-8 production was measured with enzyme-linked immunosorbent assay (ELISA) on medium. The medium was fresh and optimally diluted just before the assay so that the IL-6 and IL-8 concentrations fit the kit's standard curve range. The protocol followed is that described by the manufacturer.

3.3.2.18 Statistical analysis

All experiments were conducted at least in triplicate. Unless otherwise stated, data are presented as mean value ± standard deviation. Analysis of variance was made with KaleidaGraph (Version 4.5.2, Synergy Software, Reading, PA, USA), and statistical significance was assumed at $p < 0.05$.

3.4 Results and discussion

3.4.1 Imq_SD production by spray drying and micronization

EtOH and PG were selected as solvents to dissolve Imq_RM to produce Imq_SD because of their acceptable toxicity profile [60,61] and suitability for the formulation of pharmaceutical products, as well as for their different physicochemical properties (vapor tension, density, and viscosity). The spray drying process was performed under six conditions (Table 7), keeping the process parameters constant, except for the inlet temperature, which was selected to be higher than the boiling point of the used solvent or mixtures of solvents. The purpose was to evaluate the possible influence of the solvent and the concentration of the starting solution on the morphology and size distribution of Imq_SD obtained. Regarding EtOH and PG mixtures, inlet temperatures were chosen according to the liquid-vapor equilibrium diagram for the EtOH-PG system [62]. Therefore, for conditions 5 and 6, the first attempts were carried out with an inlet temperature of 145 °C, which did not allow the total evaporation of the solvent, being the collected powder still wet. Likely, the residual liquid corresponded to the solvent with the lowest vapor pressure, namely PG, having EtOH at 20 °C a vapor pressure more than 500 times higher than PG (5.79 kPa vs 10.6 Pa, respectively) [63]. This assumption was confirmed by TGA, which showed a mass loss of about 27% between 25 and 140 °C. A further powder was thus manufactured with an inlet temperature of 155 °C. However, also this attempt was unsuccessful because Imq_SD obtained was not completely dried. The explanation is attributable to the fact that the solution has a boiling point higher than that reported for the

EtOH-PG binary system at the given composition [62] due to the ebullioscopic contribution of the solute. In fact, unlike what happened for condition 6, for which IMQ concentration was 375 µg/mL, Imq_SD obtained under condition 5, for which IMQ concentration was 250 µg/mL, were completely dry, even if the solvent mixture was the same. Consequently, PG:EtOH 2:8 was discarded as a potential solvent for producing Imq_SD by spray drying because of the high inlet temperature required for producing dry particles.

The micronization process had a yield of 48%.

Table 11 shows process yields for micronization and spray drying under conditions tested (Table 7).

***Table 11**. Process yields of the spray drying process under conditions listed in Table 7.*

Process	Process yield (%)
Micronization	48
Spray drying (condition 1)	13
Spray drying (condition 2)	20
Spray drying (condition 3)	10
Spray drying (condition 4)	20
Spray drying (condition 5)	9
Spray drying (condition 6)	8

Process yields for spray drying were very low, which is very common because the cyclone often does not separate fine particles, which are then lost in the filter [64], while process yield for micronization is considerably higher than those obtained with the spray drying process. However, the process yield was not the focus of this part of the work.

3.4.2 Scanning electron microscopy

The morphology of Imq_RM (Figure 11), Imq_M (Figure 12), and Imq_SD obtained under conditions listed in Table 7 (Figure 13) were assessed through SEM.

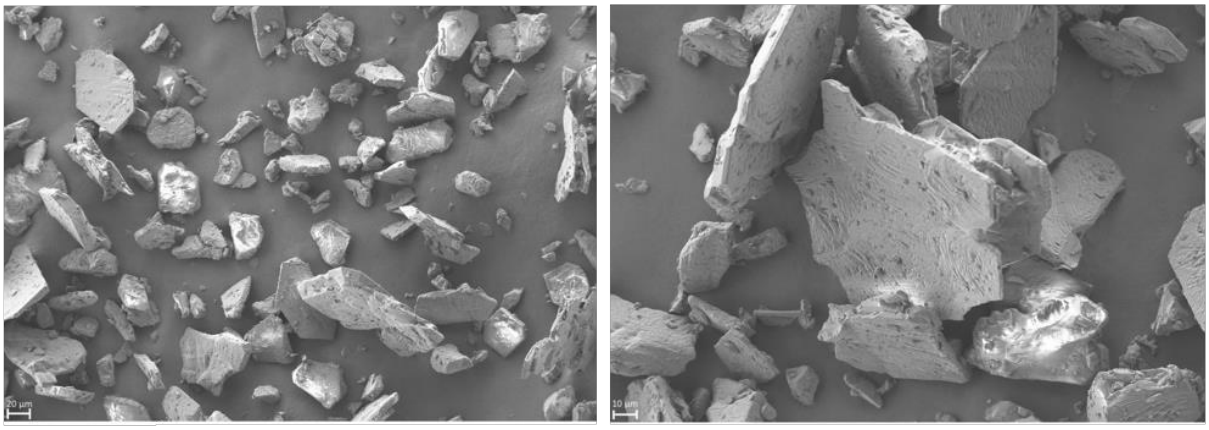

***Figure 11**. SEM pictures of Imq_RM taken at 500X (left) and 1000X magnification (right).*

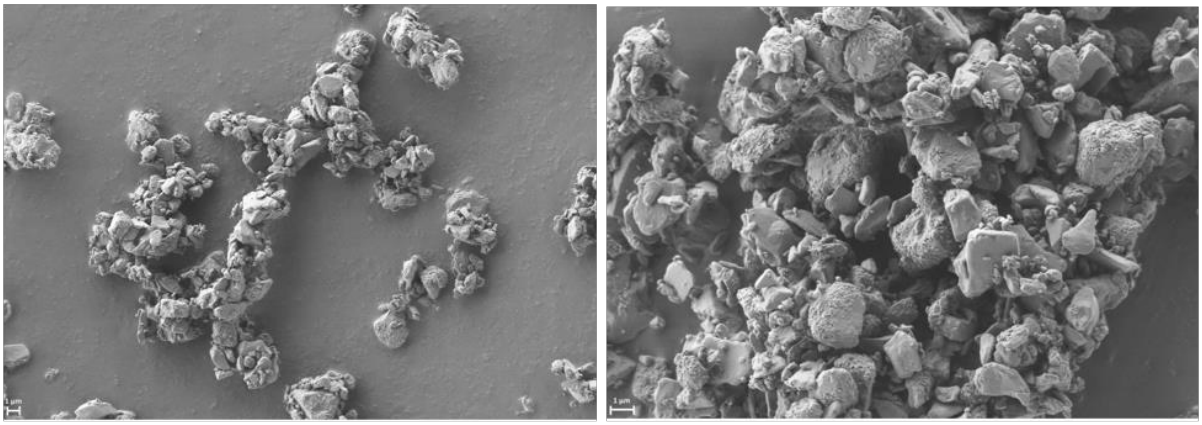

***Figure 12**. SEM pictures of Imq_M taken at 5000X (left) and 10000X (right) magnification.*

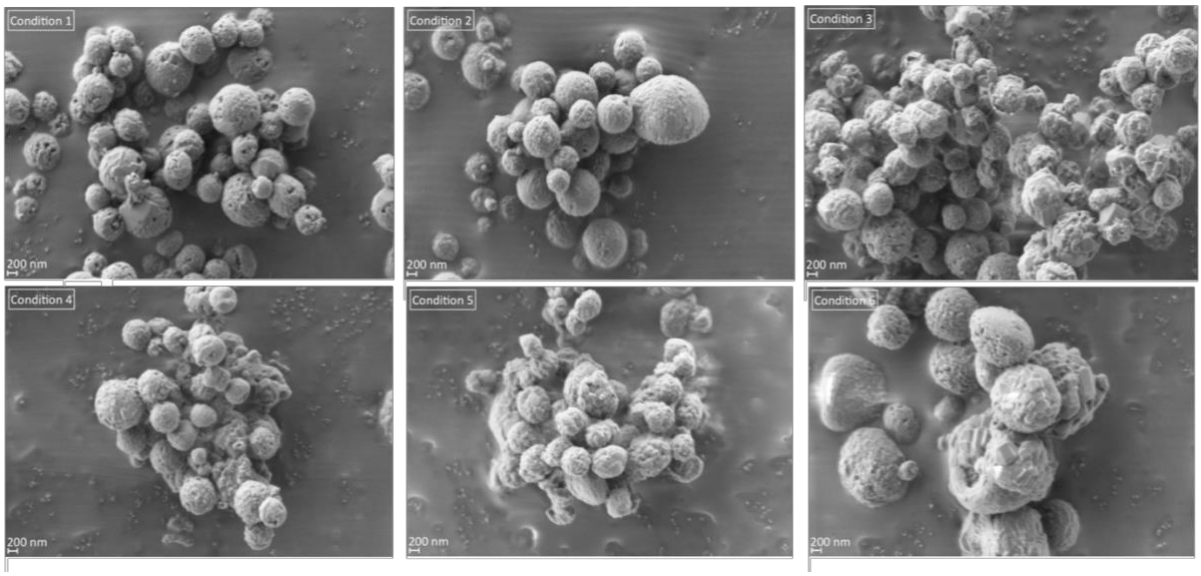

***Figure 13**. SEM pictures of Imq_SD obtained under conditions listed in Table 7 taken at 30000X magnification.*

SEM pictures showed that Imq_RM are composed of irregular particles mainly in the form of scales with dimensions visually around 30 µm. Imq_M comprise particles with sizes around 2

μm and a rough shape, which is reasonable because they were obtained from the micronization of Imq_RM, which occurs thanks to violent collisions between particles inside the micronization chamber. Imq_SD are very different: regardless of conditions, they always had an almost spherical shape, a wrinkled surface, and visually sub-micron dimensions.

Regarding Imq_M and Imq_SD, an estimate as precise as possible on their arithmetic mean diameter was carried out based on their SEM images and with the help of ImageJ software. Results are shown in Table 12.

***Table 12**. The arithmetic mean diameter of Imq_M and Imq_SD obtained under conditions listed in Table 7.*

Sample	Arithmetic mean diameter (μm)
Condition 1	0.82 ± 0.26
Condition 2	0.77 ± 0.25
Condition 3	0.80 ± 0.25
Condition 4	0.73 ± 0.21
Condition 5	0.81 ± 0.24
Condition 6	1.09 ± 0.39
Imq_M	1.97 ± 0.93

These results showed that Imq_SD are tiny, and this is because the spray drying process started from extremely dilute solutions (250 or 375 μg/mL) and, in general, particle size is usually increased as the feed concentration increases [65]. These results also showed that Imq_SD and Imq_M could be potentially suitable for inhalation administration as suggested by dimensions lower than 5 μm. However, further analysis, like laser diffraction and aerodynamic characterization, must be carried out to state it with certainty.

Based on these results, it was also possible to build the cumulative undersize distribution of Imq_M and Imq_SD produced under conditions listed in Table 7 (Figure 14).

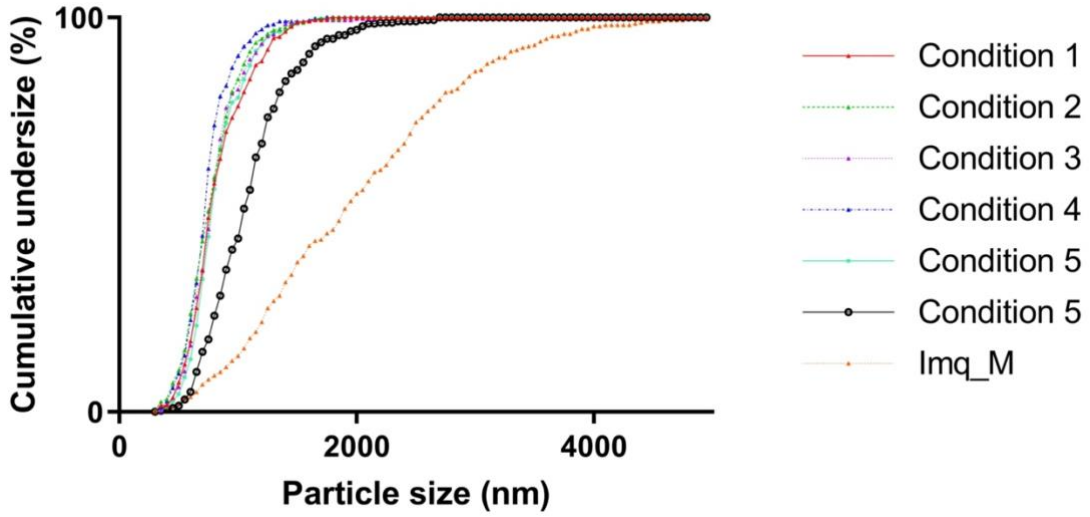

***Figure 14**. Cumulative undersize distribution of Imq_M and Imq_SD produced under conditions listed in Table 7.*

Regarding the spray drying process, the arithmetic mean diameter of Imq_SD obtained under condition 1 is not statistically different from conditions 3 and 5 ($p = 0.33$ and 0.85), as well as for condition 2 compared to conditions 3 and 4 ($p = 0.19$ and 0.049), and for condition 3 compared to condition 5 ($p = 0.40$). A statistically significant difference was found between the conditions 1 and 2 ($p = 0.02$), 1 and 4 ($p < 0.0001$), 2 and 5 ($p = 0.03$), 3 and 4 ($p = 0.001$), 4 and 5 ($p < 0.0001$). Finally, a statistically significant difference was found between condition 6 and all other conditions ($p < 0.0001$). It can be concluded that with conditions from 1 to 5, the samples obtained are relatively similar with an arithmetic mean diameter of 0.7-0.8 µm, although, from some comparisons, statistically significant differences appear. Condition 6 is the one that gave rise to Imq_SD with an arithmetic mean diameter that differs most from the others (~ 1.1 µm), with a difference that appears statistically significant in any comparison. This considerable difference is also visually evident in Figure 14, which shows that distributions are monomodal and narrow, as indicated by their high slope, with 90% of the distribution below 1000-1200 nm, except for condition 6, in which 90% is below 1600 nm. In the case of condition 6, the difference is explained by the fact that a fraction of powder was deposited in the cyclone at the end of the spray drying process. In contrast, the other fraction was deposited in the product collection vessel. The powder deposited in the product collection vessel was wet, so it was discarded, whereas the powder deposited in the cyclone was dry, so it was recovered

and analyzed through SEM. Reasonably, the powder deposited in the cyclone was formed by particles larger than those deposited in the product collection vessel due to their lower momentum.

Micronization produces larger particles than spray drying, as suggested by an almost double arithmetic mean diameter (Table 12) and a visually different cumulative undersize distribution (Figure 14) of Imq_M.

3.4.3 Selection of the best condition for production by spray drying

Imq_SD obtained under conditions listed in Table 7 are very similar, if not the same, in terms of morphology (Figure 13), arithmetic mean diameter (Table 12), and cumulative undersize distribution (Figure 14); this last except condition 6, whose peculiarity is only apparent, as explained in paragraph 3.4.2. Considering the substantial similarity between Imq_SD obtained under all conditions tested, condition 2 was selected as the best method for producing Imq_SD because it led to a higher process yield (Table 11). Moreover, unlike condition 4, which had the same yield, condition 2 had the advantage of employing pure EtOH as a solvent which, being low boiling, allows it to work with a lower inlet temperature. The outlet temperature observed under condition 2 was equal to 50 °C. All the experiments subsequently performed were then conducted employing Imq_SD produced under condition 2.

3.4.4 Laser diffraction

Laser diffraction showed for Imq_RM a Dv50 of 31.6 ± 1.2 μm and a Span of 2.1 ± 0.1, which is in accordance with dimensions observed in SEM images (around 30 μm, as stated in paragraph 3.4.2). Moreover, laser diffraction showed for Imq_M a Dv50 of 2.04 ± 0.16 μm and a Span of 1.66 ± 0.15, and for Imq_SD produced under condition 2 a Dv50 of 1.05 ± 0.2 μm and a Span of 1.85 ± 0.62: once again, Dv50 values are in accordance with arithmetic mean diameters (Table 12), although they are values that come from methods that measure the diameter of the particles in conceptually very different ways. Moreover, Dv50 values obtained

with laser diffraction, like arithmetic mean diameters, suggested once again that spray drying a solution of Imq_RM in EtOH at a concentration of 375 µg/mL or micronize Imq_M appeared to be an appropriate method to produce particles suitable for inhalation and deposition in the deep lung.

3.4.5 Solid-state characterization

PXRD was used to study the solid-state of Imq_RM, Imq_M, and Imq_SD. The relevant diffraction patterns are shown in Figure 15.

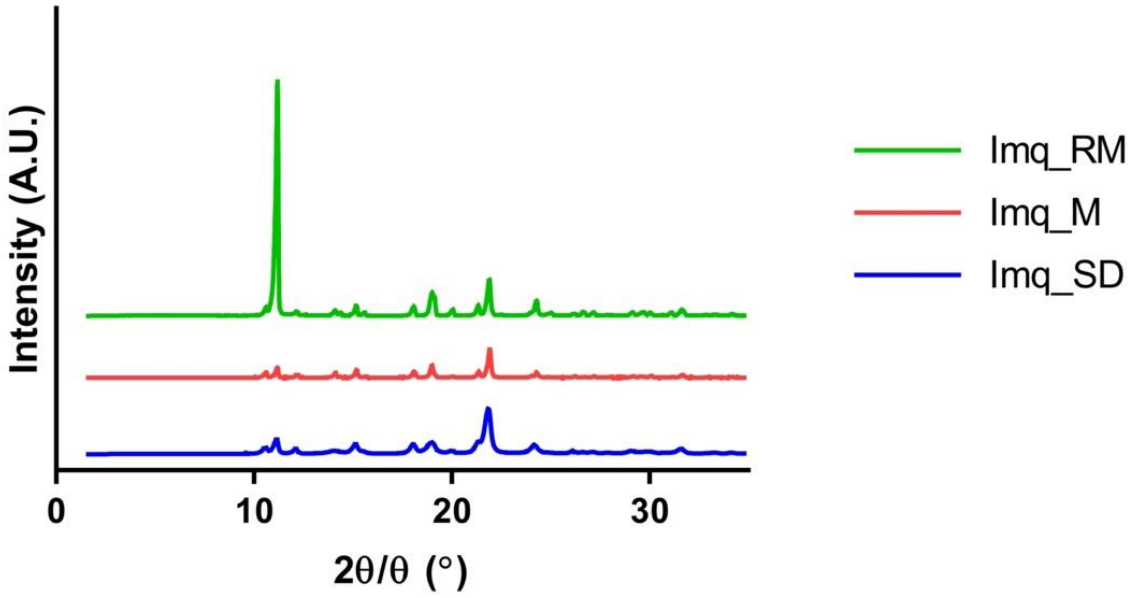

***Figure 15**. X-ray diffraction patterns of Imq_RM, Imq_M, and Imq_SD.*

The diffractograms were very similar, being practically superimposable for peak position. PXRD showed that Imq_RM, even if micronized or dissolved in EtOH and subjected to a spray drying process at 80 °C, did not undergo alterations of the solid-state because Imq_RM, Imq_M, and Imq_SD appear to be composed of the same crystal phase and the formation of polymorphs or amorphous phases upon the spray drying or micronization process can be excluded. Passing from Imq_RM to Imq_SD, a decrease in the degree of crystallinity of 3.89% was found, and of 69.06% passing to Imq_M (Equation 8). However, the obtained values were

not intended to be considered absolute crystallinity values but have been used for comparative purposes [66].

DSC further evaluated the solid-state of Imq_RM, Imq_M, and Imq_SD. DSC traces (Figure 16) of Imq_RM, Imq_M, and Imq_SD showed a single endothermic peak due to the melting of the drug crystal lattice at the onset temperature of 297 ± 1 °C, which is the temperature at which 10% of the solid melts. The peak temperature, which is the temperature at which 100% of the solid melts, was 298 ± 1 °C for Imq_RM, 297 ± 0 °C for Imq_M, and 298 ± 1 °C for Imq_SD. No other thermal phenomena were registered. In summary, the DSC traces of Imq_RM, Imq_M, and Imq_SD were superimposable. Finally, DSC analysis showed that the enthalpy of fusion was 240 ± 4 J/g for Imq_RM, 256 ± 3 J/g for Imq_M, and 248 ± 6 J/g for Imq_SD, three values that are not statistically different ($p = 0.08$) thus confirming, that from the point of view of the degree of crystallinity, the three powders are substantially superimposable.

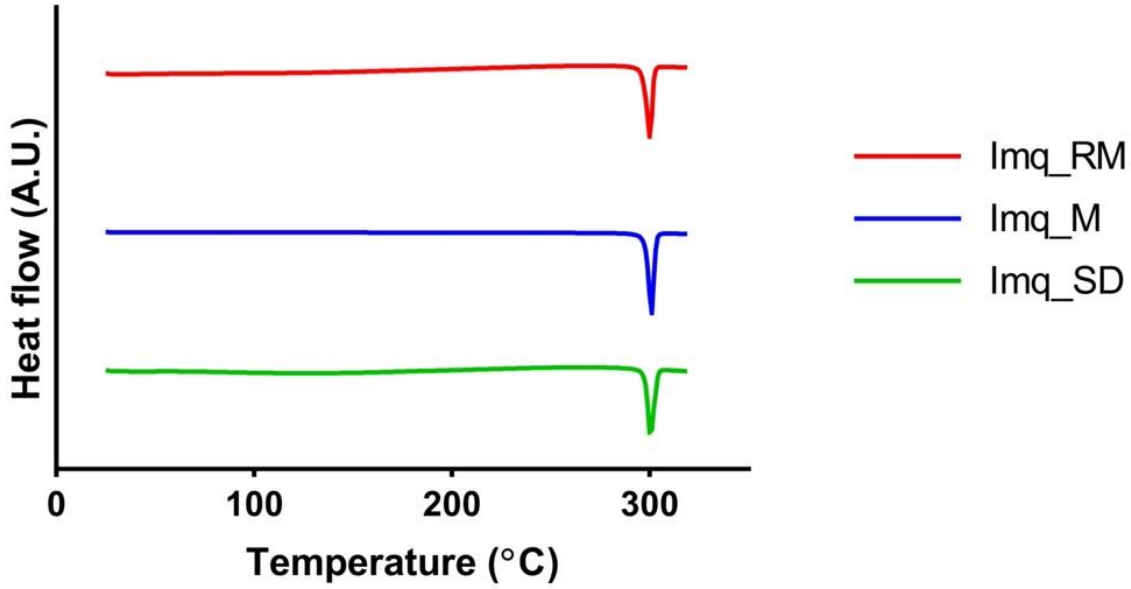

***Figure 16**. DSC traces of Imq_RM, Imq_M, and Imq_SD.*

The formation of molecular aggregates between IMQ molecules in solution in highly polar solvents highlighted from results presented in paragraph 2.5.4 is reasonably the phenomenon that forms the foundation for IMQ's tendency to yield crystalline powders after the spray drying procedure, as evidenced above. In this sense, aggregates formed in the feed solution likely

act like catalysts for the nucleation process preparatory to crystal formation. In contrast, other active substances frequently lead to the formation of amorphous powders.

In addition to the solid-state characterization, the purity of Imq_SD was assessed with HPLC with a method previously ensured to be stability-indicating (paragraph 2.3.2.2). Imq_SD were considered pure because actual concentrations found with HPLC analysis were between 95 and 105% of those expected.

3.4.6 In vitro aerosol performance

An estimate of the hypothetical therapeutic dosage of IMQ administered by inhalation was made based on the study of To et al., in which 50 µg of IMQ were administered to mice intranasally daily [40]. Considering that a laboratory mouse has an average weight of 70 g, the dosage for the animal was about 0.7 mg/kg. The corresponding human dosage was then calculated with Equation 9:

$$\text{Human dosage} = \frac{\text{mouse dosage} \cdot k_m \text{ mouse}}{k_m \text{ human}} \qquad \textit{Equation 9}$$

Where k_m is the ratio between body weight (kg) and body surface area (m^2), and corresponds to 3 for the mouse and 37 for the human [67]. Human dosage was, then, about 0.06 mg/kg. Considering that a human has an average weight of 70 kg, the hypothetical therapeutic dosage of IMQ inhaled in humans was ~ 4.2 mg. Another estimate was made based on the study of Salinas et al., in which 5 mg/kg of IMQ was administered to mice intranasally daily [41]. In this case, applying the same reasoning, the corresponding human dosage is about 0.4 mg/kg, and the hypothetical therapeutic dosage of IMQ administered by inhalation in humans was around 28 mg. However, it is essential to point out that these estimates are preliminary and approximate, that these studies referred to the intranasal administration and not to the inhalation one, and that it is not excluded that in future studies these dosages will prove to be too high and that it will be necessary to lower them. In general, we do not have specific data on the dosage that has to be administered to humans by inhalation, and one of the aims of this

second chapter is to study powders suitable to precisely investigate this aspect, so it was essential to build powders which covered a wide range of possible dosages. For this reason, we decided to mix IMQ with a carrier to obtain very low dosages that could not be otherwise handled, i.e., accurately dosed in a capsule. In this regard, adhesive mixtures of Imq_M and Imq_SD in lactose LH100, namely Imq_SD1L, Imq_SD5L, Imq_M1L, and Imq_M5L, were prepared, and 20 mg of them were aerosolized. At the end of the manual mixing procedure, Imq_SD1L, Imq_SD5L, Imq_M1L, and Imq_M5L were checked in terms of homogeneity, and they were assumed to be homogeneous because CV was, respectively, 0.40%, 1.79%, 1.26%, and 3.93%; in any case, values lower than 5%. In summary, having aerosolized 20 and 5 mg of Imq_M or Imq_SD alone and 20 mg of adhesive mixtures Imq_SD5L, Imq_SD1L, Imq_M1L, and Imq_M5L, we can say that we have explored a range of dosages from 0.2 to 20 mg of the active ingredient. The percentage distribution of the drug resulting from the ACI test for each powder is illustrated in Figure 17.

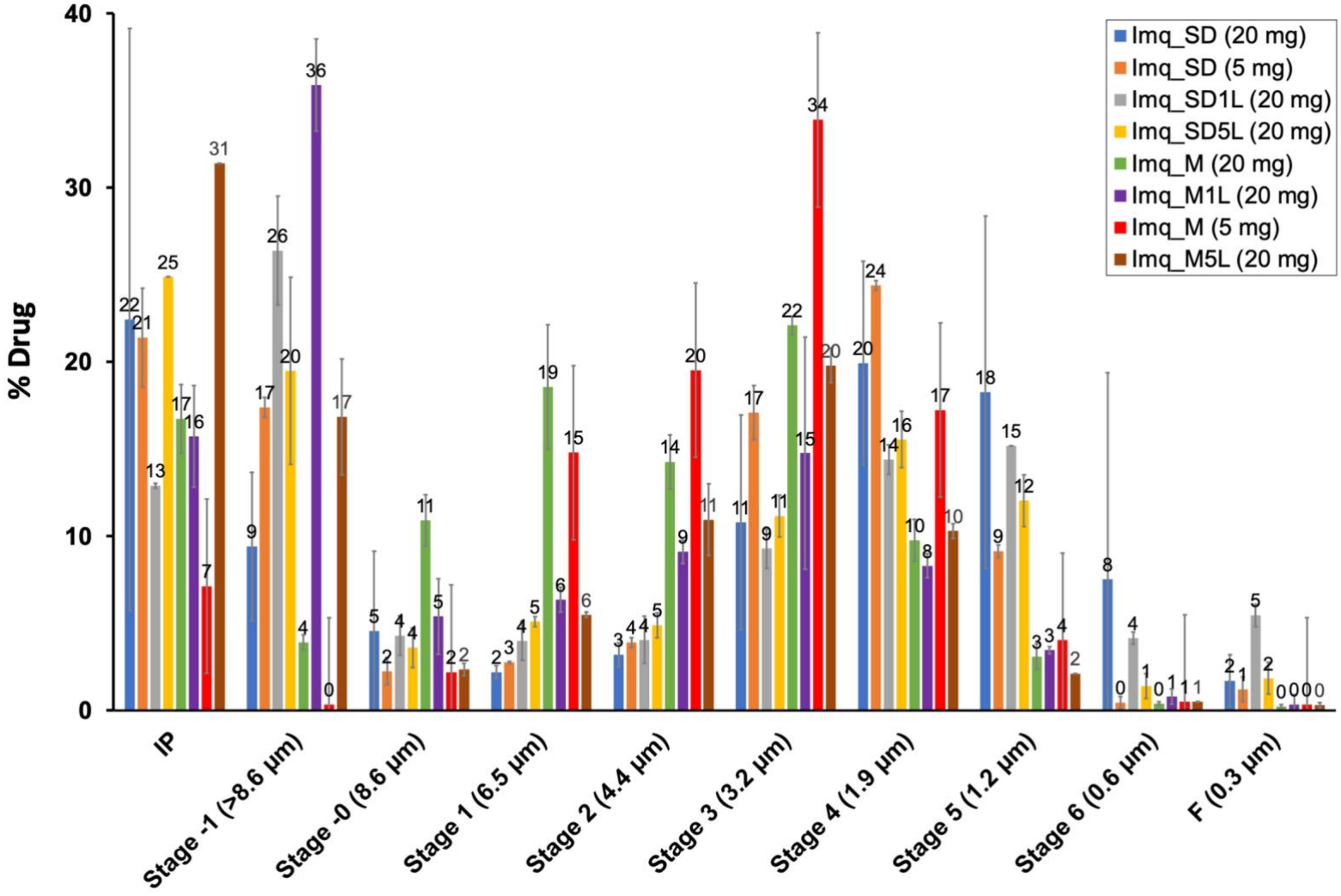

***Figure 17**. Percentage distribution of drug resulted from the ACI test for each powder.*

Imq_SD and their adhesive mixtures, Imq_SD1L and Imq_SD5L, slightly differ regarding the percentage of drug deposited in IP and stage -1: for Imq_SD the percentage of drug remaining in upper sections of the ACI is about 32-39%, while for adhesive mixtures this percentage is approximately 39-44%. Considering the lower stages of the ACI, the aerosolization of Imq_SD, Imq_SD1L, and Imq_SD5L resulted in the deposition of the drug mainly in stages 3, 4, and 5. Table 13 summarizes the aerodynamic parameters of Imq_SD, Imq_SD1L, and Imq_SD5L.

***Table 13**. MMAD, ED, DD, FPD, and FPF obtained upon aerosolization of spray-dried IMQ powders.*

Powder	MMAD (μm)	ED (%)	DD (mg)	FPD (mg)	FPF (%)
Imq_SD (20 mg)	1.65 ± 0.58	59.43 ± 8.53	8.51 ± 2.02	5.61 ± 0.71	68.14 ± 15.86
Imq_SD (5 mg)	2.13 ± 0.11	62.01 ± 10.55	2.59 ± 0.02	1.69 ± 0.07	65.22 ± 3.07
Imq_SD1L (20*4 mg)	2.46 ± 0.16	98.81 ± 0.25	0.54 ± 0.06	0.32 ± 0.03	59.10 ± 0.15
Imq_SD5L (20*3 mg)	2.75 ± 0.79	87.79 ± 1.43	1.40 ± 0.17	0.76 ± 0.02	54.35 ± 4.95

Regarding Imq_SD aerosolized alone, the dose loaded in the capsule, 20 or 5 mg, does not influence the de-aggregation because FPF and MMAD are not statistically different ($p > 0.05$). FPF values suggest that Imq_SD have good de-aggregation and flow properties despite the absence of diluents or lubricants. Regarding Imq_SD1L and Imq_SD5L, compared to Imq_SD alone, ED increases from 59-62% to 88-99%, and this difference is statistically significant ($p < 0.05$): almost all the powder loaded in the capsule is emitted. Moreover, probably because a part of the drug does not separate from the carrier during aerosolization, MMAD increases significantly compared to Imq_SD. Consequently, FPF is reduced, suggesting that among Imq_SD adhesive forces are more significant than cohesive forces, although these differences are not statistically significant ($p > 0.05$). In conclusion, ACI tests showed that Imq_SD have good de-aggregation properties even when administered without excipients, which is advantageous as it allows the administration without requiring the development of complex formulations. However, aerodynamic parameters are promising even in the case of adhesive mixtures.

Theoretical MMAD of Imq_SD can be calculated with Equation 6, where MMAD is D_{ae}. We can first estimate by approximating ρ_p, the density of Imq_SD, to the skeletal density of IMQ, which

was assessed with a gas pycnometer equal to 1.257 ± 0.001 g/cm^3. Similarly, we can approximate the shape of Imq_SD to those of a sphere, so χ equal to 1. It is essential to underline that these are estimates because the density of Imq_SD is not exactly equal to the skeletal density of IMQ, as suggested, for example, by the corrugated surface visible from SEM pictures. For the same reason, it is evident that Imq_SD are not perfect spheres. However, with these values, theoretical MMAD for Imq_SD alone is equal to 1.18 μm, which is slightly lower than experimental MMAD values, which are 1.65 μm and 2.13 μm for the high and low dosage, respectively, with a difference not statistically significant in both cases ($p = 0.56$ and 0.09, respectively). These minor discrepancies between theoretical and experimental values can be explained by the approximations made at the beginning. Finally, as suggested by the experimental MMAD higher than Dv50, Imq_SD likely have a particle density greater than 1, which reasonably reduces its ability to float in the airstream. A second element that could explain the difference is the large surface area of Imq_SD, which could give rise to aggregates between small particles that, eventually, act like larger ones. However, despite their probably high density and large surface area due to their small size and wrinkled surface, we can conclude that Imq_SD are mostly respirable, as suggested by FPF.

Moving to the micronized powders (Figure 17), Imq_M and their adhesive mixtures, Imq_M1L and Imq_M5L, differ significantly regarding the percentage of drug deposited in IP and stage -1: for Imq_M the percentage of drug remaining in upper sections of the ACI is about 8-21%, while for adhesive mixtures this percentage is higher, namely about 48-52%. In the lower stages of the ACI aerosolization of Imq_M resulted in the deposition of the drug mainly in stages 1, 2, and 3. In contrast, aerosolization of Imq_M1L and Imq_M5L resulted in the deposition of the drug mainly in stages 2, 3, and 4. Table 14 summarizes the aerodynamic parameters of Imq_M, Imq_M1L, and Imq_M5L.

***Table 14**. MMAD, ED, DD, FPD, and FPF obtained upon aerosolization of micronized IMQ powders.*

Powder	MMAD (μm)	ED (%)	DD (mg)	FPD (mg)	FPF (%)
Imq_M (20 mg)	3.64 ± 0.13	63.76 ± 3.17	13.30 ± 1.20	7.25 ± 1.07	53.34 ± 3.49
Imq_M (5 mg)	2.81 ± 0.30	90.91 ± 15.06	3.44 ± 0.55	2.71 ± 0.74	78.00 ± 8.68
Imq_M1L (20*4 mg)	6.23 ± 1.33	97.56 ± 2.38	0.35 ± 0.02	0.16 ± 0.02	43.34 ± 7.59
Imq_M5L (20*3 mg)	3.35 ± 0.13	96.45 ± 3.04	1.71 ± 0.10	0.81 ± 0.08	47.43 ± 2.33

Regarding Imq_M alone, the dose loaded in the capsule, 20 or 5 mg, influences both MMAD and FPF, so the de-aggregation, because a statistically significant difference ($p < 0.05$) is observed in both cases. In particular, the aerosolization of 20 mg of Imq_M led to a higher MMAD and a lower FPF than the aerosolization of 5 mg. For the aerosolization of 5 mg of Imq_M, we can say that the powder has good de-aggregation and flow properties, as suggested by a FPF of 78.00 ± 8.68, but for the aerosolization of 20 mg of Imq_M FPF value, 53.34 ± 3.49, is too low to state that. Comparing Imq_M alone with their adhesive mixtures, ED increases from 64-91% for Imq_M alone to 97-98% for adhesive mixtures, and this difference is statistically significant ($p < 0.05$): for adhesive mixtures, almost all the powder loaded in the capsule is emitted. Moreover, from this comparison, it also emerges that FPF decreases from 53-78% to 43-47%, while MMAD increases. In this respect, for Imq_M1L, MMAD equals 6.23 ± 1.33, a very high value. In conclusion, ACI tests showed that Imq_M have suboptimal, yet suitable aerodynamic parameters, especially if administered without lactose.

3.4.7 IMQ solubility in medium

IMQ solubility in the medium at 37 °C resulted equal to 7.6 ± 0.1 μg/ml.

3.4.8 Cell viability analysis

Regarding condition B, it was decided to dissolve IMQ in DMSO as it is, to date, the only solvent in which IMQ has a sufficiently high solubility, i.e., about 1 mg/ml (Table 3), which allows obtaining a solution with a concentration high enough to be diluted with the medium and

put in contact with cells. It follows that the obtained 5 µg/ml solution of IMQ in the medium also contained DMSO at a concentration of 0.5% v/v, which, however, from preliminary studies, was found not to affect cell viability (data not shown). This scientific evidence is also reinforced by a study in which it was found that a ≤ 5% v/v concentration of DMSO may be used for in vitro studies with Calu-3 cells without significant alteration of cell viability [68]. However, as a precaution, to keep the final concentration of DMSO as low as possible, it was decided not to test solutions with concentrations higher than 5 µg/ml. It was also agreed to adopt this precaution because IMQ in solution was taken only for comparison with IMQ in suspension. A single concentration was considered sufficient for this purpose.

Graphs representing cell viability after 24 h of exposure to Imq_RM or Imq_SD are reported in Figure 18.

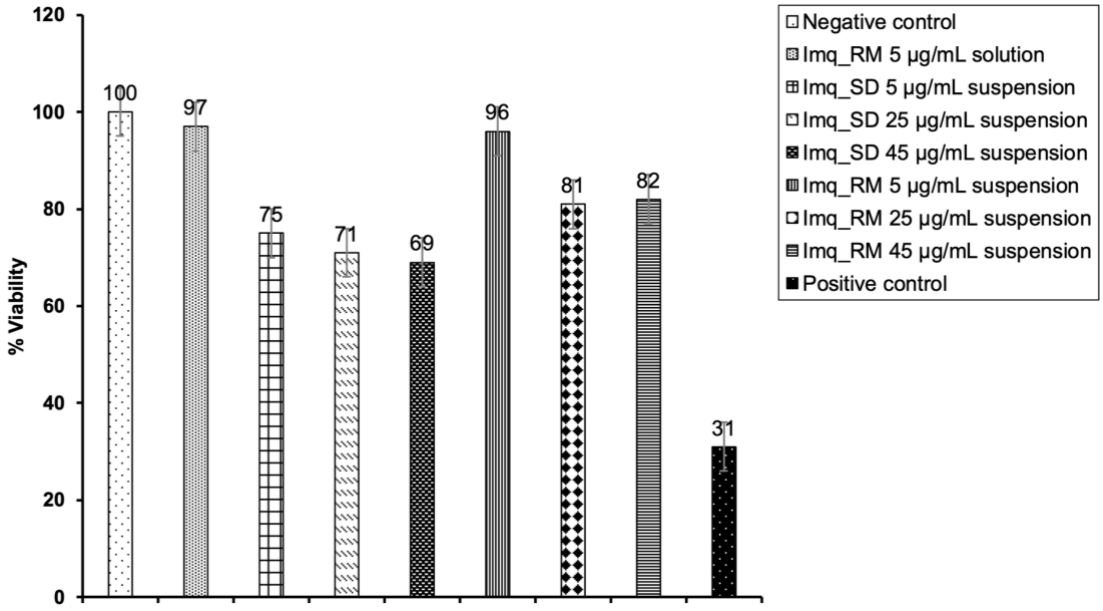

***Figure 18**. Viability of Calu-3 cells exposed to treatments listed in Table 10, as estimated by the MTT assay after 24 h of incubation. Data are expressed as a percentage of the negative control.*

Imq_RM 5 µg/ml solution did not affect cell viability (97 ± 4 %). A statistically significant effect on cell viability of Imq_SD suspensions with respect to the negative control was highlighted, with $p < 0.0001$ in all cases. Almost no cytotoxicity was highlighted for Imq_RM suspension at the lower concentration ($p > 0.05$), whereas the other two suspensions gave rise to a statistically significant difference ($p < 0.0001$).

The cytotoxicity of the Imq_RM 5 µg/ml solution and Imq_RM 5 µg/ml suspension were identical (97 ± 4 and 96 ± 6 %), while with Imq_SD suspension at the same concentration a viability reduction was observed (75 ± 4 %, $p < 0.0001$). This can be explained by considering that Imq_SD 5 µg/ml suspension was constituted by particles of significantly lower diameter than Imq_RM (1.05 *vs* 31.6 µm), which resulted in a tenfold higher surface area (SSA 7.582 ± 2.259 and 0.7084 ± 0.0577, respectively). Such difference in dimension favored the dissolution process, leading to a concentration of the drug at the particle/cell interface close, or equal to, IMQ solubility in the medium (7.6 ± 0.1 µg/ml). Likely, this did not occur with Imq_RM suspension, which requires a long time for reaching the equilibrium solubility [69].

Thus, it was possible to state that Imq_RM suspension, as well as the solution, were non-toxic, while the spray-dried particles exerted a limited effect on cell viability with values slightly above or equal to the standard threshold of acceptability (70%) [70].

3.4.9 IL-6 and IL-8 immunoassays

The Calu-3 lung cell line is a promising *in vitro* model of airway epithelia due to its similarity to *in vivo* physiology [71], while IL-6 and IL-8 are among the most important inflammatory cytokines elicited by innate immunity, and so they were selected to test *in vitro* IMQ innate immunity stimulation effect. IL-6, rapidly and temporarily synthesized in reaction to infections and tissue injuries, is pivotal in bolstering the body's defense mechanisms by triggering acute phase responses, promoting hematopoiesis, and enhancing immune reactions [72], while IL-8 is a pro-inflammatory chemokine generated in response to inflammatory conditions by various immune and non-immune cell types which primary role is the recruitment of neutrophils to the inflammatory site [73]. The levels of IL-6 after 24 h exposure to conditions listed in Table 10 were determined by ELISA and are depicted in Figure 19.

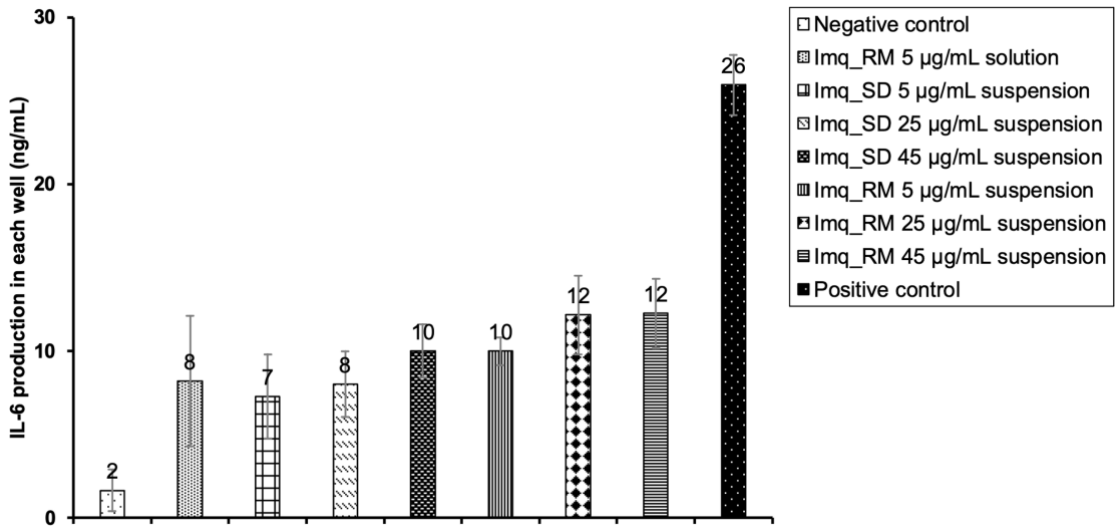

***Figure 19**. In vitro stimulation of IL-6 production by Calu-3 cells exposed to treatments listed in Table 10 after 24 h of incubation.*

Imq_RM 45 µg/mL suspension led to the production of 12 ± 2 ng/mL, positioning as the condition that stimulated the maximum production of IL-6. At an IMQ level of 5 µg/mL, considering both solution and suspensions, Imq_RM had a more significant stimulating effect than Imq_SD (10 ± 1 compared to 7 ± 3 ng/mL), while Imq_SD had substantially the same stimulating effect as IMQ in solution (7 ± 3 compared to 8 ± 4 ng/mL), an effect that can be ascribed to the fact that larger particles can induce a greater IL-6 production compared to smaller particles. In general, however, considering that the negative control led to an IL-6 concentration of 2 + 1 ng/mL, while IMQ, both in solution and suspensions, led to concentrations from 7 + 3 to 12 + 2 ng/mL, it can be concluded that IMQ stimulated IL-6 production *in vitro*. Moreover, it can be considered a controlled stimulation because it is higher than the negative control, but not as high as the positive control (26 + 2 ng/mL), which is desirable because excessive stimulation, such as that induced by LPS, can be dangerous.

In this regard, Tan et al. demonstrated that the TLR-2 agonist Pam2Cys administered intranasally induced secretion of cytokines, including IL-6, that, along with other changes, provided increased resistance against influenza A virus challenge, decreased the transmissibility of the infection and reduced weight loss and lethality associated with virulent influenza virus infection in a TLR-2-dependent manner. More specifically, the concentration of IL-6 found in the bronchoalveolar lavage fluid of mice 72 h after the administration of the TLR-

2 agonist was about 1.25 ng/mL, a concentration close to those obtained in our study and, therefore, encouraging [74].

The levels of IL-8 after 24 h exposure to conditions listed in Table 10 were determined by ELISA and are depicted in Figure 20.

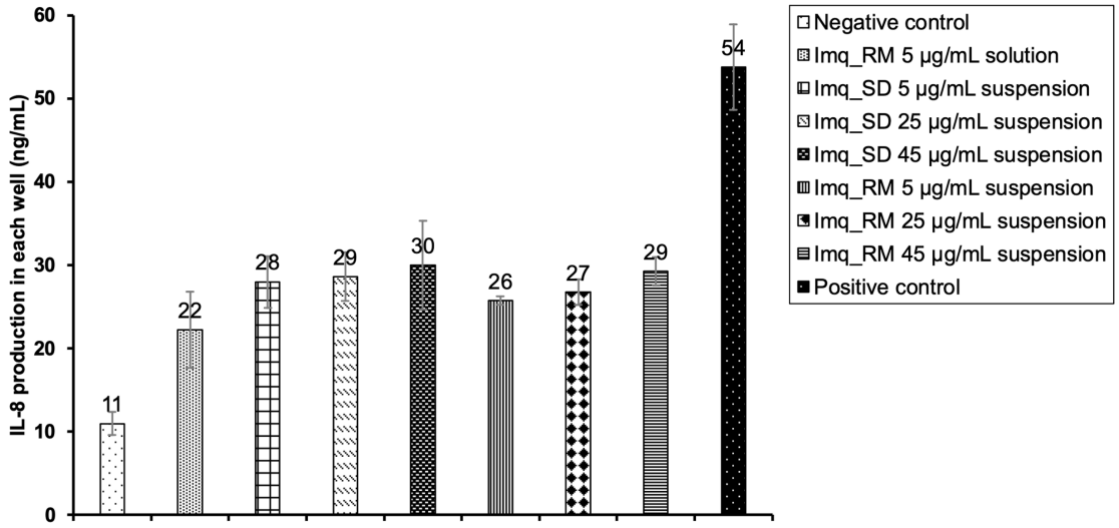

***Figure 20**. In vitro stimulation of IL-8 production by Calu-3 cells exposed to treatments listed in Table 10 after 24 h of incubation.*

Similarly to IL-6, at an IMQ level of 5 µg/mL, considering both solution and suspensions, Imq_RM and Imq_SD had a more significant stimulating effect than IMQ in solution (26 ± 1 and 28 ± 3 compared to 22 ± 5). Moreover, considering that the negative control led to an IL-8 concentration of 11 + 1 ng/mL, while IMQ, both in solution and suspensions, led to concentrations from 22 + 5 to 30 + 5 ng/mL, it can be concluded that IMQ stimulated IL-8 production *in vitro*, and as for IL-6, also IL-8 production can be considered controlled, being considerably lower than that induced by the positive control (54 + 5 ng/mL).

3.5 Conclusions

The second chapter of this thesis focused on the development of an imiquimod powder for pulmonary administration. In this respect, a dry powder for inhalation was designed, produced, and characterized. Both micronization and spray drying were found to be suitable methods to produce highly crystalline and respirable IMQ particles, with a yield of more than double in the

case of micronization compared to spray drying. The actual suitability for administration and deposition in the deep lung was suggested by the measurement of the geometric diameters and confirmed by *in vitro* aerodynamic assessment that showed an MMAD much lower than 5 µm. If future pre-clinical or clinical studies demonstrate the need to lower the administered dose, the formulation of these particles in adhesive mixtures in a carrier may be a suitable strategy. In the present study, adhesive mixtures with coarse lactose proved to maintain a favorable aerodynamic behavior, affording an acceptable respirability.

Finally, *in vitro* studies suggested micronized and spray-dried particles' non-toxicity and ability to induce controlled production of inflammatory cytokines, such as IL-6 and IL-8.

The proposal to administer imiquimod by inhalation, considering that the use of this molecule is currently limited to the topical route, represents an innovative and highly promising strategy to obtain broad-spectrum, short-term protection against infectious diseases, but also in their fighting, as adjuvant in allergen immunotherapy or in vaccines for pulmonary or nasal administration. This innovative approach is well founded as it is corroborated by encouraging scientific results reported in the literature and the preliminary results obtained in the *in vitro* studies conducted on cell lines in this thesis. In this regard, this work has developed a technological approach, the first in this sense to the best of our knowledge, that allows obtaining an imiquimod inhalation powder with suitable technological properties (de-aggregation and respirability) that could be useful in future studies aimed at investigating the promising off-label uses discussed so far.

4 CHAPTER III: PULMONARY DELIVERY OF PYRAZINOIC ACID NANOCONJUGATES FOR THE TREATMENT OF TUBERCULOSIS

The research that led to the writing of this third chapter was done at Institut Galien Paris-Saclay – UMR CNRS 8612 under the supervision of Professor Elias Fattal, Professor Nicolas Tsapis, and Professor Laurence Moine in collaboration with Dr. Thi Hong Van Nguyen.

4.1 Introduction

4.1.1 Epidemiology of tuberculosis

Tuberculosis (TB) is one of the principal causes of death worldwide. Before the COVID-19 pandemic, TB was the leading cause of death from a single infectious agent, over HIV/AIDS. The COVID-19 pandemic strongly impacted the possibility of diagnosing and treating TB. In this regard, a reduction of 18% in the number of people newly diagnosed with TB has been observed from 2019 (7.1 million) to 2020 (5.8 million), with a partial recovery registered in 2021 (6.4 million) [75].

The impact of the COVID-19 pandemic on TB diagnosis led to a high number of people with undiagnosed and untreated TB, with a consequent increase in deaths from TB and TB transmission, with increased numbers of people developing TB soon [75].

The estimated number of deaths from TB had been declining since 2005, but in 2019 it began to rise. According to WHO, 1.4 million HIV-negative people and 187000 HIV-positive people died of TB in 2021, for a total of 1.6 million people. This number exceeds 2020 (1.5 million) and 2019 (1.4 million). Most of the estimated increase in TB deaths regarded India, Indonesia, Myanmar, and the Philippines [75].

It is estimated that 10.6 million people developed TB worldwide in 2021, with a growth of 4.5% compared to 2020 (10.1 million), reversing the downward trend that has been going on for

many years. The same was shown for the TB incidence rate, which grew by 3.6% between 2020 and 2021 [75].

Another big concern is the worsening of drug-resistant TB, which requires treatment with second-line drugs because the estimated number of people who developed it worldwide each year was relatively stable from 2015 to 2020 and began to rise in 2021, reasonably due to the increase in TB incidence rate described above between 2020 and 2021 [75]. New approaches to fight TB, therefore, remain an urgent need.

4.1.2 Pathogenesis of tuberculosis

TB is caused by *Mycobacterium tuberculosis* (Mtb) and related species of the so-called Mtb complex [76]. In 80% of cases, TB affects the lungs, leading to pulmonary TB. Still, it can also affect other tissues (intestine, meninges, lymph nodes, bones, joints, kidneys, and skin), leading to extra-pulmonary TB [77].

The pathogenesis of TB is depicted in Figure 21 [76] and starts with the inhalation of infectious droplet nuclei, which are particles of 1–5 μm containing Mtb expectorated by patients with active pulmonary TB, for example, when the patient coughs [78]. After inhalation, droplet nuclei with Mtb penetrate the terminal alveoli and are phagocytosed by phagocytic immune cells, mainly alveolar macrophages, where Mtb starts to replicate [76,79]. Alveolar macrophages protect the host from the invasion by Mtb, but also facilitate its proliferation, establishing a niche that saves the pathogen from elimination by immune systems, with the possibility of allowing the infection to remain persistently in a latent stage. Alveolar macrophages may also be transported across the alveolar barrier to cause systemic dissemination. The intracellular replication of the pathogen and its simultaneous dissemination to both pulmonary and non-pulmonary sites via lymphatics and blood circulation begin before the adaptive immune response [76,78], which starts to develop right after the spreading of Mtb inside lymph nodes. Dendritic and $CD4^+$ T cell interaction activates adaptive immunity, while macrophages elicit innate and adaptive immunity [76,80]. In most cases, 2-8 weeks after infection, further

multiplication of pathogens is permanently blocked by an effective cell-mediated immunity, and disease progression is arrested [76,78].

In some cases, the mycobacteria growth is arrested, but some bacilli persist and stay dormant for many years, in a state known as latent TB infection [76]. If the bacterial replication is not arrested, Mtb can be released in the extracellular environment, where it can replicate, release toxic lipids and proteins, and interact with host cells [76,81]. Elicitation of adaptive immunity and activation of macrophages lead to phagosome-lysosome fusion and the production of cytokines that can both consolidate the bactericidal response and potentially damage tissues due to significant lung inflammation [76]. Active TB, which may come from reinfection with Mtb or reactivation from a latent infection, is characterized by replication of Mtb and an excessive host inflammatory response that damages the host's tissues, leading to lesion necrosis and cavitation [76,82].

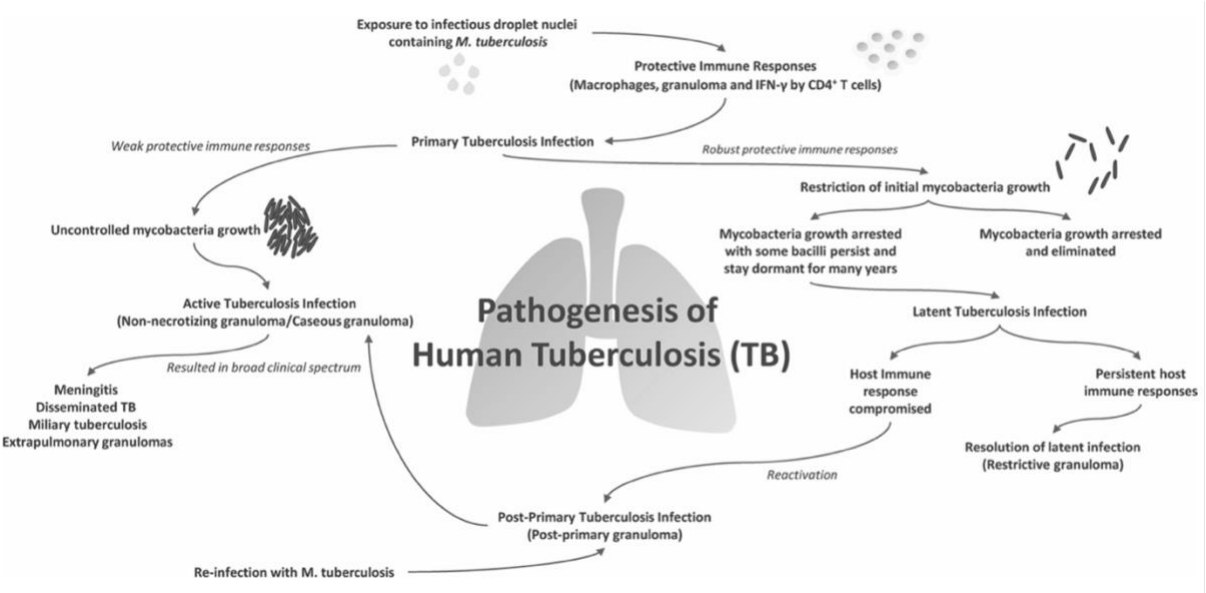

***Figure 21**. Pathogenesis of human TB* [76].

Pulmonary TB in humans is characterized by the formation of tuberculous granulomas shortly after the infection [76]. Granulomas, depicted in Figure 22 [83], exist in different forms, depending on the infectious state. The classic tuberculous granuloma, found in active and latent TB, is the caseous granuloma, which is composed of epithelial macrophages, neutrophils, an external layer of B and T cells ($CD4^+$ and $CD8^+$), and sometimes a fibrosis outer

layer. Its center is necrotic and hypoxic. In caseous granuloma, it is possible to find Mtb in macrophages, the hypoxic center, or the fibrotic border. The non-necrotic granuloma involved in active TB comprises mainly macrophages and some lymphocytes and can harbor Mtb only within macrophages. Fibrotic (or restrictive) granulomas are involved primarily in latent, sometimes also active TB, and comprise mainly fibroblasts; it is unclear where the pathogen is harbored [76,83]. Increased necrotic breakdown of granulomas and expansion of lesions in active TB damage vascular and bronchial walls, with consequent caseous necrosis and granuloma cavitation which, if it occurs in the lungs, allows the spreading of Mtb within the air and, therefore, disease transmission [76]. Granulomas aim to isolate the pathogen, preventing its dissemination and tissue damage due to bacterial replication and necrosis [84]. However, not all granulomas are sterilized, possibly promoting the persistence of Mtb in a dormant state, which can replicate and disseminate in immunocompromised populations [76,83]. Moreover, necrotic granulomas are associated with the subpopulation of Mtb that persist during host immune responses or drug treatment [85,86]. Finally, the heterogeneity of granulomas makes TB more challenging to treat since conventional oral or parenterally delivered therapies are inefficient in providing therapeutic levels of drugs inside granulomas and making the distribution variable among lesions [86].

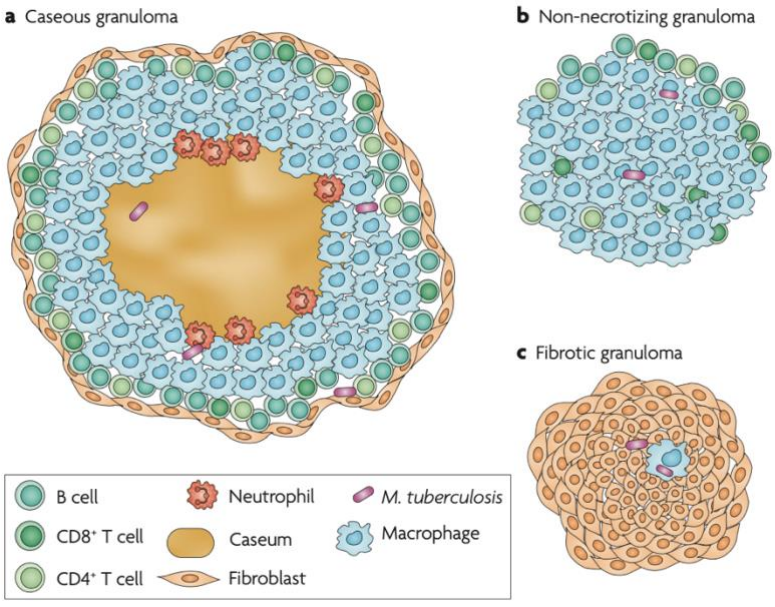

***Figure 22**. Tuberculous granulomas* [83].

4.1.3 Diagnosis of tuberculosis

Regarding the clinical diagnosis, it is essential to point out that only 5-10% of affected individuals present symptoms. However, pulmonary TB is usually characterized by symptoms in the lower respiratory system, like chronic productive cough, hemoptysis, low-grade fever, night sweats, loss of appetite, malaise, fatigue, and weight loss. In contrast, symptoms of extra-pulmonary TB depend on the site affected.

Chest X-rays are a screening tool [87] used to distinguish between primary and secondary TB but do not provide any etiological diagnosis and cannot detect latent TB [77].

The most common methods for diagnosing latent TB are tuberculin skin test and interferon-γ release assay, two immune-based approaches. However, they cannot distinguish between latent and active TB perfectly, have low sensitivity in some immunocompromised patients, and cannot always predict the progression from infection to active TB [88,89]. Therefore, it is essential to test only people at risk of progression and use all clinical data in addition to test results [88].

Mtb releases many substances when it replicates in the human host, and one of these, namely lipoarabinomannan (LAM), forms the basis of the urinary LAM test. Although it was initially questioned regarding its sensitivity, it is a highly cost-effective and easy test to do, which can be administered at the point of care and makes use of an easily obtained specimen, which showed clear mortality benefits when used in hospitalized HIV-positive people with a CD4 count lower than 200 cells/μL. Thus, the existing urinary LAM test is currently recommended for all seriously ill, hospitalized patients with HIV and a CD4 count lower than 100 cells/ μL. At the same time, higher sensitivity versions have been developed and appear promising even among people without HIV [88].

Molecular testing is used to check simultaneously the presence of Mtb and drug resistance. In this regard, the Xpert MTB/RIF test (Cepheid, CA, USA) is a WHO-recommended rapid nucleic acid amplification test widely employed to detect genetic material from Mtb and mutations

responsible for the resistance to rifampicin in sputum. A more sensitive assay version, Xpert MTB/RIF Ultra, has been developed and endorsed by WHO and is being used in South Africa. However, despite its high sensitivity, it has a low specificity and consequent problems related to the so-called trace-positive results [88,90].

Other genotypic tests based on nucleic acid amplification commercially available for centralized laboratories are RealTime MTB (Abbott, IL, USA), FluoroType MTBDR (Hain Lifescience, Nehren, Germany), and BD MAX MDR-TB (Beckton, Dickinson and Company, NJ, USA). The chip-based Truenat MTB (Molbio Diagnostics, Goa, India) is proposed in microscopy centers [88,91]. Line probe assays, which can detect drug resistance to isoniazid, rifampicin, injectable agents, and fluoroquinolones, are also available but require additional laboratory capacity [88,92].

The sequencing of the whole Genome is gaining more and more importance in identifying drug resistance [88,93] and will probably become the preferred method for that aim [88].

4.1.4 Classical tuberculosis treatment and its limitations

Without treatment, the death rate of TB is around 50%, while it is estimated that with treatment, about 85% of people can be cured [75]. More studies are being done on TB treatment than ever on any other disease, so TB treatment is constantly evolving [88]. The current recommended treatment for pan-susceptible TB involves the administration of four antibiotics, isoniazid, rifampicin, pyrazinamide, and ethambutol, for two months, followed by isoniazid and rifampicin given for four months to kill the dormant bacteria, all drugs discovered nearly 60 years ago [94,95].

The first limitation to the efficacy of the therapy is that most of the drugs are administered by the oral route and undergo first-pass metabolism in the liver with consequent inactivation [96]. Moreover, this regimen is responsible for several adverse side effects, including liver dysfunction, peripheral neuropathy, erythromelalgia, ocular toxicity, central nervous system toxicity, gastrointestinal intolerance, and skin rash [95–97], widespread among HIV-positive

patients [98]. Another factor limiting therapy efficacy is the inadequate drug distribution in granulomatous lesions due to poor vascularization [99].

Low patient compliance due to side effects, high pill count, and prolonged duration of therapy, in addition to the misuse of antibiotics, led to the emergence of drug-resistant Mtb strains [95,100].

Isoniazid monoresistant TB is the most common drug-resistant TB [88,101]. WHO recommends treatening it with fluoroquinolones, but formal clinical studies are required to evaluate the best therapy [88].

Rifampicin monoresistant TB is increasingly documented [88,102] and currently requires the same treatment as multidrug-resistant TB. This treatment significantly changed with the introduction of bedaquiline [88,103] and delamanid [88,104] and with the increasing use of repurposed drugs such as linezolid [88,105] and clofazimine [88,106]. For the first time, the WHO-recommended therapy for rifampicin-resistant is all-oral, and 9–12 months regimens, instead of the standard 18–24 months, are being rolled out [88]. Predictably, these drugs can cause side effects like QT interval prolongation for bedaquiline [88,103], bone marrow suppression, optic neuritis, and peripheral neuropathy for linezolid [88,105], QT interval prolongation and skin discoloration for clofazimine [88,106,107]. The risk of QT interval prolongation for bedaquiline is present when it is administered in combination with other QT-interval-prolonging drugs, such as those used in resistance TB, including fluoroquinolones, delamanid, and clofazimine. Specifically, the QT-prolonging effect of bedaquiline is because it and its M2 metabolite inhibit hERG, the cardiac potassium channel. Moreover, there is a big issue related to the limited access to bedaquiline in some parts of the world [103].

4.1.5 Inhaled tuberculosis treatment

Inhaled therapies have proven stable, easy to deliver, and effective for many pulmonary diseases like asthma, chronic obstructive pulmonary disease, and cystic fibrosis [85,108–110]. Exploiting inhaled therapies would be one possible approach to improve TB therapy by

delivering drugs directly to the lung, which is the primary site of Mtb infection, and which, thanks to this approach, would be reached by high local concentrations of the drug [85,111]. Inhaled TB drugs also deserve attention in light of increasing drug resistance [85,112]. As mentioned in paragraph 4.1.2, not all orally administered TB drugs can reach therapeutic levels in tuberculous granulomas [86], and that is why inhalation, for some drugs, is the only possible way to deliver them into granulomatous lesions that harbor Mtb. Inhalation is also a potential strategy for delivering drugs with poor solubility or poor oral bioavailability that other routes cannot administer [85]. Finally, inhalation prevents repeated painful intramuscular injections required for parenteral drugs [85,113]. In summary, the advantages of switching from oral or parenteral to inhaled TB therapy would be to increase lung and macrophage distribution of the drug, reduce the treatment duration, lower the administered dose, maintain and enhance the therapy's efficacy, favor patient compliance, avoid subtherapeutic concentrations, limit drug resistance, and reduce side effects [85,114].

4.1.6 Pyrazinamide

Pyrazinamide (PZA), whose structure is depicted in Figure 23A, is a milestone antimicrobial drug used only for treating TB. Due to its ability to significantly shorten drug therapy duration and lower disease relapse rates, PZA is considered a key ingredient in the standard first-line short-course therapy for pan-susceptible TB and second-line treatment regimens for multidrug-resistant TB. PZA is highly selective against Mtb in many animal species, including mice, rabbits, nonhuman primates, humans, and guinea pigs. PZA is active against replicating, slow-growing, and interestingly also nongrowing populations of Mtb bacilli [115,116], and efficiently penetrates all tuberculous granulomas [117].

A spray-dried powder containing PZA designed for pulmonary delivery has been investigated, but it led to a relatively low drug concentration in alveolar macrophages due to the premature dissolution of the drug and its fast passage from the lungs to the blood circulation [118].

Despite decades of research, the PZA mode of action still needs to be elucidated entirely [115]. It was confirmed that the hydrolysis of PZA to pyrazinoic acid (POA), whose structure is depicted in Figure 23B, plays a leading role in its action because PZA-resistant strains do not express the Mtb pyrazinamidase/nicotinamidase [119], which is the enzyme that catalyzes the reaction, which takes place inside the mycobacterial cytoplasm. This enzyme is encoded by *pncA*, and *pncA* loss-of-function mutations are the primary mechanism for PZA resistance in clinical isolates [115,120].

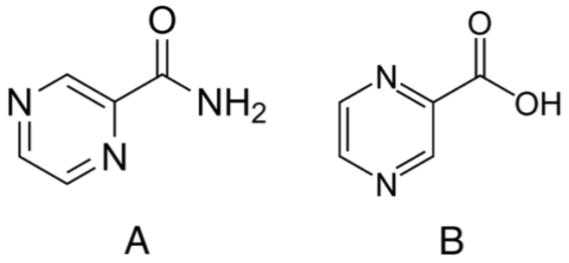

***Figure 23**. Chemical structure of PZA (A) and POA (B).*

Regarding POA mode of action, four prevailing models are currently proposed: the first model suggests that POA functions as a protonophore, the second that it inhibits mycobacterial fatty acid synthase I, the third that it binds to RpsA and inhibits *trans*-translation, the last that it blocks coenzyme A synthesis through inhibition of L-aspartate decarboxylase [115].

POA is the active form of PZA, but it cannot be used alone because it is poorly active in anti-mycobacterial tests since it cannot cross the hydrophobic bacilli cell wall due to its poor lipophilicity and high-ionized state at physiological pH [119]. For this reason, the scientific community developed POA prodrugs that do not require enzymatic activation. In this regard, novel POA esters have been prepared, and they proved to have better antimycobacterial *in vitro* activity than PZA itself against both susceptible and PZA-resistant Mtb, being their activation non-dependent on a single bacterial enzyme [121,122].

Many studies have been conducted to study nanoparticle-based anti-TB drugs suitable for pulmonary delivery [114,123,124]. However, the drug's physical loading inside the nanoparticles often led to poor loading efficiency and a burst release, as observed for PZA

physically encapsulated inside poly(D,L-lactide-*co*-glycolide) nanoparticles [123]. Physical encapsulation, besides, is well recognized to induce a drug burst release [125]. In this regard, drug-polymer conjugation, which leads to nanoconjugates instead of classic nanoparticles, has been proposed as a possible solution [126].

4.2 Aim

This third chapter aims to design a spray-dried powder of microparticles embedding innovative POA nanoconjugates (POA-NCs) for inhalation to target alveolar macrophages. This novel approach allows a system that deposits in the lungs with the delivery of microparticles and redisperses to yield nanoconjugates with the persistence advantages of nanoparticles, then disassociates in active principles through an enzymatic or hydrolytic mechanism. Exploiting nanoconjugates instead of conventional nanoparticles offers many benefits, such as good stability, high drug loading, low side effects, and sustained release without drug leakage [126]. This approach relies on easily scalable technology and requires available and cheap building blocks. We used poly (malic acid) (PMA), a water-soluble, biodegradable, biocompatible, affordable, and easily modifiable polymer [127,128]. Moreover, PMA degrades into malic acid, which is non-toxic to cells and tissues, thus foreseeing easy clinical translation. For this purpose, conjugates between POA, the active metabolite of PZA, and PMA were previously synthesized by introducing a spacer to increase stability and self-assembly properties. These conjugates will be formulated into nanoconjugates that will be spray-dried and characterized before and after spray-drying.

4.3 Previous experimental work

PMA was previously synthesized in the laboratory by polycondensation of L-malic acid under reduced pressure and without a catalyst, as shown in Figure 24, with a 70-80% yield.

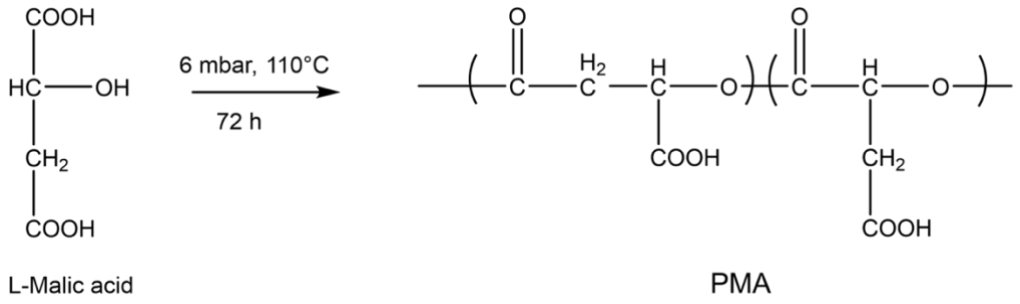

***Figure 24**. Polycondensation of malic acid.*

The second step was the esterification of POA with three different diols to obtain three different POA esters named EC_6, EC_8, and EC_{10}, as shown in Figure 25, with a yield of about 85% and with a percentage of mono-grafted product higher than 95%.

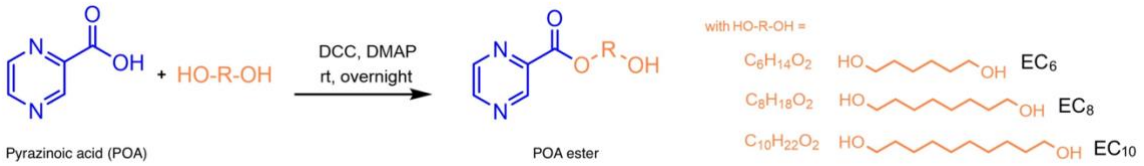

***Figure 25**. Esterification of POA and diol to yield POA ester.*

The final step was to conjugate the POA esters, EC_6, EC_8, and EC_{10}, through esterification to PMA, as shown in Figure 26, at four different ratios between POA esters and PMA, namely 10%, 25%, 50%, and 75%. Twelve different conjugates were obtained, namely $10C_6$, $25C_6$, $50C_6$, $75C_6$, $10C_8$, $25C_8$, $50C_8$, $75C_8$, $10C_{10}$, $25C_{10}$, $50C_{10}$ and $75C_{10}$, with three different spacers, namely C_6, C_8 and C_{10}. The experimental grafting rates were very close to the theoretical ones, as shown in Table 15.

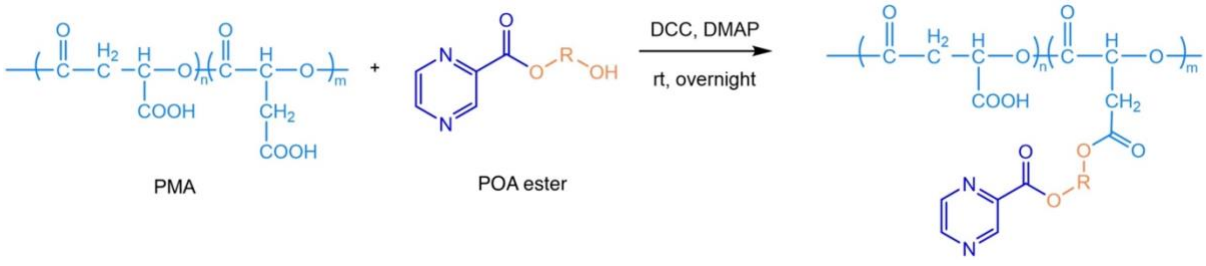

***Figure 26**. Conjugation of POA ester on PMA through esterification.*

***Table 15**. Theoretical and experimental grafting rate expressed as molar and % ratio.*

POA conjugate	Theoretical molar ratio POA:PMA	Theoretical percentage ratio	Experimental molar ratio POA:PMA	Experimental percentage ratio
10C6	1:10	10%	1:11.25	8.9%
25C6	1:4	25%	1:3.29	30.4%
50C6	1:2	50%	1:1.65	60.6%
75C6	1:1.33	75%	1:1.26	79.4%
10C8	1:10	10%	1:11.83	8.5%
25C8	1:4	25%	1:3.83	26.1%
50C8	1:2	50%	1:1.41	70.9%
75C8	1:1.33	75%	1:1.34	74.6%
10C10	1:10	10%	1:8.69	11.5%
25C10	1:4	25%	1:3.59	27.9%
50C10	1:2	50%	1:1.7	58.8%
75C10	1:1.33	75%	1:1.28	78.1%

All data were acquired and confirmed by NMR (data not shown).

4.4 Experimental work

4.4.1 Materials and Methods

4.4.1.1 Materials

- ACN (CH_3CN, ACETONITRILE RS PLUS - For HPLC Gradient- ACS- Reag.Ph.Eur.-Reag.USP, CARLO ERBA Reagents, Val-de-Reuil, France)
- Ammonium bicarbonate (CH_5NO_3, Ammonium bicarbonate ReagentPlus®, ≥99.0%, Lot #030M0144, MW 79.06 g/mol, Sigma-Aldrich, Saint-Louis, United States)
- Calcium chloride dihydrate ($CaCl_2 \cdot 2H_2O$, ≥99%, Lot #MKBX7059V, MW 147.01 g/mol, Sigma-Aldrich, Saint-Louis, United States)
- Esterase (Esterase from porcine liver, lyophilized powder, 19 units mg/solid, MW 168 kDa, source SLCK7683, Sigma-Aldrich, Saint-Louis, United States)
- Three different esters of POA named EC_6, EC_8, and EC_{10} were previously synthesized in this laboratory as described above in paragraph 4.3

- Lactose ($C_{12}H_{22}O_{11}\cdot 1H_2O$, Lactose monohydrate, GPR RECTAPUR®, Lot #84172, MW 360.32 g/mol, VWR International, Radnor, United States)
- Lipase (Lipase from *Pseudomonas sp.* - Type XIII, lyophilized powder, 33 units mg/solid, source SLCN6689, Sigma-Aldrich, Saint-Louis, United States)
- L-Leucine ($C_6H_{13}NO_2$, L-Leucine from non-animal source, 98.5-101.1%, Lot #SLBW8571, MW 131.17 g/mol, Sigma-Aldrich, Saint-Louis, United States)
- Magnesium chloride hexahydrate ($MgCl_2\cdot 6H_2O$, Lot #054K01501, MW 203.30 g/mol, Sigma-Aldrich, Saint-Louis, United States)
- Mannitol ($C_6H_{14}O_6$, D-Mannitol, ≥98%, Lot #WXBC9444V, MW 182.17 g/mol, Sigma-Aldrich, Saint-Louis, United States)
- Milli-Q water purified by reverse osmosis (MilliQ, Millipore, Molsheim, France)
- NaCl 1 mM was obtained by dissolving NaCl in milli-Q water at the concentration of 58.45 mg/L, then filtering the solution with a 0.22 µm filter
- PBS tablet (Lot #SLCK3649, Sigma-Aldrich, Saint-Louis, United States)
- PBS 10X was obtained by dissolving 1 PBS tablet in 20 mL of milli-Q water
- 25 mM phosphate buffer was obtained by dissolving KH_2PO_4 in milli-Q water at the concentration of 4.25 g/L, adjusted to pH 2 with H_3PO_4, sonicated for 20 min with an ultrasonic bath (Sonorex super rk 52, Bandelin, Germany) and filtered with a vacuum pump equipped with a 0.22 µm filter
- POA ($C_5H_4N_2O_2$, Pyrazinecarboxylic acid, >98.0%, Lot #8ZR4D-FJ, MW 124.10 g/mol, TCI Europe N.V., Montaigne, France)
- Twelve different POA conjugates named $10C_6$, $25C_6$, $50C_6$, $75C_6$, $10C_8$, $25C_8$, $50C_8$, $75C_8$, $10C_{10}$, $25C_{10}$, $50C_{10}$, and $75C_{10}$ previously synthesized in this laboratory as described above in paragraph 4.3
- Potassium chloride (KCl, Potassium chloride -BioXtra, ≥99.0%, Lot #BCBQ2623V, MW 74.55 g/mol, Sigma-Aldrich, Saint-Louis, United States)
- Potassium dihydrogen phosphate (KH_2PO_4, Lot #41197, MW 136.09 g/mol, Fluka™, Charlotte, United States)

- Sodium acetate ($C_2H_3NaO_2$, Sodium acetate anhydrous, ≥99%, Lot #BCBR7028V, MW 82.03 g/mol, Sigma-Aldrich, Saint-Louis, United States)
- Sodium bicarbonate ($NaHCO_3$, Sodium bicarbonate puriss. P.a., ACS reagent, reag. Ph. Eur., ≥99.7%, Lot #STBH3549, MW 84.01 g/mol, Sigma-Aldrich, Saint-Louis, United States)
- Sodium chloride (NaCl, Sodium chloride anhydrous, ≥99%, Lot #SLBZ3816, MW 58.44 g/mol, Sigma-Aldrich, Saint-Louis, United States)
- Sodium citrate ($Na_3C_6H_5O_7$, >99%, MW 258.06 g/mol, Fluka™, Charlotte, United States)
- Sodium dihydrogen phosphate (NaH_2PO_4, ≥98%, Lot #249AP, MW 119.98 g/mol, Fluka™, Charlotte, United States)
- Sodium hyaluronate (95%, Lot #A0307654, CAS 9067-32-7, Acros Organics, Geel, Belgium)
- Sodium sulphate decahydrate ($Na_2SO_4 \cdot 10H_2O$, ≥99.0%, Lot #92230, MW 322.2 g/mol, VWR International, Radnor, United States)
- THF (C_4H_8O, Tetrahydrofuran HiPerSolv CHROMANORM® for HPLC, Lot #190703A003, VWR International, Radnor, United States)

4.4.1.2 Methods

4.4.1.2.1 Analytical method for POA, EC_6, EC_8, and EC_{10} content determination

To quantify POA, EC_6, EC_8, and EC_{10}, an HPLC method was adapted from the one described by Simões et al. [122]. The system comprised a 1525 Binary HPLC Pump, 2707 Autosampler, In-Line Degasser AF, and 2998 Photodiode Array Detector (Waters, USA). A SynergiTM 4 µm Hydro-RP 80 Å LC Column 250 x 4.6 mm protected by a precolumn equipped with SecurityGuard Cartridges AQ C18 4 x 3.0 mm ID (Phenomenex, USA) was employed with gradient elution mode. The mobile phase was a gradient of ACN (Eluent B) and 25 mM phosphate buffer adjusted at pH 2 (Eluent A) at a flow rate of 1 mL min^{-1} (Table 16). The detection wavelength was set at 267 nm. One analysis was conducted at 35 °C for 35 min with

an injection volume of 10 µL. Under these conditions, the retention time of POA was ≈ 4.9 min, EC_6 ≈ 14.8 min, EC_8 ≈ 16.3 min, and EC_{10} ≈ 18 min. The POA, EC_6, EC_8, and EC_{10} calibration curves were obtained by injecting five standard solutions at increasing concentrations and were assessed between 1 and 50 µg/mL. The calibration curve equation for POA is y = 39084x – 11420, for EC_6 y = 22260x – 327.64, for EC_8 y = 18997x – 1132.9, and for EC_{10} y = 14547x – 944.47.

***Table 16**. Gradient composition of mobile phase as eluent A (25 mM phosphate buffer adjusted at pH 2) and eluent B (ACN) at different time points.*

Time (min)	Eluent A (%)	Eluent B (%)
	95.0	5.0
7.0	95.0	5.0
15.00	25.0	75.0
20.00	25.0	75.0
25.00	95.0	5.0

4.4.1.2.2 POA-NCs formulation

POA-NCs were prepared with the nanoprecipitation method. POA conjugate was dissolved in tetrahydrofuran (THF) at 10 mg/mL. Subsequently, the POA conjugate solution was injected into milli-Q water at a fixed volume ratio 1:10 under moderate magnetic stirring. THF was then evaporated, keeping the system under magnetic stirring for 1.5h, yielding POA-NCs at 1 mg/mL.

4.4.1.2.3 POA-NCs size distribution and surface charge characterization

POA-NCs freshly prepared according to paragraph 4.4.1.2.2 were characterized with dynamic light scattering (DLS) by particle size, polydispersity index (PdI), and zeta-potential with a Zetasizer Nano ZS (Malvern Instruments, UK). For particle size and PdI analysis, POA-NCs were diluted 1:10 with milli-Q water, and for zeta-potential analysis, they were diluted 1:20 with NaCl 1 mM. Analysis was carried out at 25 °C.

4.4.1.2.4 POA-NCs stability test

POA-NCs were stored at 4 °C. The stability of these nanoconjugates was followed for 20 days by analyzing particle size, PdI, and zeta-potential at six-time points: after their preparation, considered day 0, and after 1, 3, 6, 10, and 20 days from day 0. The analysis of particle size, PdI, and zeta-potential was carried out as described above in paragraph 4.4.1.2.3.

4.4.1.2.5 *In vitro* release of POA, EC_6, EC_8, and EC_{10} from POA-NCs

The release of POA and EC_6 from $10C_6$, $25C_6$, $50C_6$, $75C_6$, POA and EC_8 from $10C_8$, $25C_8$, $50C_8$, $75C_8$, and POA and EC_{10} from $10C_{10}$, $25C_{10}$, $50C_{10}$ and $75C_{10}$ nanoconjugates (NCs) were assessed in phosphate-buffered saline (PBS) 10X. Briefly, POA-NCs prepared according to paragraph 4.4.1.2.2 were diluted with 10X PBS yielding POA at 40 µg/mL and divided into 10 aliquots of 1 mL each. One aliquot was immediately frozen, corresponding to t = 0, while other aliquots were moved into an incubator shaker (KS 4000I control, IKA®, Germany) at 37 °C and frozen after 0.3, 1, 1.3, 2, 2.3, 3, 3.3, and 6 days, respectively. Frozen aliquots were then thawed, filtered with PTFE 0.22 µm, and analyzed with HPLC according to paragraph 4.4.1.2.1.

4.4.1.2.6 POA-NCs enzymatic degradation

Enzymatic degradation of $25C_6$ and $75C_6$ NCs was measured in the presence of esterase from porcine liver or lipase from *Pseudomonas sp.* The scattered light intensity was followed in terms of derived count rate (DCR) at different time points for up to one day with a Zetasizer Nano ZS (Malvern Instruments, UK). The DCR was presented as normalized derived count rate (nDCR). At the beginning of the experiment, an appropriate amount of esterase or lipase solutions in PBS 10X, respectively 10 U/mL and 8 U/mL, was added to 1 mg/mL POA-NCs to initiate the degradation. The final concentrations of the enzymes and the $25C_6$ NCs were 0.36 U/mL lipase in 0.955 mg/mL POA-NCs and 0.1 U/mL esterase in 0.99 mg/mL POA-NCs. For the negative control, an appropriate amount of PBS 10X was added to 1 mg/mL POA-NCs, yielding 0.955 mg/mL POA-NCs (for negative control in case of using lipase) and 0.99 mg/mL

POA-NCs (for negative control in case of using esterase). The negative controls' nDCR was checked only at t = 0 and t = 1 day. For the whole duration of the study, all samples were kept in an incubator shaker (KS 4000i control, IKA®, Germany) at 37 °C.

4.4.1.2.7 Transmission electron microscopy

The morphology of $25C_6$, $50C_6$, and $75C_6$ NCs freshly prepared was analyzed with transmission electron microscopy (TEM). 5 µL of POA-NCs was deposited onto copper grids coated with a formvar film (400 mesh) for 2 min. Then, 5 µL of a 0.5% w/v uranyl acetate solution was deposited onto the grid for 30 sec for negative staining. Colorant excess was removed with a filter paper, and samples were observed in a JEOL JEM-1400 microscope operating at 80 kV with a filament current of about 55 µA, a post-column high resolution (11 megapixels), and a high-speed camera (SC1000 Orius; Gatan). Data were acquired using Digital Micrograph (Gatan).

4.4.1.2.8 Preparation of spray-dried powders without the active substance

Leucine, lactose, ammonium bicarbonate, mannitol, and sodium hyaluronate, were tested to produce a spray-dried powder with adequate properties for deep lung delivery. From different combinations of these excipients, by varying the spray drying conditions, such as inlet temperature and feed rate, we obtained 15 powders (Table 17). The feed solutions were prepared using milli-Q water. Regarding powders #6, 7, 14, and 15, the two solutions forming the binary mixture were prepared separately and mixed before spray drying. Regarding powders #6 and 7, ammonium bicarbonate solutions were prepared shortly before being added to the leucine 4 g/L solution and then spray-dried to avoid sublimation. The final solutions were spray-dried employing a Mini Spray Dryer B-290 (Büchi Labortechnik AG, Flawil, Switzerland) equipped with a 0.7 mm two-fluid nozzle, keeping the following process parameters constant: 38 m^2/h drying air flow rate (aspiration) and 667 L/h nebulization gas rate (at standard conditions). The yield was calculated as the percentage between the powder collected from

the collector and the amount of solute dissolved in milli-Q water. Obtained powders were stored in a desiccator under vacuum at room temperature to avoid moisture absorption.

***Table 17**. Composition and volume of the feed solution, inlet temperature, and feed rate set for producing 15 different spray-dried powders without the active substance.*

#	Sub 1	Sub 1 (g/L)	Sub 2	Sub 2 (g/L)	Inlet temperature (°C)	Feed solution volume (mL)	Solution feed rate (mL/min)
1					150	200	12
2					120	100	12
3	Leucine	4	-	-	160	50	12
4					160	100	12
5					160	500	12
6	Leucine	4	Ammonium bicarbonate	1	160	100	12
7	Leucine	4	Ammonium bicarbonate	2	160	100	12
8	Lactose	4	-	-	120	100	9
9					160	100	9
10					120	100	9
11	Mannitol	4	-	-	160	100	9
12					120	100	12
13					160	100	12
14	Mannitol	2	Leucine	2	160	100	12
15	Leucine	3.8	Sodium hyaluronate	0.2	160	100	12

4.4.1.2.9 Particle size distribution analysis by laser diffraction

The particle size distribution of the spray-dried powders was assessed by laser diffraction with a Mastersizer 2000 equipped with a Sirocco dry disperser (Malvern Panalytical, Worcestershire, United Kingdom). Data were expressed as Dv50 and Span value, which was calculated according to Equation 7.

4.4.1.2.10 Preparation of spray-dried powders with the NCs

Two powders of $25C_6$ NCs, leucine, and sodium hyaluronate microparticles, were prepared; their composition is listed in Table 18. $25C_6$ NCs were prepared according to paragraph 4.4.1.2.2, while leucine and sodium hyaluronate were dissolved in milli-Q water under

magnetic stirring. Then, $25C_6$ NCs were added to leucine and sodium hyaluronate solution before spray drying. The final solutions were spray-dried employing a Mini Spray Dryer B-290 equipped with a 0.7 mm two-fluid nozzle, keeping the following process parameters constant: 12 mL/min solution feed rate, 38 m^2/h drying air flow rate (aspiration) and 667 L/h nebulization gas rate (at standard conditions), 160 °C inlet temperature, and 100 mL feed solution volume. The spray drying yield was calculated as described in paragraph 4.4.1.2.8. Obtained powders were stored in a desiccator under vacuum at room temperature to avoid moisture absorption.

***Table 18**. Composition of the feed solution for producing two different spray-dried powders with the active substance.*

#	Sub 1	Sub 1 (g/L)	Sub 2	Sub 2 (g/L)	Sub 3	Sub 3 (% w/w)
16	Leucine	3.61	Sodium hyaluronate	0.19	$25C_6$	5
17	Leucine	3.42	Sodium hyaluronate	0.18	$25C_6$	10

4.4.1.2.11 Powder disaggregation in simulated lung fluid

The ability of $25C_6$ NCs to redisperse from powders #16 and 17 (Table 18) was studied by dissolving the powders in a simulated lung fluid (SLF) (Table 19, [129]). Briefly, powder #16 was dissolved in SLF at 2 g/L, while powder #17 was dissolved in SLF at 1 g/L, yielding a final theoretical concentration of $25C_6$ NCs equal to 0.1 mg/mL. A good dissolution was achieved by vortexing for 1 minute and shaking for 30 min in an incubator shaker (KS 4000i control, IKA®, Germany) at 37 °C. Particle size, PdI, and zeta-potential were then investigated with a Zetasizer Nano ZS (Malvern Instruments, UK). Analysis was carried out at 25 °C.

***Table 19**. Composition of SLF* [129].

Substance	Concentration (g/L)
Magnesium chloride hexahydrate	0.2033
Sodium chloride	6.0193
Potassium chloride	0.2982
Sodium sulfate decahydrate	0.1610
Calcium chloride dihydrate	0.3676
Sodium acetate anhydrous	0.5742
Sodium hydrogen carbonate	2.6043
Sodium citrate anhydrous	0.0850
Sodium dihydrogen phosphate	0.1092

4.4.1.2.12 Statistical analysis

All experiments were conducted at least in triplicate. Unless otherwise stated, data are presented as mean value ± standard deviation.

4.4.2 Results and discussion

4.4.2.1 POA-NCs dimensional analysis and surface charge

Twelve different conjugates, namely $10C_6$, $25C_6$, $50C_6$, $75C_6$, $10C_8$, $25C_8$, $50C_8$, $75C_8$, $10C_{10}$, $25C_{10}$, $50C_{10,}$ and $75C_{10}$, were previously synthesized in the laboratory as described in paragraph 4.3, by combining three different spacers and four different ratios between POA and PMA. With these twelve conjugates, POA-NCs were prepared in milli-Q water following a simple nanoprecipitation method [130] without employing any surfactant. PMA is soluble in water [131] but becomes insoluble after conjugation with POA. These conjugates were soluble in THF, which spontaneously self-assembled in nanoconjugates in water thanks to their amphiphilic properties. The portion of the nanoconjugate composed of POA would form the hydrophobic core of the system. At the same time, we would find chains of PMA with carboxylic acid functions oriented toward water at the surface. POA-NCs were then characterized in terms of particle size, PdI, and zeta-potential as described in paragraph 4.4.1.2.3; results are shown in Table 20.

***Table 20**. Particle size, PdI, and zeta-potential of freshly prepared POA-NCs.*

POA-NCs	Size (nm)	PdI	Zeta-potential (mV)
$10C_6$ NCs	128 ± 1	0.15 ± 0.1	-47 ± 1
$25C_6$ NCs	150 ± 2	0.12 ± 0.1	-67 ± 2
$50C_6$ NCs	165 ± 2	0.12 ± 0.1	-70 ± 1
$75C_6$ NCs	132 ± 1	0.12 ± 0.1	-68 ± 1
$10C_8$ NCs	161 ± 4	0.13 ± 0.1	-72 ± 2
$25C_8$ NCs	148 ± 2	0.14 ± 0.1	-69 ± 5
$50C_8$ NCs	135 ± 2	0.14 ± 0.1	-81 ± 3
$75C_8$ NCs	137 ± 1	0.12 ± 0.1	-68 ± 4
$10C_{10}$ NCs	113 ± 5	0.23 ± 0.1	-47 ± 8
$25C_{10}$ NCs	113 ± 2	0.12 ± 0.1	-55 ± 5
$50C_{10}$ NCs	136 ± 3	0.15 ± 0.1	-82 ± 6
$75C_{10}$ NCs	125 ± 2	0.14 ± 0.1	-73 ± 4

Results indicated the POA-NCs prepared from the nanoprecipitation method had a diameter from 113 to 165 nm, a size range advantageous for targeting macrophages after lung administration because particles of less than 70 nm appear unable to be recognized and be uptaken by the lungs' surface alveolar macrophages, thus resulting in their access to the pulmonary interstitium and then capillary blood flow [132,133]. It is observed that in the presence of a C_{10} spacer, compared to C_6 and C_8, the size was smaller (≈ 113 to 136 nm against ≈ 128 to 165 nm, Table 20), which was explained by the increase in the hydrophobicity of the system due to the increasing length of the carbon chain that constituted the spacer itself. In other words, the more hydrophobic the POA-NCs are, the more compact and smaller they will be in water. The PdI was always below ≈ 0.2, meaning that the POA-NCs population was monodisperse with a narrow distribution. Zeta-potential showed that the POA-NCs were negatively charged because of non-conjugated carboxylic residues of PMA exposed to the aqueous solvent, which also provides colloidal stability to the system, avoiding aggregation by electrostatic repulsions.

4.4.2.2 POA-NCs stability

Stability over 20 days was evaluated by following particle size, PdI, and zeta-potential of POA-NCs, stored at 4 °C. Results are shown in Figure 27.

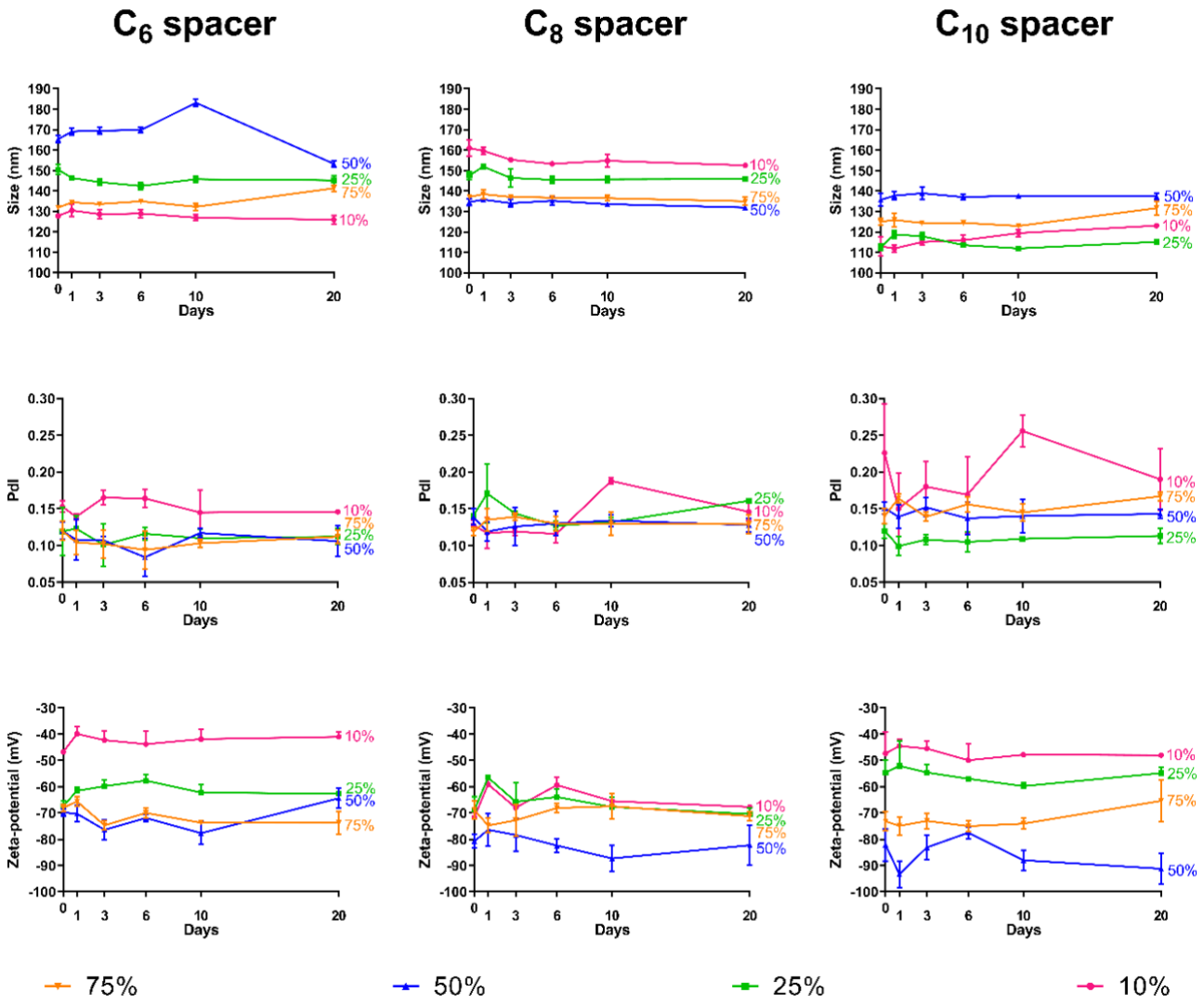

***Figure 27**. Stability tests performed for POA-NCs stored at 4 °C for 20 days, represented in terms of particle size, PdI, and zeta-potential.*

In the case of $10C_6$, $10C_8$, and $10C_{10}$ NCs, the analysis shows a fluctuating PdI, which significantly exceeded the value of 0.2 in the case of $10C_{10}$ on day 10 (Figure 27). For $50C_6$, the NCs started to get unstable after 1 week, as shown by an increase in particle size (Figure 27). In other cases, POA-NCs remained stable over time, with a PdI kept under 0.2, suggesting no aggregation. The surface charge of the POA-NCs remained strongly negative for the whole study, proving to confer sufficient colloidal stability to the systems. All this evidence further confirmed that POA-NCs could be formulated without surfactant, thus avoiding related toxicity. Another advantage is that the drug was covalently bound to the polymer, and so the loading of POA was equal to the grafting rate, ranging from 8.5% to 79.4% (Table 15), which are higher than those previously obtained by physical encapsulation of PZA in poly(D,L-lactide-*co*-glycolide) nanoparticles (around 3-4% w/w) [123].

4.4.2.3 Transmission electron microscopy

The morphology of $25C_6$, $50C_6$, and $75C_6$ NCs freshly prepared according to paragraph 4.4.1.2.2 was analyzed by TEM with negative staining to understand their morphology and to confirm particle size measured with DLS. The results are shown in Figure 28.

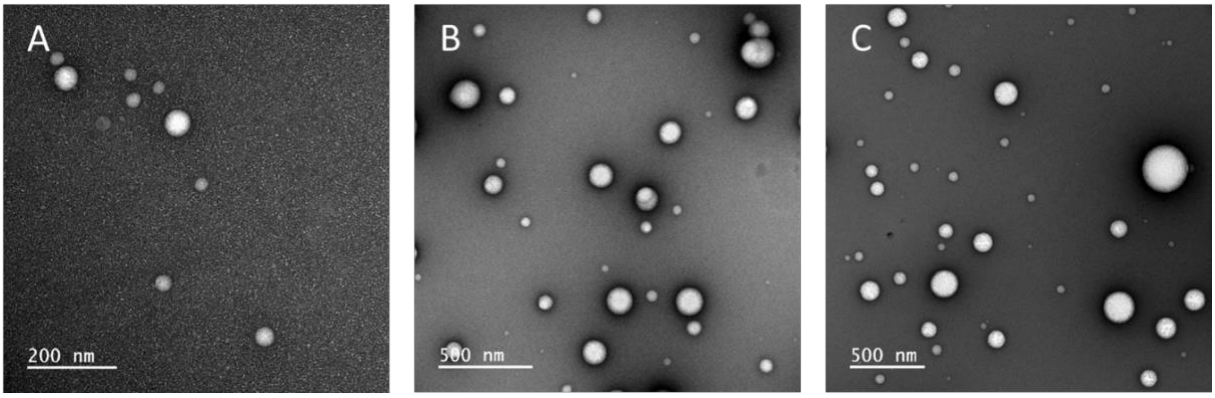

***Figure 28**. TEM images with negative staining of $25C_6$ NCs (A), $50C_6$ NCs (B), and $75C_6$ NCs (C).*

TEM imaging showed that all POA-NCs analyzed were spherical, and no aggregates were observed. Results were consistent with DLS measurements (Table 20), confirming their nanometric size and the relatively narrow size distribution.

4.4.2.4 In vitro release of POA, EC_6, EC_8, and EC_{10} from POA-NCs

The release percentage rates of POA and EC_6 from $10C_6$, $25C_6$, $50C_6$, and $75C_6$ NCs, POA and EC_8 from $10C_8$, $25C_8$, $50C_8$, and $75C_8$ NCs, and POA and EC_{10} from $10C_{10}$, $25C_{10}$, $50C_{10}$, and $75C_{10}$ NCs were followed up to 6 days in PBS 10X. We followed up both POA and POA esters (EC_6, EC_8, and EC_{10}) because ester analogs proved to be potential active principles against Mtb in recent studies [134]. Results are shown in Figure 29 and Figure 30.

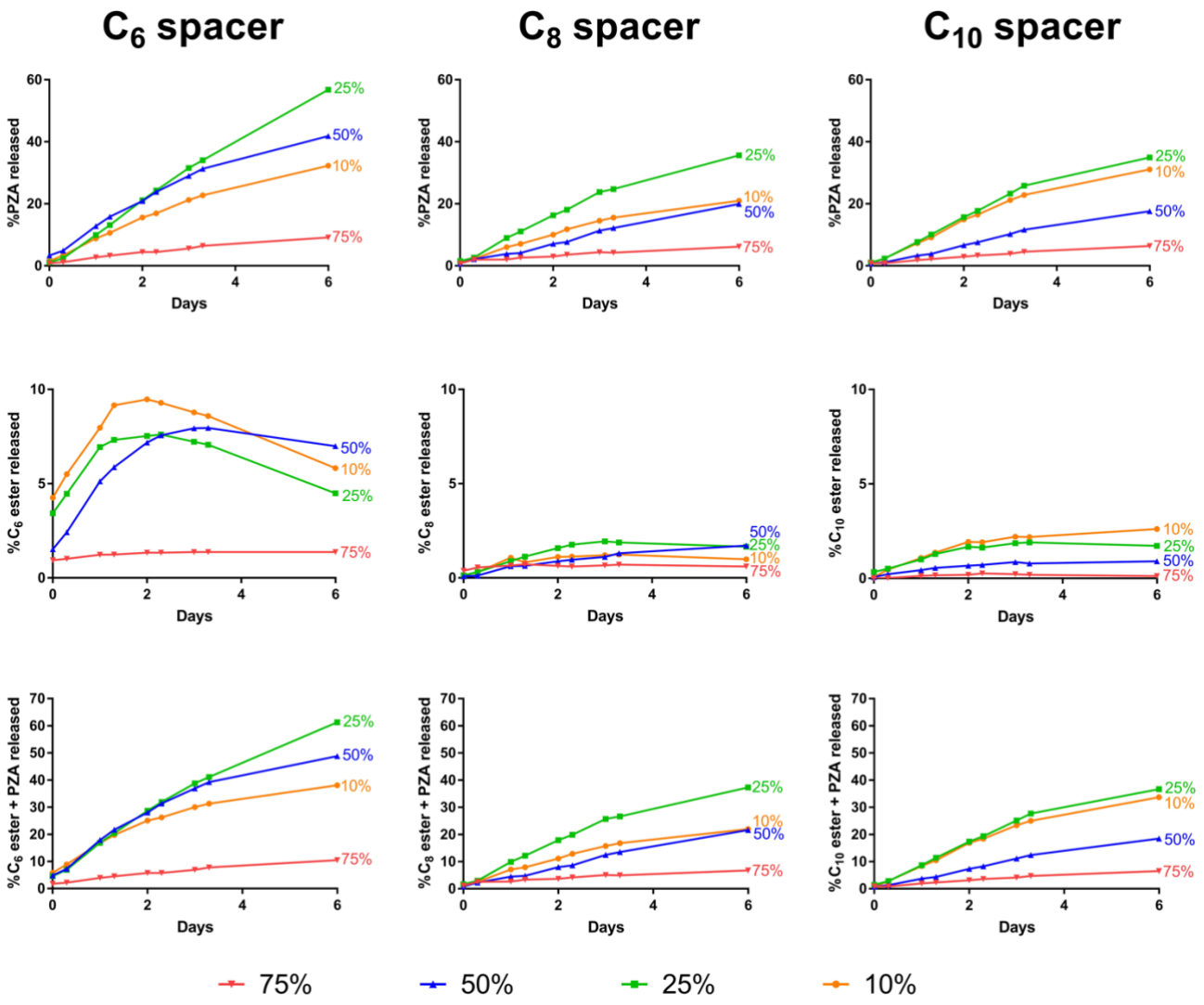

***Figure 29**. In vitro POA, POA esters, and POA+POA esters percentage release in PBS 10X at 37 °C from POA-NCs represented divided per spacer.*

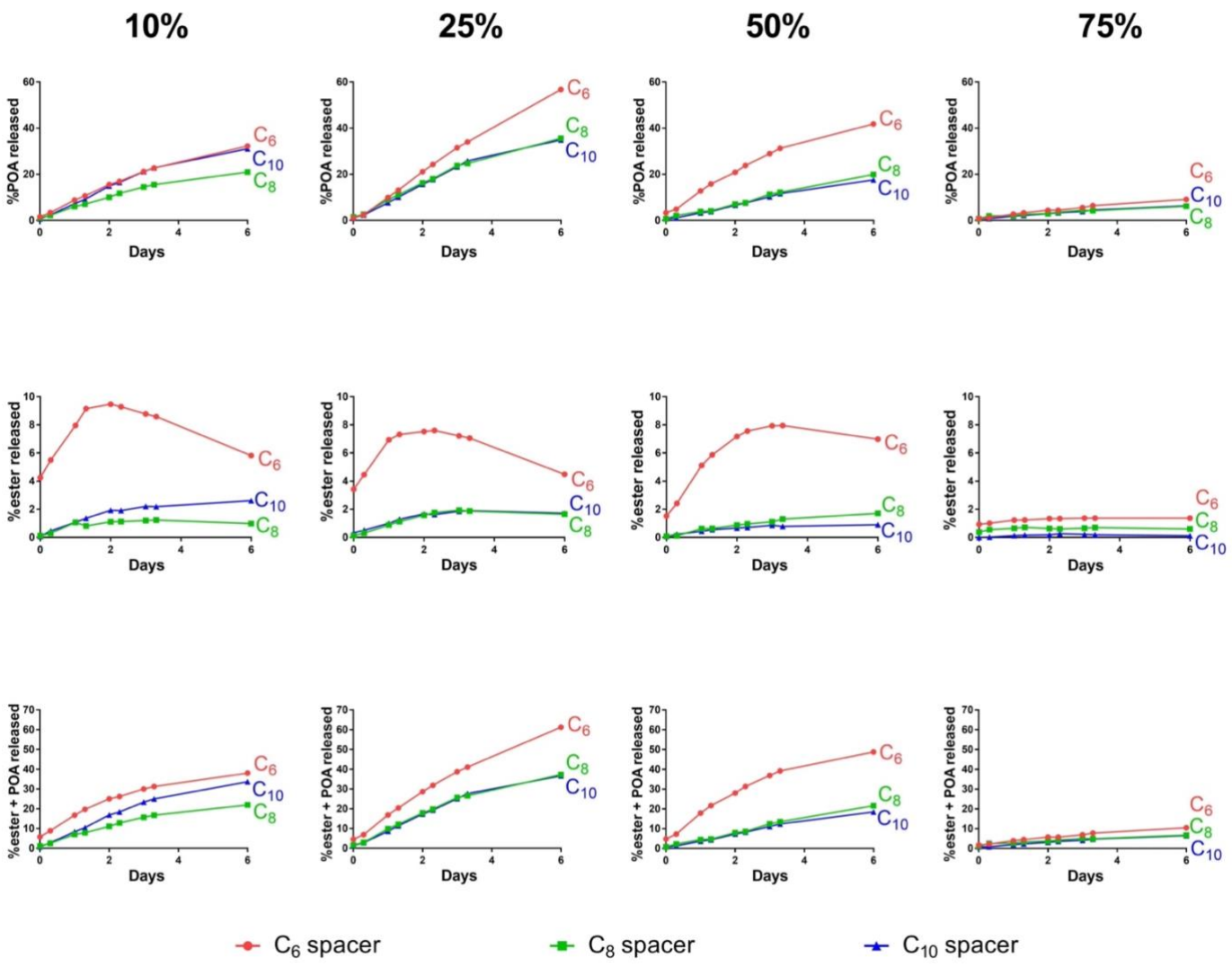

***Figure 30**. In vitro POA, POA esters, and POA+POA esters percentage release in PBS 10X at 37 °C from POA-NCs represented divided per ratio between POA esters and PMA.*

Figure 29 shows that the kinetics of POA and POA esters released from POA-NCs were gradual and progressive, reaching maximum values of ≈ 60% of POA released for $25C_6$ NCs, and ≈ 10% of EC_6 released for $10C_6$, $25C_6$, and $50C_6$ NCs at the end of the six days. The active principles, POA and POA esters, were released slowly through the hydrolysis of ester bonds, solving the problem of burst release, which occurs when the loaded drug is released in the first few minutes of contact with an external medium [135]. Burst release is a common problem for nanosystems [135], especially when the drug is physically entrapped in the carrier [123,125]. With C_8 and C_{10} spacers, the total amount of POA released in 6 days was lower, with a maximum value of ≈ 40% for $25C_8$, $25C_{10}$, and $10C_{10}$ NCs, and a maximum value lower than ≈ 5% for the POA ester (Figure 29). Figure 29 also shows that the release of POA was always higher for the 25% grafting rate compared to 75%. This was because POA-NCs with a 75% grafting ratio are the richest in POA, and their release was low because the core is compact and water struggles to access and hydrolyze ester bonds. Finally, it is essential to point out that POA release decreases as the grafting rate percentage increases, except for the 10% grafting rate, which release is in between and does not follow the progression observed in the other cases. Figure 30 shows that POA release was always higher for spacer C_6 than C_8 and C_{10}.

We have focused on 25C6 NCs based on these results because they released more POA in PBS 10X. It's important to consider that the PBS 10X, the medium employed in this study, differs from the environment inside endo-lysosomes of alveolar macrophages [136] in which there are many enzymes and an acidic pH [117], which should result in higher and faster release.

A second replicate of the experiment was done to confirm the results obtained during the first experiment, focusing on POA-NCs with spacer C_6 only and excluding the 10% ratio as it yielded less stable NCs (Figure 27). The results are shown in Figure 31.

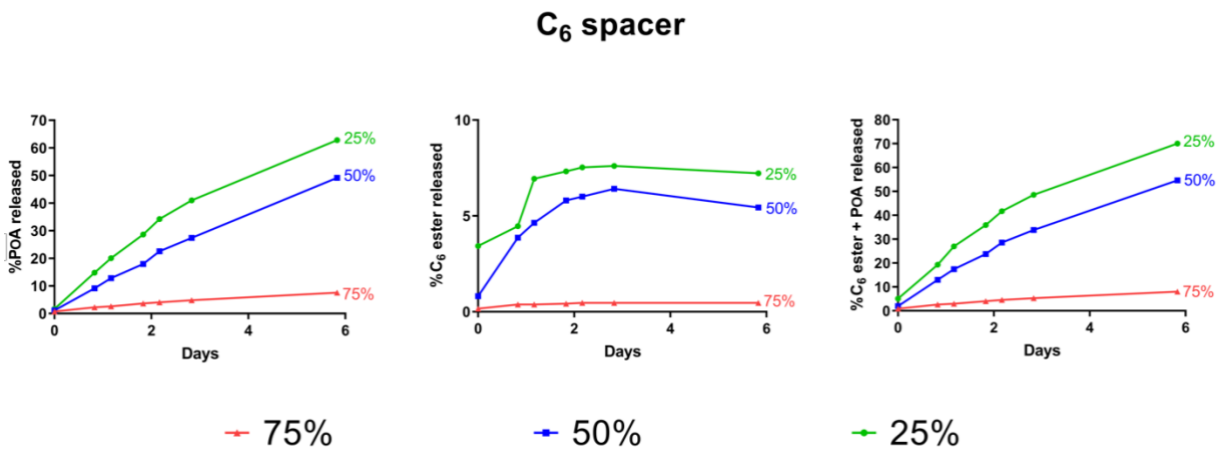

***Figure 31**. In vitro POA, EC_6, and POA+EC_6 release in PBS at 37 °C.*

Once again, as visible from Figure 31, the 25% ratio between POA esters and PMA proved to release more POA, reaching a maximum value of ≈ 70% of POA and ≈ 5-10% of EC_6, reinforcing our choice to focus from now on only on $25C_6$ NCs.

4.4.2.5 POA-NCs enzymatic degradation

Because the environment inside endo-lysosomes of alveolar macrophages [136] is rich in enzymes, we analyzed the enzyme-catalyzed degradation of $25C_6$ and $75C_6$ NCs with DLS following the nDCR, which is independent of the used attenuator setting, adapting the method from previous studies [137,138] and in the presence of esterase from porcine liver or lipase from *Pseudomonas sp.* We chose lipase isolated from *Pseudomonas sp.* because it is usually regarded as a model of lipase activity and because this type of lipase demonstrates higher activity and better efficiency compared to mammalian lipases such as lipase derived from the porcine pancreas [138]. The final lipase concentration, 0.36 U/mL, was chosen based on the same study [138]. The final concentration of esterase, 0.05 U/mL, was determined based on another study [139]. During the DLS experiment, degradation was observed as a decrease in the nDCR. $75C_6$ NCs were included in the study for comparative purposes. Results are shown in Figure 32, while Table 21 shows nDCR values for negative controls at the end of the experiment.

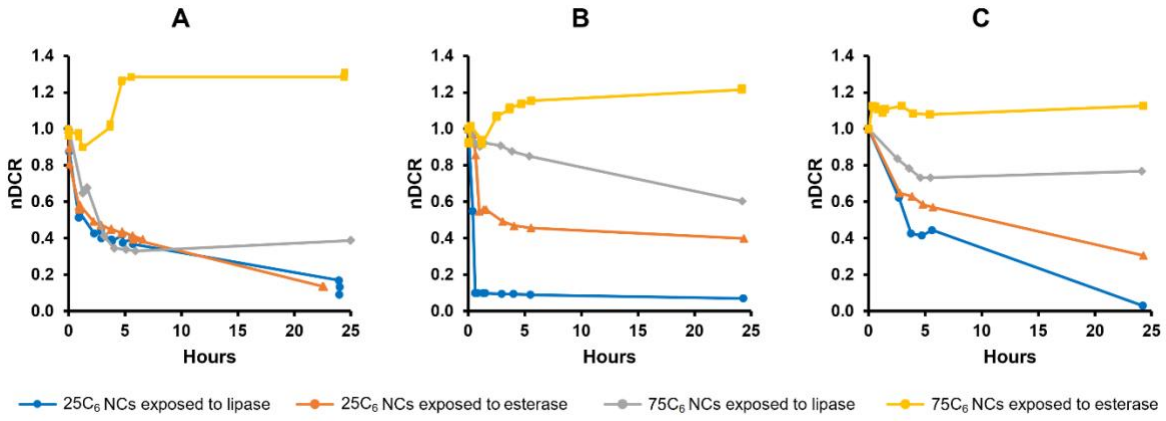

***Figure 32**. Enzymatic degradation study of 25C_6 and 75C_6 NCs exposed to esterase and lipase made in three replicates: 1st (A), 2nd (B), and 3rd (C).*

***Table 21**. nDCR of negative controls at the end of the experiment.*

POA-NCs	Enzyme	nDCR after 24 h
25C_6 NCs	lipase	0.92 ± 0.54
25C_6 NCs	esterase	0.84 ± 0.06
75C_6 NCs	lipase	1.07 ± 0.36
75C_6 NCs	esterase	1.18 ± 0.27

Figure 32 shows that an evident degradation occurred in the case of 25C_6 NCs exposed to esterase with the nDCR ≈ 0.5 five hours after the start of the experiment and ≈ under 0.4 at the end when the negative control was ≈ 0.84. Figure 32 shows no degradation in the case of 75C_6 NCs exposed to esterase, and the little increase in the nDCR at the end of the study is possibly due to the evaporation in the cuvette at 37 °C. In this case, degradation was absent probably because, as mentioned above, the core of these POA-NCs is very compact, hindering the entry of water and the action of enzymes. An intense and fast degradation also occurred for 25C_6 NCs exposed to lipase, for which the nDCR reached ≈ 0.1 after 24 h when the negative control was still at ≈ 0.92. Finally, degradation was observed for 75C_6 NCs exposed to lipase, for which the nDCR continuously decreased, reaching ≈ 0.4, while the negative control was ≈ 1.07 after 24 h.

4.4.2.6 Preparation of spray-dried powders without the active substance

We aimed to understand which excipient, or combination of excipients, allows us to obtain large porous microparticles of around 5 µm. Later, at the selected combination, POA-NCs will be added to get a system that deposits in the lungs with the delivery convenience of microparticles and disassociates to yield nanoconjugates. This system allows a good distribution of microparticles in the deep lung thanks to the micrometric sizes. Then, upon dispersion, NCs will interact with the macrophages [140]. In this regard, leucine, lactose, ammonium bicarbonate, mannitol, and sodium hyaluronate have been tested for the production of a spray-dried powder varying the volume of the feed solution, the inlet temperature, and the feed rate (Table 17), obtaining 15 different powders. Table 22 shows the outlet temperature registered during the spray drying process, the yield of the process, Dv50, and the Span of the obtained powders.

***Table 22**. Outlet temperature, yield, Dv50, and Span for the 15 spray-dried powders produced without the active substance.*

#	Outlet temperature (°C)	Yield (%)	Dv50 (µm)	Span
1	50*	65*	3.1 ± 0.1	2.1 ± 0.1
2	33*	54*	4.8 ± 0.2	2.3 ± 0.1
3	60.1 ± 0.0	56.5 ± 2.1	3.0 ± 0.2	2.1 ± 0.1
4	60.7 ± 7.0	56.3 ± 9.6	2.6 ± 0.2	1.9 ± 0.1
5	54.5 ± 6.3	66.0 ± 1.4	3.5 ± 0.4	1.7 ± 0.1
6	51.5 ± 2.1	86.0 ± 7.0	3.0 ± 0.4	1.8 ± 0.1
7	51.5 ± 0.7	69.5 ± 27.6	3.0 ± 0.4	1.8 ± 0.1
8	40*	0*	-	-
9	62*	0*	-	-
10	40*	74*	2.2 ± 0.1	1.9 ± 0.1
11	70*	53*	2.6 ± 0.1	1.8 ± 0.2
12	37*	56*	2.67 ± 0.2	1.6 ± 0.2
13	57.7 ± 5.7	63.7 ± 5.5	2.1 ± 0.1	1.9 ± 0.7
14	56.3 ± 4.2	74.7 ± 3.1	3.0 ± 0.3	1.9 ± 0.1
15	60.3 ± 6.4	52.7 ± 4.5	4.0 ± 0.4	2.0 ± 0.1

*Standard deviation is missing because the experiment was not repeated

In the first attempt, leucine was spray-dried with an inlet temperature of 120, 150, and 160 °C (powders #1-5, Table 17). However, 120 and 150 °C inlet temperatures (powders #1 and 2,

Table 17) were discarded because of humidity formed in the drying chamber during the spray-drying process, with possible residual moisture in the final powder. Then, 160 °C inlet temperature was tested with a feed solution volume of 50, 100, and 500 mL (powders #3-5, Table 17). The outlet temperatures went from ≈ 54 to 60 °C (powders #3-5, Table 22), corresponding to two different cyclones used. A slight variation in the outlet temperature is also ascribable to the state of the filter. For 500 mL feed solution volume, the yield of ≈ 66% and the Dv50 of ≈ 3.5 μm (powder #5, Table 22) were higher in comparison when the feed volume was 50 and 100 mL, for which the yield was ≈ 56%, and the Dv50 of ≈ 3.0 and 2.6 μm, respectively (powders #3 and 4, Table 22). The lower Dv50 for 500 mL feed solution volume is due to the longer time required to spray dry a large volume, allowing smaller particles to escape into the filter. This hypothesis was confirmed by a lower Span, 1.7 for 500 mL, 2.1 and 1.9 for 50 and 100 mL, respectively (powders #3-5, Table 22), indicating a narrower distribution of the final powder.

In previous studies, ammonium bicarbonate has been proposed as a porogen [141], so it was added to the feed solution aiming at larger and more porous particles (powders #6 and 7, Table 17). However, adding ammonium bicarbonate did not produce larger particles as expected. Dv50 of the binary mixture was ≈ 3 μm (powders #6 and 7, Table 22), while the Dv50 of the powders obtained from pure leucine with 160 °C inlet temperature ranged from ≈ 2.6 and 3.5 μm (powders #3-5, Table 22). Consequently, the addition of ammonium bicarbonate was considered unnecessary in this study.

As a standard approach, lactose was tested (powders #8 and 9, Table 17), but there was no powder formation (powders #8 and 9, Table 22).

We did not further test this excipient because many studies reported that spray-dried lactose powders produced from solutions are mostly amorphous and particularly unstable when exposed to moisture [142,143]. A previous study showed that spray-dried lactose amorphous particles would transform to crystalline form when storage humidity was above 32% [144]. In addition, the prevalence of confirmed cases of lactose intolerance worldwide is currently about

57%, while the actual prevalence is estimated to exceed 65% [145]. Consequently, since some inhaled powder is ingested, lactose was discarded to obtain a pharmaceutical form suitable for as many patients as possible. In this regard, a previous study showed that lactose is present in various medications and amounts that may contribute to gastrointestinal symptoms [146].

Mannitol was tested with an inlet temperature of 120 and 160 °C (powders #10-13, Table 17). As said before, 120 °C inlet temperature (powders #10 and 12, Table 17) was not further tested due to possible moisture residue in the final powder. 160 °C inlet temperature was tested with two different solution feed rates, 9 and 12 mL/min (powders #11 and 13, Table 17). A solution feed rate of 9 mL/min led to particles with a Dv50 of ≈ 2.6 µm, of 12 mL/min to particles of ≈ 2.1 µm (powders #11 and 13, Table 22). In both cases, the particles' size was much smaller than 5 µm, so it was discarded. Mannitol was also tested in a binary mixture with leucine (powder #14, Table 17), leading to particles with a Dv50 of ≈ 3 µm (powder #14, Table 22), which are larger than those obtained with mannitol (≈ 2.1 µm, powder #13, Table 22) and leucine (≈ 2.6 µm, powder #4, Table 22) spray-dried alone with 160 °C inlet temperature and 100 mL feed solution volume. However, it was still too small for our purposes.

Leucine was also tested in a binary mixture with sodium hyaluronate (powder #15, Table 17) and led to particles with a Dv50 of ≈ 4 µm (powder #15, Table 22), which was the closest to the size we were looking for; therefore, this condition was chosen to produce spray-dried powders containing $25C_6$ NCs. Leucine is a suitable excipient because nanoparticles spray-dried from L-leucine yield microparticles with relevant characteristics for lung administration [147,148]. It is an anti-adherent excipient [149], and thanks to its surfactant-like properties [150], leucine can migrate to the surface of the microparticle during the rapid drying of the droplet in the last phase of the spray-drying process [151]. In other words, leucine acts as a dispersibility enhancer [147,152,153]. It should facilitate the disaggregation of nanoparticles in contact with an aqueous solution and generate powders with improved aerosolization properties [148].

4.4.2.7 Preparation of spray-dried powders with the active substance

After choosing powder #15 (Table 17) as the best for our purpose due to the Dv50 nearest to 5 μm (Table 22) among those produced, the concentrations of leucine and sodium hyaluronate in the feed solution were lowered to accommodate $25C_6$ NCs. In addition, sodium hyaluronate is an approved compound for inhalation, while leucine is widely used in inhalation formulations in clinical trials. The total solids concentration inside the feed solution was fixed at 4 g/L. NCs $25C_6$ was added, equal to 5 or 10% w/w. For this reason, to make $25C_6$ having a concentration of 5% w/w in the feed solution, leucine was lowered at 3.61 g/L and sodium hyaluronate at 0.19 g/L (powder #16, Table 17), while to make 10% w/w of $25C_6$, leucine was decreased at 3.42 g/L and sodium hyaluronate at 0.18 g/L (powder #17, Table 17). Table 23 shows the outlet temperatures, the yield of the processes, Dv50, and the Span of the obtained powders.

***Table 23**. Outlet temperature, yield, Dv50, and Span of spray-dried powders composed of POA-NCs and excipients.*

#	Outlet temperature (°C)	Yield (%)	Dv50 (μm)	Span
16	46	53	4.2 ± 0.1	2.1 ± 0.2
17	49	93	4.4 ± 0.1	1.9 ± 0.2

The powders containing $25C_6$ NCs comprised particles with a Dv50 ranging from ≈ 4.2 to 4.4 μm (powders #16 and 17, Table 23), larger than the powder spray-dried from excipients only, for which the Dv50 was ≈ 4 μm (powder #15, Table 22), although the size increase was not statistically significant. Moreover, when the concentration of $25C_6$ NCs increased from 5 to 10% w/w, Dv50 rose from 4.2 to 4.4 μm (powders #16 and 17, Table 23), and that was consistent with previously observed trends for which Dv50 increased with the addition of nanoparticles and as the concentration of nanoparticles increased [140,154,155]. The Span value was the same, ≈ 2, for powders with $25C_6$ NCs and for the powder spray-dried from excipients only (powder #15, Table 22, and powders #16 and 17, Table 23).

4.4.2.8 Powder disaggregation in simulated lung fluid

After the dissolution of the powder in SLF, the solution was analyzed with DLS. The particle size of $25C_6$ NCs was 153 ± 1 and 144 ± 8 nm (Table 24), proving that the spray drying process is capable of generating particles that, following disintegration in simulated pulmonary fluid, regenerated nanoparticles substantially similar to the starting ones (150 ± 2 nm, see Table 20). The PdI changed from 0.12 ± 0.1 (Table 20) to 0.54 ± 0.1 and 0.49 ± 0.1 (Table 24), showing an increase in the polydispersity, which suggests aggregation probably occurred during the spray-drying process as hypothesized by a previous study [154] or during redispersion. The zeta-potential passed from -67 ± 2 (Table 20) to -15 ± 5 and -29 ± 8 mV (Table 24), decreasing in absolute value, but remaining negative. This change in the zeta-potential caused the particles to repel each other less, which could further explain the observed increase in the PdI.

***Table 24**. Particle size, PdI, and zeta-potential of POA-NCs dispersion from powders #16 and 17 dissolved in SLF.*

#	Size (nm)	PdI	Zeta-potential (mV)
16	153 ± 1	0.54 ± 0.1	-15 ± 5
17	144 ± 8	0.49 ± 0.1	-29 ± 8

4.4.3 Conclusions

The third chapter of this thesis focused on the characterization and evaluation of different polymeric conjugates of pyrazinoic acid capable of originating biodegradable NCs, choosing the best in terms of stability and release of active ingredients to design a spray-dried powder of nanoconjugate-embedded microparticles as a novel strategy to allow the gradual intracellular enzymatic or hydrolytic release of active ingredients to alveolar macrophages.

Conjugates between pyrazinoic acid and poly (malic acid) previously synthesized proved to self-assemble, after simple nanoprecipitation in water, into nanometric, negatively surface-charged, spherical, and stable over time NCs. These NCs evidenced a sustained release of pyrazinoic acid and its esters, with higher amounts released from $25C_6$ NCs, who were therefore selected for the subsequent phases of this study.

$25C_6$ NCs proved to be degraded if exposed to esterase and lipase, which would reasonably happen also inside endo-lysosomes of alveolar macrophages due to the more acidic environment, rich in enzymes.

A potentially respirable spray-dried microparticle powder was designed to originate the studied nanoconjugates upon redispersion in aqueous media. The more promising empty microparticles are those spray-dried from leucine and sodium hyaluronate, which have suitable, micrometric dimensions for pulmonary administration. After loading the NCs, microparticles show slightly higher dimensions than empty ones, but they are still micrometric and appropriate for inhalation delivery. Finally, the drug-loaded microparticles after redispersion in SLF yield NCs with the same dimensions, a slightly less negative zeta-potential, and a higher PdI than the originally synthetized ones.

These results suggest that the developed, innovative platform appears extremely promising because it can maintain drug concentration over time, solving the common problem of burst release that affects nanosystems and reducing doses and frequency of administration with a lower chance of inducing side effects, improving TB therapy.

5 General conclusions

One of the aims of this doctoral thesis, i.e., the design of a platform suitable to be administered by inhalation that stimulates the immune response to prevent infectious diseases, was achieved by designing micrometric and sub-micrometric imiquimod powders. These powders, produced through spray drying and micronization, maintain the crystal structure of the raw material, conferring thermodynamical stability to the treated material, which in any future development could be an element of value to accelerate the process toward the final application.

Since imiquimod is an active ingredient with physicochemical characteristics highly unfavorable to its easy technological formulation, it was necessary to study its behavior in solution beforehand and in-depth, and this investigation revealed some interesting and peculiar anomalies, which were explained through the association between imiquimod molecules in solution. This phenomenon, which occurs mainly in very polar solvents, is at the basis of the marked tendency shown by IMQ to give rise to crystalline powders following the spray drying process, as demonstrated in the second chapter. In contrast, with other active ingredients, amorphous powders are often obtained. The aggregates in solution, in fact, can act as facilitators of the nucleation process, which is the basis of the formation of crystal.

The first research phase acquainted us with nanotechnologies applied to powders for highly advantageous inhalation administration. This allowed us to switch from developing a platform whose primary purpose was the achievement of broad-spectrum prevention of infectious diseases from their therapy. In particular, the goal was to develop a promising platform to improve the current treatment against tuberculosis, which to date is not without complications and numerous side effects. This last aim was pursued through the design of an inhalation powder that deposits in the lungs with the convenience of microparticles and with the persistence of nanosystems, originating innovative nanoconjugates that target alveolar macrophages and gradually release active ingredients, maintaining a constant concentration

of pyrazinoic acid and its ester, with the consequent and concrete possibility of reducing dosage, frequency of administration and therefore adverse effects.

6 References

1. David, C. V; Nguyen, H.; Goldenberg, G. Imiquimod: A Review of off-Label Clinical Applications. *J Drugs Dermatol* **2011**, *10*, 1300–1306.

2. Ghezzi, M.; Pescina, S.; Delledonne, A.; Ferraboschi, I.; Sissa, C.; Terenziani, F.; De Freitas Rosa Remiro, P.; Santi, P.; Nicoli, S. Improvement of Imiquimod Solubilization and Skin Retention via TPGS Micelles: Exploiting the Co-Solubilizing Effect of Oleic Acid. *Pharmaceutics* **2021**, *13*, 1476–1476, doi:10.3390/pharmaceutics13091476.

3. Arany, I.; Tyring, S.K.; Stanley, M.A.; Tomai, M.A.; Miller, R.L.; Smith, M.H.; Mcdermott, D.J.; Slade, H.B. Enhancement of the Innate and Cellular Immune Response in Patients with Genital Warts Treated with Topical Imiquimod Cream 5%. *Antiviral Res* **1999**, *43*, 55–63, doi:10.1016/s0166-3542(99)00033-9.

4. Hanna, E.; Abadi, R.; Abbas, O. Imiquimod in Dermatology: An Overview. *Int J Dermatol* **2016**, 831–844, doi:10.1111/ijd.13235.

5. Telò, I.; Pescina, S.; Padula, C.; Santi, P.; Nicoli, S. Mechanisms of Imiquimod Skin Penetration. *Int J Pharm* **2016**, *511*, 516–523, doi:10.1016/j.ijpharm.2016.07.043.

6. Chollet, J.L.; Jozwiakowski, M.J.; Phares, K.R.; Reiter, M.J.; Roddy, P.J.; Schultz, H.J.; Ta, Q. V.; Tomai, M.A. Development of a Topically Active Imiquimod Formulation. *Pharm Dev Technol* **1999**, *4*, 35–43, doi:10.1080/10837459908984222.

7. Lapteva, M.; Mignot, M.; Mondon, K.; Möller, M.; Gurny, R.; Kalia, Y.N. Self-Assembled MPEG-HexPLA Polymeric Nanocarriers for the Targeted Cutaneous Delivery of Imiquimod. *European Journal of Pharmaceutics and Biopharmaceutics* **2019**, *142*, 553–562, doi:10.1016/j.ejpb.2019.01.008.

8. Algahtani, M.S.; Ahmad, M.Z.; Nourein, I.H.; Ahmad, J. Co-Delivery of Imiquimod and Curcumin by Nanoemugel for Improved Topical Delivery and Reduced Psoriasis-Like Skin Lesions. *Biomolecules* **2020**, *10*, 968–968, doi:10.3390/biom10070968.

9. Pescina, S.; Garrastazu, G.; del Favero, E.; Rondelli, V.; Cantù, L.; Padula, C.; Santi, P.; Nicoli, S. Microemulsions Based on TPGS and Isostearic Acid for Imiquimod Formulation and Skin Delivery. *European Journal of Pharmaceutical Sciences* **2018**, *125*, 223–231, doi:10.1016/j.ejps.2018.10.007.

10. Panoutsopoulou, E.; Zbytovská, J.; Vávrová, K.; Paraskevopoulos, G. Phospholipid-Based Microemulsions for Cutaneous Imiquimod Delivery. *Pharmaceuticals* **2022**, *515*, 15, doi:10.3390/ph15050515.

11. Kim, S.; Abdella, S.; Abid, F.; Afinjuomo, F.; Youssef, S.H.; Holmes, A.; Song, Y.; Vaidya, S.; Garg, S. Development and Optimization of Imiquimod-Loaded Nanostructured Lipid Carriers Using a Hybrid Design of Experiments Approach. *Int J Nanomedicine* **2023**, *18*, 1007–1029, doi:10.2147/IJN.S400610.

12. Avdeef, A.; Fuguet, E.; Llinàs, A.; Ràfols, C.; Bosch, E.; Völgyi, G.; Verbic, T.; Boldyreva, E.; Takács-Novák, K. Equilibrium Solubility Measurement of Ionizable Drugs - Consensus Recommendations for Improving Data Quality. *ADMET DMPK* **2016**, *4*, 117–178, doi:10.5599/admet.4.2.292.

13. Sinko, P.J.; Martin, A.N. *Martin's Physical Pharmacy and Pharmaceutical Sciences: Physical Chemical and Biopharmaceutical Principles in the Pharmaceutical Sciences*; David Troy, Ed.; 5th ed.; Lippincott Williams & Wilkins: Philadelphia, 2006;

14. Kalam, M.A.; Alshamsan, A.; Alkholief, M.; Alsarra, I.A.; Ali, R.; Haq, N.; Anwer, M.K.; Shakeel, F. Solubility Measurement and Various Solubility Parameters of Glipizide in Different Neat Solvents. *ACS Omega* **2020**, *5*, 1708–1716, doi:10.1021/acsomega.9b04004.

15. Sinko, P.J.; Martin, A.N. *Martin's Physical Pharmacy and Pharmaceutical Sciences: Physical Chemical and Biopharmaceutical Principles in the Pharmaceutical Sciences*; David Troy, Ed.; 5th ed.; Lippincott Williams & Wilkins: Philadelphia, 2006;

16. Hussain, S.; Shaikh, T.; Farooqui, M. Development and Validation of Liquid Chromatography Method for the Determination and Quantification of Impurities in Imiquimod. *Br J Pharm Res* **2016**, *13*, 1–9, doi:10.9734/bjpr/2016/28020.

17. Balireddi, V.; Tirukkovalluri, S.R.; Murthy Tatikonda, K.; Surikutchi, B.T.; Mitra, P. Development and Validation of Stability Indicating UPLC-PDA/MS for the Determination of Imiquimod and Its Eight Related Substances: Application to Topical Cream. *J Chromatogr Sci* **2019**, *57*, 249–257, doi:10.1093/chromsci/bmy108.

18. Vay, K.; Scheler, S.; Frieß, W. Application of Hansen Solubility Parameters for Understanding and Prediction of Drug Distribution in Microspheres. *Int J Pharm* **2011**, *416*, 202–209, doi:10.1016/j.ijpharm.2011.06.047.

19. Fedors, R.F. A Method for Estimating Both the Solubility Parameters and Molar Volumes of Liquids. *Polym Eng Sci* **1974**, *14*, 147–154, doi:10.1002/pen.760140211.

20. Zhao, B.; Rong, Y.Z.; Huang, X.H.; Shen, J.S. Experimental and Theoretical Study on the Structure and Electronic Spectra of Imiquimod and Its Synthetic Intermediates. *Bioorg Med Chem Lett* **2007**, *17*, 4942–4946, doi:10.1016/j.bmcl.2007.06.020.

21. Karachevtsev, V.A.; Plokhotnichenko, A.M.; Karachevtsev, M. V.; Leontiev, V.S. Decrease of Carbon Nanotube UV Light Absorption Induced by π-π-Stacking Interaction with Nucleotide Bases. *Carbon N Y* **2010**, *48*, 3682–3691, doi:10.1016/j.carbon.2010.06.009.

22. D'Abramo, M.; Castellazzi, C.L.; Orozco, M.; Amadei, A. On the Nature of DNA Hyperchromic Effect. *Journal of Physical Chemistry B* **2013**, *117*, 8697–8704, doi:10.1021/jp403369k.

23. Li, C.P.; Du, M. Role of Solvents in Coordination Supramolecular Systems. *Chemical Communications* **2011**, *47*, 5958–5972, doi:10.1039/c1cc10935a.

24. Layek, B.; Rahman Nirzhor, S.S.; Rathi, S.; Kandimalla, K.K.; Wiedmann, T.S.; Prabha, S. Design, Development, and Characterization of Imiquimod-Loaded Chitosan Films for Topical Delivery. *AAPS PharmSciTech* **2019**, *20*, 58, doi:10.1208/s12249-018-1288-5.

25. Takkella, D.; Sharma, S.; Martinez-Fernandez, L.; Gavvala, K. Excited-State Dynamics of Imiquimod in Aqueous Solutions. *J Photochem Photobiol A Chem* **2022**, *431*, doi:10.1016/j.jphotochem.2022.113998.

26. Hunter, C.A. Quantifying Intermolecular Interactions: Guidelines for the Molecular Recognition Toolbox. *Angewandte Chemie - International Edition* **2004**, *43*, 5310–5324, doi:10.1002/anie.200301739.

27. Beutler, B. Innate Immunity: An Overview. *Mol Immunol* **2004**, *40*, 845–859, doi:10.1016/j.molimm.2003.10.005.

28. Poltorak, A.; Smirnova, I.; He, X.; Liu, M.-Y.; Huffel, C. Van; Birdwell, D.; Alejos, E.; Silva, M.; Du, X.; Thompson, P.; et al. Genetic and Physical Mapping of the Lps Locus: Identification of the Toll-4 Receptor as a Candidate Gene in the Critical Region. *Blood Cells Mol Dis* **1998**, *240*, 340–355.

29. Poltorak, A.; He, X.; Smirnova, I.; Liu, M.-Y.; Van Huffel, C.; Du, X.; Birdwell, D.; Alejos, E.; Silva, M.G.; Chris Freudenberg, M.; et al. Defective LPS Signaling in C3H/HeJ and C57BL/10ScCr Mice: Mutations in Tlr4 Gene. *Science (1979)* **1998**, *282*, 2085–2088.

30. Singh, P.K.; Parsek, M.R.; Peter Greenberg, E.; Welsh, M.J.; Keck, W.M. A Component of Innate Immunity Prevents Bacterial Biofilm Development. *Nature* **2002**, *417*, 552–555.

31. Condie, R.M.; Zak, S.J.; Good, R.A. Effect of Meningococcal Endotoxin on the Immune Response. *Proceedings of the Society for Experimental Biology and Medicine* **1955**, *90*, 355–369, doi:10.3181/00379727-90-22032.

32. Bartlett, J.A.; Fischer, A.J.; Mccray, P.B. Innate Immune Functions of the Airway Epithelium The Strategic Position of the Airway Epithelium. *Contrib Microbiol. Basel, Karger* **2008**, *15*, 147–163.

33. Bourhis, L. Le; Werts, C. Role of Nods in Bacterial Infection. *Microbes Infect* **2007**, *9*, 629–636, doi:10.1016/j.micinf.2007.01.014.

34. Shi, S.; Zhu, H.; Xia, X.; Liang, Z.; Ma, X.; Sun, B. Vaccine Adjuvants: Understanding the Structure and Mechanism of Adjuvanticity. *Vaccine* **2019**, *37*, 3167–3178, doi:10.1016/j.vaccine.2019.04.055.

35. Glenny A. T. INSOLUBLE PRECIPITATES IN DIPHTHERIA AND TETANUS IMMUNIZATION. *Br Med J* **1930**, *2*, 244–245.

36. Sun, B.; Xia, T. Nanomaterial-Based Vaccine Adjuvants. *J Mater Chem B* **2016**, *4*, 5496–5509, doi:10.1039/c6tb01131d.

37. Https://Pulmotect.Com/Science/ (Visited on 13th December 2023).

38. Bekkering, S.; Domínguez-Andrés, J.; Joosten, L.A.B.; Riksen, N.P.; Netea, M.G. Trained Immunity: Reprogramming Innate Immunity in Health and Disease Keywords. *Annual Review of Immunology* **2021**, *39*, 667–693, doi:10.1146/annurev-immunol-102119.

39. *Pulmotect Reports Positive Topline Results from Randomized, Placebo Controlled Phase-2 Trial of PUL-042 against COVID-19*; 2021;

40. To, E.E.; Erlich, J.; Liong, F.; Luong, R.; Liong, S.; Bozinovski, S.; Seow, H.J.; O'Leary, J.J.; Brooks, D.A.; Vlahos, R.; et al. Intranasal and Epicutaneous Administration of Toll-

like Receptor 7 (TLR7) Agonists Provides Protection against Influenza A Virus-Induced Morbidity in Mice. *Sci Rep* **2019**, *9*, doi:10.1038/s41598-019-38864-5.

41. Salinas, F.M.; Nebreda, A.D.; Vázquez, L.; Gentilini, M.V.; Marini, V.; Benedetti, M.; Nabaes Jodar, M.S.; Viegas, M.; Shayo, C.; Bueno, C.A. Imiquimod Suppresses Respiratory Syncytial Virus (RSV) Replication via PKA Pathway and Reduces RSV Induced-Inflammation and Viral Load in Mice Lungs. *Antiviral Res* **2020**, *179*, doi:10.1016/j.antiviral.2020.104817.

42. Angelopoulou, A.; Alexandris, N.; Konstantinou, E.; Mesiakaris, K.; Zanidis, C.; Farsalinos, K.; Poulas, K. Imiquimod - A Toll like Receptor 7 Agonist - Is an Ideal Option for Management of COVID 19. *Environ Res* **2020**, *188*, doi:10.1016/j.envres.2020.109858.

43. Kirtland, M.E.; Tsitoura, D.C.; Durham, S.R.; Shamji, M.H. Toll-Like Receptor Agonists as Adjuvants for Allergen Immunotherapy. *Front Immunol* **2020**, *11*, doi:10.3389/fimmu.2020.599083.

44. Ekman, A.K.; Adner, M.; Cardell, L.O. Toll-like Receptor 7 Activation Reduces the Contractile Response of Airway Smooth Muscle. *Eur J Pharmacol* **2011**, *652*, 145–151, doi:10.1016/j.ejphar.2010.11.009.

45. Drake, M.G.; Scott, G.D.; Proskocil, B.J.; Fryer, A.D.; Jacoby, D.B.; Kaufman, E.H. Toll-like Receptor 7 Rapidly Relaxes Human Airways. *Am J Respir Crit Care Med* **2013**, *188*, 664–672, doi:10.1164/rccm.201303-0442OC.

46. Vicente, S.; Peleteiro, M.; Díaz-Freitas, B.; Sanchez, A.; González-Fernández, Á.; Alonso, M.J. Co-Delivery of Viral Proteins and a TLR7 Agonist from Polysaccharide Nanocapsules: A Needle-Free Vaccination Strategy. *Journal of Controlled Release* **2013**, *172*, 773–781, doi:10.1016/j.jconrel.2013.09.012.

47. Stein, S.W.; Thiel, C.G. The History of Therapeutic Aerosols: A Chronological Review. *J Aerosol Med Pulm Drug Deliv* **2017**, *30*, 20–41, doi:10.1089/jamp.2016.1297.

48. Newman, S.P. Drug Delivery to the Lungs: Challenges and Opportunities. *Ther Deliv* **2017**, *8*, 647–661, doi:10.4155/tde-2017-0037.

49. Hoppentocht, M.; Hagedoorn, P.; Frijlink, H.W.; de Boer, A.H. Technological and Practical Challenges of Dry Powder Inhalers and Formulations. *Adv Drug Deliv Rev* **2014**, *75*, 18–31, doi:10.1016/j.addr.2014.04.004.

50. Labiris, N.R.; Dolovich, M.B. Pulmonary Drug Delivery. Part I: Physiological Factors Affecting Therapeutic Effectiveness of Aerosolized Medications. *Br J Clin Pharmacol* **2003**, *56*, 588–599, doi:10.1046/j.1365-2125.2003.01892.x.

51. Santos Cavaiola, T.; Edelman, S. Inhaled Insulin: A Breath of Fresh Air? A Review of Inhaled Insulin. *Clin Ther* **2014**, *36*, 1275–1289, doi:10.1016/j.clinthera.2014.06.025.

52. Ewald R. Weibel *Morphometry of the Human Lung*; 1st ed.; Springer Berlin, Heidelberg: New York, 1963;

53. Frijlink, H.W.; De Boer, A.H. Dry Powder Inhalers for Pulmonary Drug Delivery. *Expert Opin Drug Deliv* **2004**, *1*, 67–86, doi:10.1517/17425247.1.1.67.

54. Patton, J.S.; Byron, P.R. Inhaling Medicines: Delivering Drugs to the Body through the Lungs. *Nat Rev Drug Discov* **2007**, *6*, 67–74, doi:10.1038/nrd2153.

55. Patwa, A.; Shah, A. Anatomy and Physiology of Respiratory System Relevant to Anaesthesia. *Indian J Anaesth* **2015**, *59*, 533–541, doi:10.4103/0019-5049.165849.

56. Darquenne, C. Deposition Mechanisms. *J Aerosol Med Pulm Drug Deliv* **2020**, *33*, 181–185, doi:10.1089/jamp.2020.29029.cd.

57. Darquenne, C. Aerosol Deposition in Health and Disease. *J Aerosol Med Pulm Drug Deliv* **2012**, *25*, 140–147, doi:10.1089/jamp.2011.0916.

58. Telko, M.J.; Hickey, A.J. Dry Powder Inhaler Formulation. *Respir Care* **2005**, *50*, 1209–1227.

59. Edwards, D.A.; Hanes, J.; Caponetti, G.; Hrkach, J.; Ben-Jebria, A.; Eskew, M. Lou; Mintzes, J.; Deaver, D.; Lotan, N.; Langer, R. Large Porous Particles for Pulmonary Drug Delivery. *Science (1979)* **1997**, *276*, 1868–1871, doi:10.1126/science.276.5320.1868.

60. *Chapter <467>: RESIDUAL SOLVENTS*; United States Pharmacopeial Convention: Rockville, 2023;

61. Rowe, R.C.; Sheskey, P.J.; Quinn, M.E. *Handbook of Pharmaceutical Excipients*; 6th ed.; Pharmaceutical Press and American Pharmacists Association, 2009;

62. Ferreira da Silva, L.; Silva Eustacio, R. da; Fraguas Neto, M.R.; de Souza Silva, C.; Mendes, M.F.; Siqueira Pereira, C. de S. Simulation of the Extractive Distillation Process of Ethanol-Water- Propylene Glycol System. *Journal of Thermodynamics & Catalysis* **2017**, *08*, doi:10.4172/2157-7544.1000191.

63. Kahlbaum G.W.A., von Wirkner C.G.: Hälfte (Vol. 2a). Monograph (1897) 1-222.

64. Kemp, I.C.; Wadley, R.; Hartwig, T.; Cocchini, U.; See-Toh, Y.; Gorringe, L.; Fordham, K.; Ricard, F. Experimental Study of Spray Drying and Atomization with a Two-Fluid Nozzle to Produce Inhalable Particles. *Drying Technology* **2013**, *31*, 930–941, doi:10.1080/07373937.2012.710693.

65. Nath, S.; Satpathy, G.R. A Systematic Approach for Investigation of Spray Drying Processes. *Drying Technology* **1998**, *16*, 1173–1193, doi:10.1080/07373939808917459.

66. EUROPEAN PHARMACOPOEIA 10.2. In.

67. Reagan-Shaw, S.; Nihal, M.; Ahmad, N. Dose Translation from Animal to Human Studies Revisited. *The FASEB Journal* **2008**, *22*, 659–661, doi:10.1096/fj.07-9574lsf.

68. MacDonald, C.; Lyzenga, W.; Shao, D.; Agu, R.U. Water-Soluble Organic Solubilizers for in Vitro Drug Delivery Studies with Respiratory Epithelial Cells: Selection Based on Various Toxicity Indicators. *Drug Deliv* **2010**, *17*, 434–442, doi:10.3109/10717541003777548.

69. Sorgi, D.; Sartori, A.; Germani, S.; Gentile, R.N.; Bianchera, A.; Bettini, R. Imiquimod Solubility in Different Solvents: An Interpretative Approach. *Pharmaceutics* **2024**, *16*, 282, doi:10.3390/pharmaceutics16020282.

70. International Organization for Standardization ISO 10993-5:2009. Biological Evaluation of Medical Devices-Part 5: Tests for in Vitro Cytotoxicity 2009.

71. Ong, H.X.; Traini, D.; Young, P.M. Pharmaceutical Applications of the Calu-3 Lung Epithelia Cell Line. *Expert Opin Drug Deliv* **2013**, *10*, 1287–1302, doi:10.1517/17425247.2013.805743.

72. Tanaka, T.; Narazaki, M.; Kishimoto, T. IL-6 in Inflammation, Immunity, and Disease. *Cold Spring Harb Perspect Biol* **2014**, *6*, doi:10.1101/cshperspect.a016295.

73. Vilotić, A.; Nacka-Aleksić, M.; Pirković, A.; Bojić-Trbojević, Ž.; Dekanski, D.; Jovanović Krivokuća, M. IL-6 and IL-8: An Overview of Their Roles in Healthy and Pathological Pregnancies. *Int J Mol Sci* **2022**, *23*, doi:10.3390/ijms232314574.

74. Tan, A.C.L.; Mifsud, E.J.; Zeng, W.; Edenborough, K.; McVernon, J.; Brown, L.E.; Jackson, D.C. Intranasal Administration of the TLR2 Agonist Pam2Cys Provides Rapid Protection against Influenza in Mice. *Mol Pharm* **2012**, *9*, 2710–2718, doi:10.1021/mp300257x.

75. World Health Organization *Global Tuberculosis Report 2022*; 2022;

76. Kanabalan, R.D.; Lee, L.J.; Lee, T.Y.; Chong, P.P.; Hassan, L.; Ismail, R.; Chin, V.K. Human Tuberculosis and Mycobacterium Tuberculosis Complex: A Review on Genetic Diversity, Pathogenesis and Omics Approaches in Host Biomarkers Discovery. *Microbiol Res* **2021**, *246*, 126674, doi:10.1016/j.micres.2020.126674.

77. Acharya, B.; Acharya, A.; Gautam, S.; Ghimire, S.P.; Mishra, G.; Parajuli, N.; Sapkota, B. Advances in Diagnosis of Tuberculosis: An Update into Molecular Diagnosis of Mycobacterium Tuberculosis. *Mol Biol Rep* **2020**, *47*, 4065–4075, doi:10.1007/s11033-020-05413-7.

78. Ahmad, S. Pathogenesis, Immunology, and Diagnosis of Latent Mycobacterium Tuberculosis Infection. *Clin Dev Immunol* **2010**, *2011*, 1–17, doi:10.1155/2011/814943.

79. Dannenberg Jr., A.M. Immune Mechanisms in the Pathogenesis of Pulmonary Tuberculosis. *Rev Infect Dis* **1989**, *11*, S369–S378, doi:10.1093/clinids/11.supplement_2.s369.

80. de Martino, M.; Lodi, L.; Galli, L.; Chiappini, E. Immune Response to Mycobacterium Tuberculosis: A Narrative Review. *Front Pediatr* **2019**, *7*, 350, doi:10.3389/fped.2019.00350.

81. Palucci, I.; Delogu, G. Host Directed Therapies for Tuberculosis: Futures Strategies for an Ancient Disease. *Chemotherapy* **2018**, *63*, 172–180, doi:10.1159/000490478.

82. Kiran, D.; Podell, B.K.; Chambers, M.; Basaraba, R.J. Host-Directed Therapy Targeting the Mycobacterium Tuberculosis Granuloma: A Review. *Semin Immunopathol* **2016**, *38*, 167–183, doi:10.1007/s00281-015-0537-x.

83. Barry, C.E.; Boshoff, H.I.; Dartois, V.; Dick, T.; Ehrt, S.; Flynn, J.A.; Schnappinger, D.; Wilkinson, R.J.; Young, D. The Spectrum of Latent Tuberculosis: Rethinking the Biology and Intervention Strategies. *Nat Rev Microbiol* **2009**, *7*, 845–855, doi:10.1038/nrmicro2236.

84. Martinot, A.J. Microbial Offense vs Host Defense: Who Controls the TB Granuloma? *Vet Pathol* **2018**, *55*, 14–26, doi:10.1177/0300985817705177.

85. Braunstein, M.; Hickey, A.J.; Ekins, S. Why Wait? The Case for Treating Tuberculosis with Inhaled Drugs. *Pharm Res* **2019**, *36*, 166, doi:10.1007/s11095-019-2704-6.

86. Lenaerts, A.; Barry, C.E.; Dartois, V. Heterogeneity in Tuberculosis Pathology, Microenvironments and Therapeutic Responses. *Immunol Rev* **2015**, *264*, 288–307, doi:10.1111/imr.12252.

87. Pande, T.; Cohen, C.; Pai, M.; Ahmad Khan, F. Computer-Aided Detection of Pulmonary Tuberculosis on Digital Chest Radiographs: A Systematic Review. *International Journal of Tuberculosis and Lung Disease* **2016**, *20*, 1226–1230, doi:10.5588/ijtld.15.0926.

88. Furin, J.; Cox, H.; Pai, M. Tuberculosis. *The Lancet* **2019**, *393*, 1642–1656, doi:10.1016/S0140-6736(19)30308-3.

89. Pai, M.; Denkinger, C.M.; Kik, S. V.; Rangaka, M.X.; Zwerling, A.; Oxlade, O.; Metcalfe, J.Z.; Cattamanchi, A.; Dowdy, D.W.; Dheda, K.; et al. Gamma Interferon Release Assays for Detection of Mycobacterium Tuberculosis Infection. *Clin Microbiol Rev* **2014**, *27*, 3–20, doi:10.1128/CMR.00034-13.

90. Kohli, M.; Schiller, I.; Dendukuri, N.; Yao, M.; Dheda, K.; Denkinger, C.M.; Schumacher, S.G.; Steingart, K.R. Xpert MTB/RIF Ultra and Xpert MTB/RIF Assays for Extrapulmonary Tuberculosis and Rifampicin Resistance in Adults. *Cochrane Database of Systematic Reviews* **2021**, *1*, CD012768, doi:10.1002/14651858.CD012768.pub3.

91. Seki, M.; Kim, C.K.; Hayakawa, S.; Mitarai, S. Recent Advances in Tuberculosis Diagnostics in Resource-Limited Settings. *European Journal of Clinical Microbiology and Infectious Diseases* **2018**, *37*, 1405–1410, doi:10.1007/s10096-018-3258-y.

92. Singh, B.K.; Sharma, S.K.; Sharma, R.; Sreenivas, V.; Myneedu, V.P.; Kohli, M.; Bhasin, D.; Sarin, S. Diagnostic Utility of a Line Probe Assay for Multidrug Resistant-TB in Smear-Negative Pulmonary Tuberculosis. *PLoS One* **2017**, *12*, e0182988, doi:10.1371/journal.pone.0182988.

93. Satta, G.; Lipman, M.; Smith, G.P.; Arnold, C.; Kon, O.M.; McHugh, T.D. Mycobacterium Tuberculosis and Whole-Genome Sequencing: How Close Are We to Unleashing Its Full Potential? *Clinical Microbiology and Infection* **2018**, *24*, 604–609, doi:10.1016/j.cmi.2017.10.030.

94. Zumla, A.; Nahid, P.; Cole, S.T. Advances in the Development of New Tuberculosis Drugs and Treatment Regimens. *Nat Rev Drug Discov* **2013**, *12*, 388–404, doi:10.1038/nrd4001.

95. Alsayed, S.S.R.; Gunosewoyo, H. Tuberculosis: Pathogenesis, Current Treatment Regimens and New Drug Targets. *Int J Mol Sci* **2023**, *24*, 5202, doi:10.3390/ijms24065202.

96. Castro, A.T. e.; Mendes, M.; Freitas, S.; Roxo, P.C. Incidence and Risk Factors of Major Toxicity Associated to First-Line Antituberculosis Drugs for Latent and Active Tuberculosis during a Period of 10 Years. *Revista Portuguesa de Pneumologia* **2015**, *21*, 144–150, doi:10.1016/j.rppnen.2014.08.004.

97. Yee, D.; Valiquette, C.; Pelletier, M.; Parisien, I.; Rocher, I.; Menzies, D. Incidence of Serious Side Effects from First-Line Antituberculosis Drugs among Patients Treated for Active Tuberculosis. *Am J Respir Crit Care Med* **2003**, *167*, 1472–1477, doi:10.1164/rccm.200206-626OC.

98. Forget, E.J.; Menzies, D. Adverse Reactions to First-Time Antituberculosis Drugs. *Expert Opin Drug Saf* **2006**, *5*, 231–249, doi:10.1517/14740338.5.2.231.

99. Strydom, N.; Gupta, S. V.; Fox, W.S.; Via, L.E.; Bang, H.; Lee, M.; Eum, S.; Shim, T.S.; Barry, C.E.; Zimmerman, M.; et al. Tuberculosis Drugs' Distribution and Emergence of Resistance in Patient's Lung Lesions: A Mechanistic Model and Tool for Regimen and Dose Optimization. *PLoS Med* **2019**, *16*, e1002773, doi:10.1371/journal.pmed.1002773.

100. Chiang, C.Y.; Centis, R.; Migliori, G.B. Drug-Resistant Tuberculosis: Past, Present, Future. *Respirology* **2010**, *15*, 413–432, doi:10.1111/j.1440-1843.2010.01738.x.

101. Chien, J.Y.; Chen, Y.T.; Wu, S.G.; Lee, J.J.; Wang, J.Y.; Yu, C.J. Treatment Outcome of Patients with Isoniazid Mono-Resistant Tuberculosis. *Clinical Microbiology and Infection* **2015**, *21*, 59–68, doi:10.1016/j.cmi.2014.08.008.

102. Malenfant, J.H.; Brewer, T.F. Rifampicin Mono-Resistant Tuberculosis - A Review of an Uncommon but Growing Challenge for Global Tuberculosis Control. *Open Forum Infect Dis* **2021**, *8*, doi:10.1093/ofid/ofab018.

103. Martín-García, M.; Esteban, J. Evaluating Bedaquiline as a Treatment Option for Multidrug-Resistant Tuberculosis. *Expert Opin Pharmacother* **2021**, *22*, 535–541, doi:10.1080/14656566.2020.1867538.

104. Liu, Y.; Matsumoto, M.; Ishida, H.; Ohguro, K.; Yoshitake, M.; Gupta, R.; Geiter, L.; Hafkin, J. Delamanid: From Discovery to Its Use for Pulmonary Multidrug-Resistant Tuberculosis (MDR-TB). *Tuberculosis* **2018**, *111*, 20–30, doi:10.1016/j.tube.2018.04.008.

105. Thwaites, G.; Nguyen, N. V. Linezolid for Drug-Resistant Tuberculosis. *New England Journal of Medicine* **2022**, *387*, 842–843, doi:10.1056/nejme2208554.

106. Mirnejad, R.; Asadi, A.; Khoshnood, S.; Mirzaei, H.; Heidary, M.; Fattorini, L.; Ghodousi, A.; Darban-Sarokhalil, D. Clofazimine: A Useful Antibiotic for Drug-Resistant Tuberculosis. *Biomedicine and Pharmacotherapy* **2018**, *105*, 1353–1359, doi:10.1016/j.biopha.2018.06.023.

107. Dalcolmo, M.; Gayoso, R.; Sotgiu, G.; D'Ambrosio, L.; Rocha, J.L.; Borga, L.; Fandinho, F.; Braga, J.U.; Galesi, V.M.N.; Barreira, D.; et al. Effectiveness and Safety of Clofazimine in Multidrug-Resistant Tuberculosis: A Nationwide Report from Brazil. *European Respiratory Journal* **2017**, *49*, 1602445, doi:10.1183/13993003.02445-2016.

108. Falk, J.A.; Minai, O.A.; Mosenifar, Z. Inhaled and Systemic Corticosteroids in Chronic Obstructive Pulmonary Disease. *Proc Am Thorac Soc* **2008**, *5*, 506–512, doi:10.1513/pats.200707-096ET.

109. Thomas, B.; Pugalenthi, A. Currently Available Inhaled Therapies in Asthma and Advances in Drug Delivery and Devices. *Indian J Pediatr* **2022**, *89*, 387–394, doi:10.1007/s12098-021-03976-2.

110. Littlewood, K.J.; Higashi, K.; Jansen, J.P.; Capkun-Niggli, G.; Balp, M.M.; Doering, G.; Tiddens, H.A.W.M.; Angyalosi, G. A Network Meta-Analysis of the Efficacy of Inhaled Antibiotics for Chronic Pseudomonas Infections in Cystic Fibrosis. *Journal of Cystic Fibrosis* **2012**, *11*, 419–426, doi:10.1016/j.jcf.2012.03.010.

111. Rossi, I.; Buttini, F.; Sonvico, F.; Affaticati, F.; Martinelli, F.; Annunziato, G.; Machado, D.; Viveiros, M.; Pieroni, M.; Bettini, R. Sodium Hyaluronate Nanocomposite Respirable Microparticles to Tackle Antibiotic Resistance with Potential Application in Treatment of Mycobacterial Pulmonary Infections. *Pharmaceutics* **2019**, *11*, doi:10.3390/pharmaceutics11050203.

112. Giovagnoli, S.; Schoubben, A.; Ricci, M. The Long and Winding Road to Inhaled TB Therapy: Not Only the Bug's Fault. *Drug Dev Ind Pharm* **2017**, *43*, 347–363, doi:10.1080/03639045.2016.1272119.

113. Hickey, A.J.; Durham, P.G.; Dharmadhikari, A.; Nardell, E.A. Inhaled Drug Treatment for Tuberculosis: Past Progress and Future Prospects. *Journal of Controlled Release* **2016**, *240*, 127–134, doi:10.1016/j.jconrel.2015.11.018.

114. Pham, D.D.; Fattal, E.; Tsapis, N. Pulmonary Drug Delivery Systems for Tuberculosis Treatment. *Int J Pharm* **2015**, *478*, 517–529, doi:10.1016/j.ijpharm.2014.12.009.

115. Lamont, E.A.; Dillon, N.A.; Baughn, A.D. The Bewildering Antitubercular Action of Pyrazinamide. *Microbiology and Molecular Biology Reviews* **2020**, *84*, e00070-19, doi:10.1128/MMBR.

116. Zhang, Y.; Wade, M.M.; Scorpio, A.; Zhang, H.; Sun, Z. Mode of Action of Pyrazinamide: Disruption of Mycobacterium Tuberculosis Membrane Transport and Energetics by Pyrazinoic Acid. *Journal of Antimicrobial Chemotherapy* **2003**, *52*, 790–795, doi:10.1093/jac/dkg446.

117. Prideaux, B.; Via, L.E.; Zimmerman, M.D.; Eum, S.; Sarathy, J.; O'Brien, P.; Chen, C.; Kaya, F.; Weiner, D.M.; Chen, P.Y.; et al. The Association between Sterilizing Activity and Drug Distribution into Tuberculosis Lesions. *Nat Med* **2015**, *21*, 1223–1227, doi:10.1038/nm.3937.

118. Pham, D.D.; Grégoire, N.; Couet, W.; Gueutin, C.; Fattal, E.; Tsapis, N. Pulmonary Delivery of Pyrazinamide-Loaded Large Porous Particles. *European Journal of Pharmaceutics and Biopharmaceutics* **2015**, *94*, 241–250, doi:10.1016/j.ejpb.2015.05.021.

119. Fernandes, J.P. dos S.; Pavan, F.R.; Leite, C.Q.F.; Felli, V.M.A. Synthesis and Evaluation of a Pyrazinoic Acid Prodrug in Mycobacterium Tuberculosis. *Saudi Pharmaceutical Journal* **2014**, *22*, 376–380, doi:10.1016/j.jsps.2013.12.005.

120. Mahmood, N.; Bhatti, S.; Abbas, S.N.; Shahid, S.; Nasir, S.B. The PncA Gene Mutations of Mycobacterium Tuberculosis in Multidrug-Resistant Tuberculosis. *Biotechnol Appl Biochem* **2022**, *69*, 2195–2204, doi:10.1002/bab.2278.

121. Cynamon, M.H.; Klemens, S.P.; Chou, T.-S.; Gimi, R.H.; Welch, J.T. Antimycobacterial Activity of a Series of Pyrazinoic Acid Esters. *J. Med. Chem* **1992**, *35*, 1212–1215, doi:10.1021/jm00085a007.

122. Simões, M.F.; Valente, E.; Gómez, M.J.R.; Anes, E.; Constantino, L. Lipophilic Pyrazinoic Acid Amide and Ester Prodrugs. Stability, Activation and Activity against M. Tuberculosis. *European Journal of Pharmaceutical Sciences* **2009**, *37*, 257–263, doi:10.1016/j.ejps.2009.02.012.

123. Pham, D.D.; Fattal, E.; Tsapis, N. Pyrazinamide-Loaded Poly(Lactide-Co-Glycolide) Nanoparticles: Optimization by Experimental Design. *J Drug Deliv Sci Technol* **2015**, *30*, 384–390, doi:10.1016/j.jddst.2015.07.006.

124. Usharani, N.; Kanth, S.V.; Saravanan, N. Current Nanotechnological Strategies Using Lipids, Carbohydrates, Proteins and Metal Conjugates-Based Carrier Systems for Diagnosis and Treatment of Tuberculosis — A Review. *Int J Biol Macromol* **2023**, *227*, 262–272, doi:10.1016/j.ijbiomac.2022.12.087.

125. Gómez-Gaete, C.; Tsapis, N.; Besnard, M.; Bochot, A.; Fattal, E. Encapsulation of Dexamethasone into Biodegradable Polymeric Nanoparticles. *Int J Pharm* **2007**, *331*, 153–159, doi:10.1016/j.ijpharm.2006.11.028.

126. Abioye, A.O.; Chi, G.T.; Kola-Mustapha, A.T.; Ruparelia, K.; Beresford, K.; Arroo, R. Polymer-Drug Nanoconjugate-An Innovative Nanomedicine: Challenges and Recent Advancements in Rational Formulation Design for Effective Delivery of Poorly Soluble Drugs. *Pharm Nanotechnol* **2016**, *4*, 38–79, doi:10.2174/2211738504666160213001714.

127. Ljubimova, J.Y.; Fujita, M.; Ljubimov, A. V.; Torchilin, V.P.; Black, K.L.; Holler, E. Poly(Malic Acid) Nanoconjugates Containing Various Antibodies and Oligonucleotides for Multitargeting Drug Delivery. *Nanomedicine* **2008**, *3*, 247–265, doi:10.2217/17435889.3.2.247.

128. Loyer, P.; Cammas-Marion, S. Natural and Synthetic Poly(Malic Acid)-Based Derivates: A Family of Versatile Biopolymers for the Design of Drug Nanocarriers. *J Drug Target* **2014**, *22*, 556–575, doi:10.3109/1061186X.2014.936871.

129. Marques, M.R.C.; Loebenberg, R.; Almukainzi, M. Simulated Biological Fluids with Possible Application in Dissolution Testing. *Dissolut Technol* **2011**, *18*, 15–28, doi:10.14227/DT180311P15.

130. Fessi, H.; Puisieux, F.; Devissaguet, J.P.; Ammoury, N.; Benita, S. Nanocapsule Formation by Interfacial Polymer Deposition Following Solvent Displacement. *Int J Pharm* **1989**, *55*, R1–R4, doi:10.1016/0378-5173(89)90281-0.

131. Yin, F.P.; Cao, Y.; Zhu, Y.; Judeh, Z.M.A.; Chan-Park, M.B. Addition of β-Malic Acid-Containing Poly(Ethylene Glycol) Dimethacrylate to Form Biodegradable and Biocompatible Hydrogels. *Biomacromolecules* **2009**, *10*, 2043–2052, doi:10.1021/bm801367n.

132. Yang, W.; Peters, J.I.; Williams, R.O. Inhaled Nanoparticles-A Current Review. *Int J Pharm* **2008**, *356*, 239–247, doi:10.1016/j.ijpharm.2008.02.011.

133. Borm, P.J.A.; Kreyling, W. Toxicological Hazards of Inhaled Nanoparticles - Potential Implications for Drug Delivery. *J Nanosci Nanotechnol* **2004**, *4*, 521–531, doi:10.1166/jnn.2004.081.

134. Pinto Carneiro, S.; Moine, L.; Tessier, B.; Nicolas, V.; dos Santos, O.; Fattal, E. Pyrazinoic Acid-Poly(Malic Acid) Biodegradable Nanoconjugate for Efficient Intracellular Delivery. *Precis Nanomed* **2019**, *2*, 303–317, doi:10.33218/prnano2(3).190523.1.

135. Hasan, A.S.; Socha, M.; Lamprecht, A.; Ghazouani, F. El; Sapin, A.; Hoffman, M.; Maincent, P.; Ubrich, N. Effect of the Microencapsulation of Nanoparticles on the Reduction of Burst Release. *Int J Pharm* **2007**, *344*, 53–61, doi:10.1016/j.ijpharm.2007.05.066.

136. Erez-Arellano, J.L.; Barrios, M.N.; Martin, T.; Sanchez, M.L.; Jimbnez, A.; Gonzalez-Buitrago, J.M. Hydrolytic Enzyme of the Alveolar Macrophage in Diffuse Pulmonary Interstitial Disease. *Respir Med* **1996**, *90*, 159–166, doi:10.1016/s0954-6111(96)90158-4.

137. Hoffmann, S.; Gorzelanny, C.; Moerschbacher, B.; Goycoolea, F.M. Physicochemical Characterization of FRET-Labelled Chitosan Nanocapsules and Model Degradation Studies. *Nanomaterials* **2018**, *8*, 846, doi:10.3390/nano8100846.

138. Trousil, J.; Syrová, Z.; Dal, N.J.K.; Rak, D.; Konefal, R.; Pavlova, E.; Matějková, J.; Cmarko, D.; Kubíčková, P.; Pavliš, O.; et al. Rifampicin Nanoformulation Enhances Treatment of Tuberculosis in Zebrafish. *Biomacromolecules* **2019**, *20*, 1798–1815, doi:10.1021/acs.biomac.9b00214.

139. Yu, Z.; Li, H.; Jia, Y.; Qiao, Y.; Wang, C.; Zhou, Q.; He, X.; Yu, S.; Yang, T.; Wu, H. Ratiometric Co-Delivery of Doxorubicin and Docetaxel by Covalently Conjugating with MPEG-Poly(β-Malic Acid) for Enhanced Synergistic Breast Tumor Therapy. *Polym Chem* **2020**, *11*, 7330–7339, doi:10.1039/d0py01130d.

140. Tsapis, N.; Bennett, D.; Jackson, B.; Weitz, D.A.; Edwards, D.A. Trojan Particles: Large Porous Carriers of Nanoparticles for Drug Delivery. *PNAS* **2002**, *99*, 12001–12005, doi:10.1073/pnas.182233999.

141. Huang, Y.; Tang, H.; Meng, X.; Zhao, Z.; Liu, Y.; Liu, D.; Chen, B.; Zou, Z. Development of Large Hollow Particles for Pulmonary Delivery of Cyclosporine A. *Pharmaceutics* **2023**, *15*, doi:10.3390/pharmaceutics15092204.

142. Ke, W.R.; Chang, R.Y.K.; Kwok, P.C.L.; Chen, D.; Chan, H.K. Spray Drying Lactose from Organic Solvent Suspensions for Aerosol Delivery to the Lungs. *Int J Pharm* **2020**, *591*, 119984, doi:10.1016/j.ijpharm.2020.119984.

143. Ke, W.R.; Kwok, P.C.L.; Khanal, D.; Chang, R.Y.K.; Chan, H.K. Co-Spray Dried Hydrophobic Drug Formulations with Crystalline Lactose for Inhalation Aerosol Delivery. *Int J Pharm* **2021**, *602*, 120608, doi:10.1016/j.ijpharm.2021.120608.

144. Wu, L.; Miao, X.; Shan, Z.; Huang, Y.; Li, L.; Pan, X.; Yao, Q.; Li, G.; Wu, C. Studies on the Spray Dried Lactose as Carrier for Dry Powder Inhalation. *Asian J Pharm Sci* **2014**, *9*, 336–341, doi:10.1016/j.ajps.2014.07.006.

145. Catanzaro, R.; Sciuto, M.; Marotta, F. Lactose Intolerance: An Update on Its Pathogenesis, Diagnosis, and Treatment. *Nutrition Research* **2021**, *89*, 23–34, doi:10.1016/j.nutres.2021.02.003.

146. Eadala, P.; Waud, J.P.; Matthews, S.B.; Green, J.T.; Campbell, A.K. Quantifying the "hidden" Lactose in Drugs Used for the Treatment of Gastrointestinal Conditions. *Aliment Pharmacol Ther* **2009**, *29*, 677–687, doi:10.1111/j.1365-2036.2008.03889.x.

147. Najafabadi, A.R.; Gilani, K.; Barghi, M.; Rafiee-Tehrani, M. The Effect of Vehicle on Physical Properties and Aerosolisation Behaviour of Disodium Cromoglycate Microparticles Spray Dried Alone or with L-Leucine. *Int J Pharm* **2004**, *285*, 97–108, doi:10.1016/j.ijpharm.2004.07.027.

148. Rabbani, N.R.; Seville, P.C. The Influence of Formulation Components on the Aerosolisation Properties of Spray-Dried Powders. *Journal of Controlled Release* **2005**, *110*, 130–140, doi:10.1016/j.jconrel.2005.09.004.

149. Staniforth JN Powders Comprising Anti-Adherant Materials for Use in Dry Powder Inhalers 2002.

150. Glinski, J.; Chavepeyer, G.; Platten, J.-K. Surface Properties of Aqueous Solutions of L-Leucine. *Biophys Chem* **2000**, *84*, 99–103, doi:10.1016/s0301-4622(99)00150-7.

151. Columbano, A.; Buckton, G.; Wikeley, P. Characterisation of Surface Modified Salbutamol Sulphate-Alkylpolyglycoside Microparticles Prepared by Spray Drying. *Int J Pharm* **2003**, *253*, 61–70, doi:10.1016/s0378-5173(02)00634-8.

152. Li, H.Y.; Neill, H.; Innocent, R.; Seville, P.; Williamson, I.; Birchall, J.C. Enhanced Dispersibility and Deposition of Spray-Dried Powders for Pulmonary Gene Therapy. *J Drug Target* **2003**, *11*, 425–432, doi:10.1080/10611860410001659786.

153. Li, H.Y.; Seville, P.C.; Williamson, I.J.; Birchall, J.C. The Use of Amino Acids to Enhance the Aerosolisation of Spray-Dried Powders for Pulmonary Gene Therapy. *Journal of Gene Medicine* **2005**, *7*, 343–353, doi:10.1002/jgm.654.

154. Li, Y.Z.; Sun, X.; Gong, T.; Liu, J.; Zuo, J.; Zhang, Z.R. Inhalable Microparticles as Carriers for Pulmonary Delivery of Thymopentin-Loaded Solid Lipid Nanoparticles. *Pharm Res* **2010**, *27*, 1977–1986, doi:10.1007/s11095-010-0201-z.

155. Ruge, C.A.; Bohr, A.; Beck-Broichsitter, M.; Nicolas, V.; Tsapis, N.; Fattal, E. Disintegration of Nano-Embedded Microparticles after Deposition on Mucus: A Mechanistic Study. *Colloids Surf B Biointerfaces* **2016**, *139*, 219–227, doi:10.1016/j.colsurfb.2015.12.017.

Acknowledgments

I want to thank Professor Ruggero Bettini, my supervisor, who guided me professionally and carefully in realizing this project.

I acknowledge Professor Elias Fattal, Professor Nicolas Tsapis, and Professor Laurence Moine for kindly welcoming and guiding me at Institut Galien Paris-Saclay - UMR CNRS 8612, and Dr. Thi Hong Van Nguyen, with whom I had the great honour of collaborating. In this regard, I am grateful to the ULLA consortium for the financial support that helped me realize this amazing, educational experience.

A significant thank you goes to Professor Andrea Sartori for precious NMR studies.

I wish to acknowledge Dr. Giovanna Trevisi from the IMEM-CNR for scanning electron microscopy analysis and Prof. Paolo Pio Mazzeo from the SCVSA department for powder X-ray diffraction analysis.

Finally, I want to remember the undergraduate students who contributed to part of this project, Rosita Nicolella Gentile and Saveria Germani.